# Mechanisms of the Reductive Immobilization of Hexavalent Chromium by Wheat Straw Biochar

by

Manuel Giancarlo Cossio Kohler

A thesis submitted in partial fulfillment of the requirements for the degree of

Master of Science

Department of Earth and Atmospheric Sciences
University of Alberta

ABSTRACT

Biochar has received significant attention as an innovative sorbent for treating heavy metal contamination due to its high surface reactivity and sorption capacity, ease of manufacture and low production cost. Most studies involving chromium removal from solution by biochar have focused on removal rates and extent, which largely ignores the mechanisms of sorption and electron transfer that occur during Cr immobilization. For this reason, a comprehensive Cr-biochar study that couples adsorption and reduction kinetics to spectroscopic data to elucidate the Cr binding environment and speciation on the biochar was conducted.

Wheat Straw biochar (WSBC), produced by the Alberta Biochar Initiative, was used to sorptively remove and subsequently reduce hexavalent chromium (Cr(VI)) from solution over the course of days at a range of acidic pH (between 2 – 3). Sorption and reduction kinetics were monitored and concentration-independent intrinsic rate constants for both phenomena were calculated. To understand the Cr binding environment on the surface of WSBC following metal reduction, synchrotron X-ray adsorption spectroscopy, synchrotron-based X-ray fluorescence mapping, Fourier transform infrared spectroscopy, Raman microscopy and scanning electron microscopy were performed. The results show that (1) the reduction and sorption of Cr(VI) with WSBC is possible, especially in acidic media, (2) that the distribution of Cr on the WSBC surface is heterogeneous, and (3) the Cr(III) binding to WSBC surfaces are dominated by O-containing functional groups, with hydroxyl groups comprising the majority of the Cr binding sites, followed by binding to carboxyl and carbonyl groups.

ACKNOWLEDGMENTS

I would like to thank Dr. Daniel Alessi, who has guided me throughout the course of my graduate studies. I would also like to thank my co-supervisor Dr. Kurt Konhauser, who has provided me with invaluable assistance. I would also like to show my gratitude to all my colleagues and fellow members of the Environmental Geochemistry Lab for providing me help through the lengths of my research.

I would like to thank the following researchers for their invaluable contribution into this project: Dr. Ning Chen for the XANES analysis and EXAFS interpretation of Cr standards and Cr-laden biochar samples, Dr. Janice Kenney for the fitting of the FTIR spectra of Cr-laden biochar samples, Dr. Andras Gorzsas for aiding with the Raman analysis and all the help involving the D and G bands of wheat straw derived biochar, Dr. Renfei Fend and Dr. Blanchard with VESPERS and Cr XRF maps generation in Cr-laden biochar samples.

This research was supported by a NSERC Discovery grant to DSA.

TABLE OF CONTENTS

LIST OF FIGURES

LIST OF TABLES

# INTRODUCTION

Chromium (Cr) naturally accumulates at the surface of the Earth through weathering of Cr-bearing rocks, wet precipitation and dry fallout from the atmosphere, and run-off from terrestrial systems (Kotasâ & Stasicka, 2000). Natural concentrations of Cr in surface waters are between 0.5 to 2 ppb Cr (WHO, 2011), while concentrations of Cr in various soil commonly ranges from 1.04 to 3016 ppm from airborne Cr-deposition to anthropogenic Cr-sludge influence (Kotasâ & Stasicka, 2000). Anthropogenic sources result from the direct release of Cr-loaded wastewaters or solid wastes from industries, which include: finishing, electroplating, leather tanning, pigments, chemical manufacturing, wood protection, nuclear power plants, and mining (Gottipati & Mishra, 2010; Kimbrough *et al.*, 1999; Kotasâ & Stasicka, 2000). In Canada, chromium production is primordially located near the Ring of Fire chromite ore deposits in Northern Ontario (e.g. Timmins, James Bays and Nakina). Surface finishing industry in particular produces spent plating bathwaters and contaminated rinsewaters that are highly acidic and contain elevated Cr concentrate, ranging from 20 to 500 ppm of Cr(VI), from the use of chromic acid in the electroplating and anodizing process (Cabatingan *et al.*, 2001). Cr-laden wastewaters, produced from various industries, often contain concentrations between 0.1 to 200 ppm, but as high as 3950 ppm has been reported (Dong *et al.*, 2011).

Cr contamination is of considerable concern because it is a known carcinogen to humans (Cohen *et al.*, 2008; Costa, 2008; Hayes, 1997). The Cr(VI) limit in drinking water standard has been set to 50 ppb (WHO, 2011), while the total Cr concentration has been set to 0.1 ppm by the United States Environmental Protection Agency (EPA). Therefore, contamination of water and soil to Cr levels above the regulatory limits can occur with relatively small industrial releases, and

Cr contaminated waters must therefore be carefully treated to lower concentrations before they can be discharged into the environment (Wang *et al*., 2010).

Cr has multiple oxidation states, ranging from -2 to +6, but only trivalent chromium, Cr(III), and hexavalent chromium, Cr(VI), are stable under most surface environmental conditions (Fendorf, 1995; Kotasâ & Stasicka, 2000; Tytłak *et al.*, 2015). Both Cr species, Cr(III) and Cr(VI), are often found in industrial wastewaters; however, they have remarkable differences in mobility, solubility and toxicological properties. Cr(VI) is highly soluble and is a known carcinogen, mutagen and teratogen (Choppala *et al.*, 2010; Kimbrough *et al.*, 1999; Murphy *et al.*, 2009). Long term contact and exposure to Cr(VI) may cause lung cancer, kidney and gastric damage, epidermal irritation ,and sensitization (Kimbrough *et al.*, 1999). Cr(VI) exists as an oxyanion, rather than as a free ion, and resembles biological nutrients, such as phosphates and sulphates, which are required for diverse biochemical processes in the human body (Costa, 2003). Cr(VI), having a coordination number (CN) of four, will bind to 4 oxygen molecules, producing an overall negative (2-) charge intrinsic to oxyanions. Chromates ($CrO_4^{2-}$ , $HCrO_4^-$ and $H_2CrO_4$) and dichromates ($Cr_2O_7^{2-}$) are the two distinct Cr(VI) oxyanion species. The resemblance of chromates and dichromates to such bionutrients results in the cell mistakenly transporting external Cr(VI) through the cell membrane (Costa, 2003). Due to the strong oxidizing nature of Cr(VI) (E(V) = +1.23), Cr(VI) will be reduced to Cr(III) by most, if not all, cells inside the body (Rai *et al.*, 1989). The reduction of Cr(VI) to Cr(III) produces free radicals (OH·, O, $O_2^-$, RS·, R·) (Fendorf, 1995; Kotasâ & Stasicka, 2000), which are known to trigger a number of human diseases by the adverse alteration of lipids, proteins and DNA. Not only will Cr(VI) reduction produce free radicals, but it also produce unstable Cr intermediate species, Cr(IV) and Cr(V) that are highly labile and transient and will produce more free radicals as they are reduced to Cr(III) (Costa, 2003).

In contrast to Cr(VI), Cr(III) is relatively immobile, with Cr(III) concentrations being controlled by chemical and physical process, such as hydrolysis, complexation, redox reactions and adsorption (Kotasâ & Stasicka, 2000). Cr(III) exists as free cations and is easily hydrolyzed in the absence of complexing agents, especially organic agents, such as amino, fulvic, humic, and other organic acids (Kotasâ & Stasicka, 2000). Cr(III) concentrations in aqueous solution are limited by the low solubility of $Cr(OH)_3(s)$ at circumneutral pH (Costa, 2003; Kimbrough *et al.*, 1999), and since Cr(III) lacks any resemblance to biological nutrients, it is unlikely to go through the cell membrane (Costa, 2003). Not only is Cr(III) highly insoluble and relatively immobile, but it is can also be considered an essential micronutrient required for sugar and fat metabolism (Anderson, 1997). Supplementation of Cr(III) has recorded to improve patients under stress, helped to prevent sugar-induced hypertension, and has been shown to improve insulin and several risks associated with cardiovascular disease and diabetes (Anderson, 1997). Nonetheless, most side effects from Cr contamination in humans arise due to Cr exposure at above 50 to 100 ppb over extended periods of time.

Conventional techniques used for Cr removal involve chemical precipitation, ion exchange, membrane separation, ultrafiltration, vitrification, electrokinetics, sedimentation, and adsorption; however, such treatments often suffer from high technical costs, low efficiency and selectivity, high-energy requirements, and they may generate toxic byproducts (Hawley *et al.*, 2004; Palmer & Wittbrodt, 1991; Sharma & Forster, 1994; Tytłak *et al.*, 2015;). As a result, there has been a recent research focus on the use of biomaterials, produced at low cost from naturally-occurring and abundant biomass, that may be capable of removing Cr from aqueous solution and/or soil systems (Fomina & Michael, 2014; Garg *et al.*, 2007; Inyang *et al.*, 2016; Murphy *et al.*, 2008; Nguyen *et al.*, 2013; Saha & Orvig, 2010). These materials are referred to as biosorbents, since

they employ biosorption as the main removal mechanism. Activated carbon (AC) is one of the most commonly-used carbonaceous sorbents for industrial wastewaters treatment (Pollard *et al.*, 1992; Ahmad *et al.*, 2014). Carbonaceous materials such as AC are often chemically or physically activated to increase the adsorption capacity of the biomaterial, as a result of the greater surface area and increased microporosity after activation (Sharma & Forster, 1994). The production of AC remains an expensive process (Owlad & Aroua, 2009), and consequently, there has been a growth in research focused on well-dispersed and low-cost biosorbents (e.g., Pollard *et al.*, 1992).

Biochar (BC) presents a promising alternative treatment technology to AC. BC is the carbonaceous material obtained from the thermal decomposition of biomass under a limited oxygen atmosphere (Lehmann, 2007). Charcoal and biochar are very similar pyrolysis products but have different applications. Charcoal is used for the generation of energy and fuel production, while BC is applied for carbon sequestration and environmental management. The applications of biochar include soil improvement, climate change mitigation, energy production and waste management (Ahmad *et al.*, 2014; Lehmann, 2007). Biochar is enriched in carbon, with up to 90% of the original organic carbon being retained (Beesley *et al.*, 2011). It is also a very stable material, making it resistant to chemical and microbial breakdown in the natural environment (Mohanty *et al.*, 2013).

BC contains both crystalized aromatic carbons and non-polyromantic carbon. Guo and Chen (2014) attribute the recalcitrance of BC to the degree of aromaticity of C, with greater recalcitrance proportional to higher pyrolysis temperatures. BC produced from feedstock with elevated Si concentration at 500$^{o}$C yielded intertwined C-Si structures and Si-encapsulated C, and have markedly decreased degradation rates of BC in soil systems because incorporated Si increases the intrinsic stability of C in BC (Guo & Chen, 2014; Xiao *et al.*, 2014). Additionally, BC has

great potential to reduce $CO_2$ emissions from soil by sequestering C for hundreds to thousands of years (Ahmad *et al.*, 2014; Beesley *et al.*, 2010; Lehmann, 2007; Mohanty *et al.*, 2013). BC is not only capable of reducing $CO_2$ emissions, but I can also decrease the production of methane. In fact, BC is also know to decrease nitrous oxide emissions by interfering with the nitrogen (N) cycle within soil systems (Roberts *et al.*, 2009; Verheijen *et al.*, 2010).

Slow pyrolysis of biomass generates bio-oils and syngas as BC-coproducts (Bian *et al.*, 2016). BC production releases more energy than it consumes, and combined with the co-productivity of bio-oils and syngas, makes the pyrolysis of biomass to produce BC a promising alternative for bioenergy generation. The International Biochar Initiative (IBI) has proposed that up to 80% of crop and forest waste will eventually be converted to BC, paving the way for BC to replace coal for energy generation by the year 2050.

The amendment of BC to agricultural soils can yield positive results in crop yields by improving soil fertility via increased soil pH, cation exchange capacity, water holding capacity, enhance fungal and bacterial communities growth, and reduced soil compaction (Jones *et al.*, 2016; Verheijen *et al.*, 2010; Zhang & Ok, 2014). The cation content of BC is often strongly correlated to its ash content. High pyrolysis temperatures increase the ash content in BC, particularly macronutrients such as Ca, Mg, K, and some micronutrients such as P, Na, Mn, Fe, Zn and Cu; the release of these nutrients can then have a positive effect on crop yield (Titiladunayo *et al.*, 2012). Most importantly, BC improves nutrient retention by reducing leaching and increasing the ion exchange capacity of soils, while at the same time providing an increase in the major cations and essential nutrients mentioned above (Lehmann & Rondon, 2006; Lehmann & Steiner, 2003)

BC has been recognized as a promising technology for environmental remediation because of its high surface area and chemical reactivity. It has been reported that BC can remove heavy

metals via electrostatic interaction, ionic exchange, and precipitation, while the removal of organic pollutants has been mostly attributed to adsorption and partitioning mechanisms (Alam *et al.*, 2016; Ahmad *et al.*, 2014; Beesley *et al.*, 2011; Tang *et al.*, 2013). Pyrolysis conditions (residence time, pyrolysis temperature, humidity, and heating rate) and biomass type affect the BC properties and consequently the surface chemistry of BC can be tuned for applications in the cleanup of either organic or inorganic contaminants (Mohan *et al.*, 2014). High pyrolysis temperature decreases the O and H contents, resulting in lower molecular H/C and O/C ratios due to increased dehydration and deoxygenation (Li *et al.*, 2013), while at the same time increasing BC surface area. Higher levels of dehydration and deoxygenation decrease polarity and increase conductivity of the BC by the realignment of graphene sheets and through the growth of aromatic C planes from the loss of labile aliphatic components (Li *et al.*, 2013). Thus, BC produced at elevated temperatures possess greater hydrophobicity (low polarity), surface area and pore volume, and a complete loss of volatile matter and easily degradable aliphatic C which makes them suitable for sorption of organic contaminants. For example, Ahmad *et al.* (2012) produced a soybean stover derived biochar (SSBC) and a peanut shell derived biochar (PSBC) capable of removing trichloroethylene (TCE) via sorption. The BC was produced at both 300ºC and 700ºC, with maximum sorption capacity of 32 mg $g^{-1}$ and 12 mg $g^{-1}$, respectively. SSBC and PSBC produced at 700ºC led to a BC that displayed comparable TCE adsorption capabilities to those exhibited by AC. The high sorption values for TCE were attributed to the increase in hydrophobicity and SA, and the decrease of polarity and O-containing surface functional groups resulting from high pyrolysis temperatures (Ahmad *et al*., 2012). On the other hand, removal of heavy metals from solution is generally more efficient when using low temperature BC as a sorbent. Titiladunayo *et al.* (2012) produced a BC derived from charred lignocellulosic biomass at pyrolysis temperatures of 400º and 500º C. The

resulting BC retained 13% and 8% O, respectively, in comparison to a BC produced from the same feedstock at 800$^{o}$, which contained < 0.1% O. Thus, BC pyrolyzed at lower temperature retained higher concentrations of O-containing functional groups. This is important for heavy metal removal since O-containing carboxyl, carbonyl, hydroxyl, and phenolic surface functional groups can bind soil contaminants, especially heavy metals (Uchimiya *et al.*, 2011a). Because low temperature BC retains a higher degree of polarity, related to higher content of O-containing functional groups, it adsorbs water as a result of hydrogen bonding, which in turn, leads to the formation of water clusters that can inhibit the sorption of organic contaminants (Ahmad *et al.*, 2012). However, this polarity is conversely beneficial to the sorption of charged metal species. For instance, Uchimiya *et al.*, (2011b) demonstrated that cottonseed hull biochar, produced at 350$^{o}$C, displayed greater removal capabilities for Pb(II), Cd(II), Cu(II) and Ni(II) than biochar produced at higher temperatures. Uchimiya *et al.* (2011b) attributed such greater removal capacity for heavy metals to the greater electrostatic interaction between cations and negatively charged surfaces intrinsic to low pyrolysis biochars, as a result of O-containing surface functional groups. In particular, metals will form complexes with easily accessible carboxyl (-COOH) and hydroxyl (-OH) functional groups (Ahmad *et al.*, 2014), which can deprotonate and have negative surface charge. Several additional recent studies using various BC have further confirmed that low temperature BC are especially capable of heavy metal removal from solution (Inyang *et al.*, 2012; Johansson *et al.*, 2016; Jones *et al.*, 2016; Melo *et al.*, 2013; Park *et al*., 2011; Rinklebe *et al.*, 2016; Tang *et al.*, 2013; Zhuang *et al.*, 2011).

In terms of the biomass sourced for BC, lignocellulose accounts for as much as 50% of all types of biomasses (Naik *et al.*, 2010), and is substantially available in Canada, with as much as 561 million dry tons produced per annum (Nanda *et al.*, 2013). Lignocellulose is a very important

starting material for the production of AC and BC (Pollard *et al.*, 1992), with higher BC yields correlated to higher lignin content (Titiladunayo *et al.*, 2012). Wheat straw (WS) is one of the most widespread and easily available agricultural residues (Atik & Ates, 2012), with approximately 25 million metric tons of wheat produced in Canada in 2011 (Agricultural Statistics, 2011). Naik *et al.* (2010) identified WS as a potential candidate for bioenergy production due to its high calorific value, volatility, cellulose and hemicellulose content. Production of wheat straw biochar, WSBC, could help direct the vast amounts of wheat straw residue produced in Canada toward alternative uses in bioenergy production, soil fertilization, C sequestration, and also in remediation technologies such as treating metals in industrial wastewater streams.

Cr has been removed from aqueous solution by BC produced from sugar beet tailings (Dong *et al.*, 2011), coconut coir (Shen *et al.*, 2012), dew melon peels (Ahmadi *et al.*, 2016), rice husks (Agrafioti *et al.*, 2014), and oak wood and bark (Mohan, *et al*., 2011). The mechanism of Cr removal by BC has been attributed to an adsorption-coupled reduction process (Park *et al*., 2005; 2006; 2008) in acidic systems. O-containing functional groups are important in the removal of Cr(VI), in particular hydroxyl, phenolic ,carboxyl and carbonyl surface functional groups (Shen *et al.*, 2012). Protonation of these functional groups under acidic conditions and the resulting increase in positive charge at the surface result in enhanced sorption of the Cr(VI) anion at low pH. Fourier transform infrared (FTIR) spectroscopy studies demonstrate that Cr(VI) aqueous species are readily adsorbed to BC surface functional groups, resulting in the subsequent oxidation of phenolic groups, producing higher quantities of carboxyl and carbonyl groups capable of adsorbing Cr(III) (Hsu *et al*., 2009; Shen *et al*., 2012).

Despite this initial characterization, the mechanisms of Cr(VI) adsorption and reduction to immobilized Cr(III) species at the BC surface is poorly understood, especially in untreated biochar

(e.g., not acid washed) and in those with high concentrations of Si. Untreated biochar is the material likely to be used in pilot scale and industrial scale applications, and WSBC (a major potential product in Canada) will have relatively high Si contents since wheat is known to show great accumulation of Si. Moreover, even as studies utilizing different biochar types for Cr(VI) removal increase, the micron-scale Cr speciation and distribution at the surface of biochar remains unstudied.

For this thesis research, I focused on the removal of Cr(VI), especially in acidic systems that mimic the releases from electroplating rinsewaters, with locally-produced wheat straw biochar (WSBC). WSBC was provided by the Alberta Biochar initiative (ABI) and was previously characterized and used for removal of organic acids (Alam *et al.*, 2016), but its potential for the treatment of heavy metals in water remained untested. The objectives of this study were to: (1) fully characterize WSBC with new alkaline fusion and sequential extractions method for better WSBC elemental characterization, with a special focus on Si; (2) elucidate the Cr removal capabilities of WSBC for sorption and reduction by using batch kinetics experiments as a function of pH, contact time, and initial Cr concentration, (3) study the Cr speciation before, during and after Cr kinetics experiments by multiple spectroscopic techniques, (4) determine the role of specific O-containing functional groups in Cr sorption/reduction reactions, and (5) determine the role of graphitic carbonaceous structures in WSBC in controlling the reductive immobilization and distribution of Cr(III) species on the surface and within the structure of WSBC.

## METHODS

### *2.1. Past WSBC analysis and complete elemental analysis via alkaline fusion and sequential extractions and ICP-MS configuration Biochar characterization*

*2.1.1. Previous work on WSBC*

Initial chemical and morphological analyses on WSBC were performed and described by Alam *et al*. (2016) including physical parameters, such as surface area, pore volume and C, H, N, and O elemental analyses, and molar ratios (summarized in section 3.1).

*2.1.2. Alkaline fusion & Sequential extraction*

Alkaline fusion was performed on WSBC to determine bulk elemental content, and in particular to measure Si, which cannot be quantified using common total digestion methods. Alkaline fusion was performed according to a modified method by GBC Scientific Equipment (2013) and as described in von Gunten *et al*. (2017). To do so, 10 g of WSBC was ashed in a furnace for 6 h at 500 °C. Following, 1.5 g of sodium hydroxide (NaOH, ACS certified, ACROS Organics) was melted in a nickel crucible over a Bunsen burner. Once the crucible cooled down, 0.1 g of WSBC ash, 0.5 g NaOH and 0.5 g of sodium peroxide ($Na_2O_2$, ACS certified, Fisher Scientific) were added to the crucible, it was then covered with a lid, and heated for another 5 min. After cooling, the outside of the crucible was washed with 6 M hydrochloric acid (HCl, ACS certified, Fisher Scientific) and placed into a 250 mL polypropylene beaker together with the lid. Ultrapure water (18.5 Ω at 25°C) and approximately 25 mL 6 M HCl were added until the fused mass dissolved. After removing the crucible and lid from each beaker, the volume was adjusted to 50 mL with ultrapure water. Each BC sample was analyzed in duplicate, along with a blank (no ash added). Obtained solutions were diluted (1:20 ratio) prior to analysis using an inductively coupled plasma – triple quadrupole mass spectrometer (ICP-MS/MS; Agilent Technologies 8800; see below for details). After data collection, metal concentrations were corrected using blank-value subtractions.

Sequential extractions were performed in triplicates according to a modified Community Bureau of Reference (CBR) method by Yuan *et al.* (2011) and von Gunten *et al.* (2017). Briefly, 0.5 g of WSBC was put into 50 mL polypropylene centrifuge tubes and soaked in 20 mL of 0.1 M acetic acid (glacial, ACS certified, Fisher Scientific) for 16 h to obtain the first fraction (exchangeable/acid soluble fraction). The tubes were then centrifuged (Sorvall LYNX 4000, Fisher Scientific) at 17000 rcf for 15 min and 10 mL of the supernatant was removed and filtered through a 0.2 µm nylon membrane. The remaining liquid and the solid samples were flushed with ultrapure water using a vacuum filtration unit and 0.2 µm nylon membranes to retain the solids. The solids were flushed back into the tubes with ultrapure water and dried at 60°C in an oven (HERATHERM, Thermo Scientific). The remaining sample was further extracted in a second step with 20 mL of 0.1 M hydroxylamine chloride (ACS certified, Fisher Scientific), which was previously adjusted to pH 2 with nitric acid ($HNO_3$, ACS certified, Fisher Scientific), for 16 h to obtain the second fraction (reducible). The extraction liquid was recovered by centrifugation and the solids were flushed as described above. The oxidizable fraction was obtained by adding 5 mL of 30% $H_2O_2$ to the residues from step two, and allowing this mixture to react for 1 h at room temperature. Another 5 mL of 30% $H_2O_2$ was then added and the tubes were heated for 1 h in a heating block at 85 °C. 25 mL of 1 M ammonium acetate (HPLC grade, Fisher Scientific, previously adjusted to pH 2 with $HNO_3$) was added and the mixture was shaken for at least 30 min. The samples were centrifuged for supernatant recovery and flushed again for the last extraction step. For the final step (residual fraction), the remaining solid was transferred into ceramic trays and burned in a furnace at 500 °C for 6 h. The ash was transferred into 50 mL Teflon® FEP tubes for total digestion. The digestion was performed with 5 mL of 70% $HNO_3$ and 5 mL of 47-51% HF at 130°C until all solution was evaporated, followed by a final addition of 3

mL 37% HCl and 1 mL 70% $HNO_3$ at 130°C until only a small amount of liquid remained. The remains were diluted to 50 mL with 2% HNO3 and 0.5% HCl. The residual fraction for Si was calculated by subtracting the concentrations obtained in the previous steps from the total concentrations obtained by alkaline fusion.

*2.1.3. ICP-MS/MS analyses*

Elemental concentrations were analyzed with an 8800 ICP-MS Triple Quadrupole system (Agilent Technologies). Single-element standards (Spex CertiPrep, CPI International, Ricca Chemical Company) were used for external calibration and indium for internal calibration. Argon was used as the carrier gas. Four measurements were performed for each sample and required standard, with 300 scans performed per measurement. Each element was analyzed in normal MS/MS mode and additionally with the introduction of He gas (3 mL $min^{-1}$) to remove potential polyatomic interferences (May & Wiedmeyer, 1998). For Ca and Si, hydrogen gas was introduced as the collision gas (3 mL $min^{-1}$) based on the method in Agilent Technologies (2015). To measure Cr, As, and P, oxygen (10% $O_2$) was introduced into the reaction chamber (an octopole) and a mass shift (*m/z*) of 16 was considered in the second mass analyzer to select for the $^{52}Cr^{16}O^+$ (*m/z* 68), $^{75}As^{16}O^+$ (*m/z* 91), and $^{31}P^{16}O^+$ (*m/z* 47) polyatomic species (Agilent Technologies, 2015).

*2.2. Batch Kinetics experiments & Chromium analysis*

WSBC was initially dried overnight at 80°C in a dying oven and then crushed using a ceramic mortar and pestle. The crushed WSBC was passed through a 200-mesh sieve, and the smaller fraction was stored in an air tight container. No washing or any pretreatment was applied to the WSBC, in order to retain its original physical characteristics, which are relevant to pilot or

commercial scale applications of the material. Batch kinetics experiments were performed to determine the kinetics of both Cr(VI) adsorption and reduction. To prepare batch experiments, 100 ml glass serum bottles (Wheaton Scientific) were acid-washed and rinsed repeatedly with ultrapure water prior to use. A biochar loading of 1g $L^{-1}$ of WSBC, which allowed for meaningful slower kinetic sampling, was introduced into the serum bottle and mixed with 95 mL ultrapure water. The water-WSBC mixture was adjusted to the desired pH by adding small aliquots of 1 or 12 M NaOH and/or 1 or 12 M HCl, and pH measurements were taken using a Mettler Toledo FEP 20 pH meter. Serum bottles were then sealed with butyl stoppers and metal caps, and were bubbled with nitrogen gas for at least 1.5 h to remove oxygen and carbon dioxide from the solution and bottle head space. The resulting water-WSBC systems were left to equilibrate overnight on a shaker (New Brunswick Scientific Excella E5 Plataform shaker) at 200 rpm. Cr stock solutions of 1.7, 7 and 13 mM were prepared using potassium dichromate salt ($K_2Cr_2O_7$, ACS certified, Fischer Scientific), and underwent subsequent bubbling to render them anoxic. Using a sterile syringe, 5 mL of a given stock solution was injected into the sealed, equilibrated and anoxic water-WSBC serum bottles. Exponentially increasing and constant 12-hour sampling began once Cr(VI) was injected into the serum bottle system (t = 0) for Cr adsorption and reduction kinetics. For reduction analyses, 500 μL of Cr-biochar suspension was removed from the system using a 1 mL syringe (BD) and a 1.2 mm x 40 mm needle. The sample extraction volume never exceeded 3% of the total volume of an experiment. The removed Cr-WSBC slurry was spiked with 500 μL 1 M NaOH (1:1 ratio) in order to raise the pH and desorb all of the surface-bound Cr(VI) (American Public Health Association, American Water Works Association, & Water Environment Federation, 1999). The difference between the input concentration of Cr(VI) in an experiment, and that measured after Cr(VI) desorption using 1 M NaOH, was considered to be the reductively immobilized Cr(III)

fraction on the biochar itself. To quantify adsorption, no NaOH treatment was conducted. Both reduction and adsorption samples were filtered through a 0.2 μm nylon membrane (Econofilter), prior to analysis using photospectrometry (see below). Filtered solids from the 12-hour sampling series were stored in a laboratory fridge (Isotemp, Fisher Scientific) at 4$^{o}$C for further materials characterization studies.

A modified colorimetric method (method 7196A from the United States Environmental Protection Agency (EPA, 1992)) was used to measure Cr(VI) concentrations using a UV-Vis Spectrophotometer (Thermo Scientific Evolution 60S) and the 1,5-diphenylcarbazide (DPC, ACS certified, Acros) method. All experiments and colorimetric measurements were performed in triplicate. Total aqueous Cr, which includes both Cr(VI) and Cr(III), was only measured in the adsorption kinetics samples by ICP-MS/MS. Cr(III) was calculated by subtracting Cr(VI) measured by the DPC method from the total Cr concentration determined by ICP-MS/MS, according to:

$$Cr_{tot} = Cr_{(VI)} + Cr_{(III)}$$

*2.3. Fourier Transform Infrared Spectroscopy*

Solid WSBC samples collected from the kinetics experiments were dried under a fume hood overnight prior to FTIR analysis. Approximately 1 mg of sample was diluted with KBr (1:150 ratio) and pelletized by hand. FTIR analyses were performed using a Nicolet 8700 FTIR coupled with a DTGS KBr detector and XT-KBr beamsplitter. The range for the analysis was between 4000 cm$^{-1}$ to 450 cm$^{-1}$, with a resolution of 4.000 cm$^{-1}$ and 32 scans.

All spectra were baseline corrected using asymmetric least square fitting (Eilers, 2004) with parameters $\lambda$ = 70,000 and p= 0.001, smoothed using Savitzky – Golay (Savitzky & Golay,

1964) and area-normalised to the total area. Data were compiled into a Matlab file using OPUS v.7 by Bruker Optics and all manipulations were conducted using a Matlab-based graphical interface written by Felten *et al.* (2015).

*2.4 Cr K-edge XANES & EXAFS*

Cr K-edge X-ray absorption near edge structure (XANES) measurements were conducted at the Hard X-ray Microanalysis beamline (HXMA 06ID-1) of the Canadian Light Source (CLS) at the University of Saskatchewan, Canada to determine the speciation of Cr associated with WSBC. The CLS is a third-generation synchrotron facility operating at injection current of 250 mA and electron energy of 2.6 GeV. Beamline optics were comprised of a double Si (220) crystal monochromator, a toroidal focusing mirror, and a vertical collimating mirror, coupled along with a 32 Elemental solid state Ge detector were responsible for data collection. The monochromator was detuned to 40% of the maximum intensity to reduce the influence of higher-order harmonics. The pre-edge peak was assigned to 5989 eV by the photon energy calibration from a chromium metal foil, and $E_0$ values were determined from the adsorption edge step midpoint. XANES spectra measurements were taken between ~5790 eV to ~6500 eV for samples at pH 2.5 and 3.7, and between ~5790 eV to ~6800 eV for samples at pH 2, with step sizes of 0.25 eV. Reference spectra were collected in transmission mode, while samples spectra were collected in fluorescence mode. Each sample and standard underwent at least three scans.

The reference material standards included $K_2Cr_2O_7$, Cr(III) acetate, $Cr(OH)_3$, and Cr(III) acetylacetonate. Cr(III) acetate and Cr(III) acetylacetonate were purchased from Strem Chemical and Acros Organics respectively, with both chemicals having ACS certification. $Cr(OH)_3$ was synthesized by adding 10 M NaOH dropwise to a 0.5 M $CrCl_3$ solution until a circumneutral pH

was obtained, allowing the formation of a green $Cr(OH)_3$ precipitate. The resulting $Cr(OH)_3$ slurry was filtered using a Büchner funnel apparatus and left to dry under a fume hood. Reference standard pellets were prepared by mixing each reference compound with KBr (1:20 ratio) to minimize self-adsorption effects during X-ray absorption spectroscopy (XAS) analyses. KBr-standard mixtures were pressed into pellets using a hydraulic press and then wrapped in Kapton tape to hold the pellets together. Cr-laden WSBC samples were loaded onto Teflon® holders wrapped with Kapton tape. The samples and reference pellets were then mounted onto a stage for XANES analysis.

XANES raw data was processed using Athena software by Ravel & Newville (2005). XANES spectra for all sample were merged and normalized. Linear combination fitting (LCF) of samples with reference materials were produced for Cr-laden WSBC at pH 2, 2.5 and 3.7, with a 10% error accepted as indicated by Kelly *et al.* (2008. The R-factor calculated in Athena was utilized to evaluate the goodness of the LCF fits. WinXAS version 2.3 (Ressler, 1998) was used to fit extended X-ray absorption fine structure (EXAFS) data after preprocessing raw data using the Athena software package. FEFF 7 code was used to calculate the theoretical phase shift and backscattering amplitude function (Ankudinov & Rehr, 2000) from the crystal structure data of α-CrOOH (Christensen, 1976). Fits of Fourier transform (FT) $k^3$-weighted EXAFS data to FeFF modelling were produced using an R-space between 0.8 and 4.2 Å. The k range considered for modelling ranged between 3 to 10 $Å^{-1}$. For R-space fitting, the shift in the threshold energy ($E_0$) had the flexibility to vary for optimal fits optimization (Rihs *et al.*, 2014). Finally, the amplitude factor ($S_0^2$) was fixed to 1 for all fits.

*2.5 Morphology analysis*

The surface morphology of WSBC was characterized using a Zeiss Sigma Field Emission scanning electron microscope (SEM) operated under variable pressure with a resolution of approximately 10 nm, at the SEM Laboratory at the University of Alberta. Backscattered images were obtained using magnification ranges between 500x to 100x for WSBC. Energy dispersive X-ray spectroscopy (EDS) analyses, to investigate elemental concentrations, were obtained at specific locations using a Broker EDS system with dual silicon drift detectors, and having a resolution of 123 eV and beam spot size of 60 $mm^2$ for each detector.

*2.6 Bulk X-Ray Diffraction*

Bulk X-Ray Diffraction (XRD) was conducted using a Rigaku Geigeflex Powder Diffractometer (Rigaku Ultima IV) equipped with a cobalt tube, graphite monochromator and scintillation detector. One to two grams of powdered WSBC were mounted on zero-background plates for analysis. Diffraction pattern matching and searching were conducted using JADE 9.1 software and the ICDD and ICSD diffraction pattern databases.

*2.7 Thin section analysis*

*2.7.1 Thin section making process*

The BC material, including BC and Cr-laden BC, was mixed into a 1-inch round cylinder with epoxy (EPOTEK 301) and left to solidify overnight. The BC plug was then removed and lapped with glass using silicon carbide (SiC) as the abrasive. This process involved an initial lapping step utilizing 9 μm SiC abrasive, followed by a second 3 μm SiC abrasive lapping. Once the plug was flat enough to be mounted, it was glued to a thin glass (EPOTHIN, Buehler), cured overnight and

then cut utilizing a diamond tip blade. The cured and cut plug was then lapped to a thickness of 40 μm, and was achieved by using a 9 μm and 5 μm SiC abrasive utilizing a Logitech LP30 and Logitech PM5, respectively. Finally, the thin section underwent a polishing step that required a 3 μm diamond paste, producing a polished thin section with 30 μm thickness.

*2.7.2 Cr hotspot locations & XRF mapping*

To conduct X-ray fluorescence (XRF) mapping, biochar thin sections were carbon coated to approximately 25 nm. The carbon coated thin sections were then analyzed using an XRF (JOEL 8900R) featuring five wavelength spectrometers (WDS), and an energy dispersive spectrometer (Bruker EDS). A chromite standard was used to tune the machine in backscattered mode, to facilitate finding locations with high Cr concentrations or containing Cr precipitates. Backscatter mode was used to show differences in mean atomic number, making Cr brighter in comparison to C. Cr spots, ranging from 5 to 30 microns in size, were found and located in the thin section scans. EDS analysis was also performed at the hotspots to verify a relatively high concentration of Cr at those locations.

Synchrotron-based X-ray fluorescence (XRF) mapping was performed at the Very Sensitive Elemental and Structural Probe Employing Radiation beamline (VESPERS 07B2-1) at the CLS facility. To do so, biochar thin sections were positioned at a 45$^{o}$ angle relative to the synchrotron radiation source and a the single-element dispersive silicon drift XRF detector (Hitachi Vortex-90EX). All measurements were performed using the "Pink Beam" mode, which includes all X-ray energies from 4–30 keV (with a significant drop in flux occurring near 20 keV). The X-ray beam was focused down to approximately 3 μm$^2$ using the Kirkpatrick-Baez (KB) mirror system. High resolution XRF maps were obtained by moving the sample stage in three-

micron steps, dwelling for one second at each location. VESPERS data reduction and map processing were done using Excel 2010 and Surfer v.10 software.

*2.7.3 Raman spectroscopy*

Raman spectroscopy analyses were obtained at the Vibrational Spectroscopy Core Facility at Umeå University, using a Renishaw inVia Raman spectrometer with confocal microscope with tunable Ar-ion laser. The 457-nm blue laser was tuned at 50% for 1 sec to prevent and minimize sample damage, and the total power was calibrated to 15-30 MW. A 2400 line per millimeter gratings was also utilized. The samples for these analyses were Cr-laden BC thin sections. Raman scans were taken at 2 by 2 by 2 μm resolution.

Pre-processing of the original spectra included limiting the range between 300 $cm^{-1}$ and 1850 $cm^{-1}$, asymmetrical least squares baseline correction with parameters $\lambda$ = 1,000,000 and p = 0.001, normalization of the total area, and the Savitzky-Golay first order polynomial filter (Savitzky & Golay, 1964) with a frame rate of 13 for data smoothing. After pre-processing, data was analyzed utilizing the MatLab-GUI Multivariate Curve Resolution-Alternating Least Squares (MCR-ALS) GUI v.4 software.

## RESULTS & DISCUSSION

*3.1 Chemical and Physical characterization of WSBC*

Basic physicochemical and structural characteristics of unwashed WSBC are summarized in Tables 1 and 2 (modified from Alam *et al.*, 2016). Table 1 contains the pH, EC and proximal analysis results, while Table 2 contains basic chemical and structural analysis results of WSBC.

The ash content in WSBC was 17% (Table 1), which was higher than for wheat straw derived biochar produced by Kloss *et al.* (2012) who observed a 12.7% ash fraction from pyrolysis of wheat straw at 525$^{o}$C, or for wheat straw derived biochar produced by Bian *et al.* (2016) who observed a 14.6% ash fraction from pyrolysis at 400$^{o}$C. Fixed C was 47.3% (Table 1), lower than the 68.14% obtained by the wheat straw biochar produced by Bian *et al.* (2016). Factors including an elevated temperature, proportion of alkaline and alkali metals concentration, and the contribution of abundant Si would increase the proportion of ash in WSBC. Wheat straw pyrolyzed at 500$^{o}$C is more likely to produce greater ash content and release more volatiles than WSBC produced at lower temperatures. Even when the same mass of source WS is pyrolyzed, the elemental characteristics of biomass from different locations will vary, especially since the genesis of such biomasses are greatly affected by the natural and anthropogenic processes involved before, during and after genesis, as well as the difference on the local environments in which the wheat grew (Nanda *et al.*, 2013). The higher yield of ash in our biochar is likely related to the pyrolysis temperature, with generally higher concentrations of ash produced as a function of increasing pyrolysis temperature (Titiladunayo *et al.*, 2012). In fact, the ash produced during the pyrolysis process is related to the concentration of inorganic constituents of the original feedstock (Singh *et al.*, 2010; Titiladunayo *et al.*, 2012). Washing of the biochar removes some of its mineral ash content (Cao *et al.*, 2016; Mukherjee *et al.*, 2011), and thus unwashed biochar contains higher levels of ash. However, washing was unlikely the reason for the lower fixed C matter content in WSBC as compared to the wheat straw derived biochar produced by Bian *et al.* (2016) and Kloss *et al.* (2012), which were also not washed. Since the high-Si WS in our study was pyrolyzed at ~550$^{o}$C, which was above the pyrolysis temperature utilized by Bian *et al*. (2016) and Kloss *et al.* (2012), it is likely that more of the C in our biochar turned into ash and/or was released as carbon-

containing volatiles, yielding less fixed C. Therefore, the combination of both the elevated Si content in WS and the higher pyrolysis temperature yields WSBC with greater ash content.

| Sample | pH | EC (mS $cm^{-1}$) | Moisture content (%) | Mobile matter (%) | Ash content (%) | Fixed matter (%) |
|---|---|---|---|---|---|---|
| WSBC | 6.77 | 1.2 | 2.7 | 33.02 | 17 | 47.3 |

***Table 1.*** *pH, EC and proximal analysis of WSBC*

| Sample | C | H | N | N Wt (%) | S | O | H/C | O/C | (O+N)/C | Surface area ($m^2/g$) | Pore volume (cc/g) | Pore size distribution (Å) |
|---|---|---|---|---|---|---|---|---|---|---|---|---|
| WSBC | 69.68±0.52 | 2.58±0.03 | 2.58±0.03 | 0.81±0.01 | 0.07±0.01 | 8.65±0.99 | 0.4 | 0.1 | 0.1 | 26.64 | 18-22 | 5.00E-03 |

***Table 2.*** *Basic chemical and structural analysis of WSBC*

Higher pH in biochar is closely related to greater quantities of salts of alkali and alkaline elements such as Na, K, Ca, Mg; some biochar displays highly alkaline pH values because of the presence of carbonate and bicarbonates within their structure (Singh *et al.*, 2010; Tryon, 1948). WSBC displayed a circumneutral pH of 6.77 and had a lower pH value than other wheat straw derived biochar produced at 525$^{o}$C and 550$^{o}$C, with pH values of 9.2 and 9.0, respectively (Dang *et al.*, 2015; Kloss *et al.*, 2012). The circumneutral pH of WSBC could be correlated to its electrical conductivity (EC): the ability of a given material to transport charge. The measured EC of WSBC is affected by the content of salts as dissolved salts, with either positively and negatively charged ions being able to increase the intrinsic conductivity of the solution into which the biochar is placed. Manure feedstock biochar has high EC values owing to the high intrinsic concentrations of water-soluble salts (Singh *et al.*, 2010). A comparison of EC values between WSBC and the wheat straw derived biochar produced by Kloss *et al.* (2012) showed a deficit of 73% of EC in WSBC. Considering only alkali and alkaline cation, such as $K^{+}$, $Ca^{2+}$, $Na^{+}$, and $Mg^{2+}$, the sum of such cations in the exchangeable form was 9978 ppm as obtained from the sequential extractions (Tables 3 and 4). Although the concentrations of extractable $Ca^{2+}$, $Na^{+}$, and $Mg^{2+}$ were lower in the wheat straw biochar produced by Kloss *et al.* (2012), the overall sum of major cations including $K^{+}$ was 18443 ppm. Thus overall, the total sum of extractable $K^{+}$, $Ca^{2+}$, $Na^{+}$, and $Mg^{2+}$ for WSBC was only 50% of the total for the wheat straw biochar of Kloss *et al.* (2012), which explains the difference in the measured EC of WSBC. The pH of 6.77 of WSBC then likely results from the lesser extractable alkali and alkaline metals in WSBC.

| | Exchangeable/acid soluble µg/g | Reducible µg/g | Oxidizible µg/g | Residual µg/g | Total (sum) µg/g |
|---|---|---|---|---|---|
| Na | 122.09 ± 2.78 | 47.44 ± 4.69 | 167.02 ± 18.68 | 349.93 ± 64.14 | 686.48 ± 90.30 |
| Mg | 448.50 ± 25.01 | 404.31 ± 46.02 | 3043.37 ± 168.09 | 851.56 ± 208.19 | 4747.74 ± 447.31 |
| Al | 45.65 ± 0.38 | 359.75 ± 27.17 | 696.91 ± 38.43 | 2042.26 ± 366.75 | 3144.57 ± 432.72 |
| Si | 207.33 ± 10.76 | 191.63 ± 74.74 | 335.59 ± 33.84 | 46493.13 ± 14.97 | 47227.68 ± 103.46 |
| K | 6244.65 ± 502.46 | 1280.14 ± 70.59 | 1504.80 ± 98.56 | 1044.39 ± 234.42 | 10073.99 ± 906.03 |
| Ca | 3162.06 ± 201.06 | 364.48 ± 31.72 | 2973.06 ± 57.37 | 612.11 ± 142.61 | 7111.71 ± 432.76 |
| V | <0.04 | 0.48 ± 0.08 | 1.80 ± 0.15 | 3.81 ± 0.85 | 6.13 ± 1.08 |
| Cr | 0.08 ± 0.02 | 0.24 ± 0.04 | 2.93 ± 0.11 | 2.37 ± 0.11 | 5.61 ± 0.28 |
| Mn | 21.33 ± 1.21 | 21.29 ± 0.86 | 105.34 ± 4.49 | 30.23 ± 6.14 | 178.19 ± 12.70 |
| Fe | 7.41 ± 0.68 | 317.28 ± 42.17 | 829.61 ± 70.54 | 1146.41 ± 323.41 | 2300.72 ± 436.80 |
| Co | 0.09 ± 0.02 | 0.28 ± 0.02 | 0.97 ± 0.51 | 0.29 ± 0.07 | 1.64 ± 0.61 |
| Ni | 0.25 ± 0.08 | 0.41 ± 0.03 | 1.96 ± 0.16 | 2.27 ± 1.67 | 4.89 ± 1.94 |
| Cu | 5.94 ± 0.39 | 11.61 ± 0.74 | 9.08 ± 0.57 | 18.96 ± 8.72 | 45.59 ± 10.43 |
| Zn | 896.50 ± 73.57 | 84.37 ± 6.15 | 75.52 ± 5.71 | 24.97 ± 4.17 | 1081.36 ± 89.59 |
| As | 0.07 ± 0.01 | 0.07 ± 0.01 | 1.15 ± 0.02 | 0.21 ± 0.01 | 1.50 ± 0.05 |
| Sr | 35.37 ± 1.83 | 6.60 ± 0.28 | 54.49 ± 2.71 | 19.62 ± 4.45 | 116.08 ± 9.26 |
| Ba | 22.29 ± 0.64 | 35.32 ± 1.05 | 100.39 ± 4.97 | 54.36 ± 9.60 | 212.36 ± 16.25 |
| Pb | 0.18 ± 0.03 | 1.26 ± 0.13 | 0.52 ± 0.04 | 6.00 ± 2.83 | 7.95 ± 3.03 |
| U | <0.04 | <0.04 | <0.07 | <0.14 | <0.28 |

***Table 3.*** *Sequential extraction analysis results for WSBC*

Numerous elements were found in WSBC by sequential extractions and alkaline fusion, consisting of essential nutrients, non-essential elements and toxic metals. The most abundant elements found in WSBC are Si, Ca, K, Mg and Fe (Fig. 1). The combination of the concentration of alkali, alkaline metals, and especially Si, with a pyrolysis temperature of 500 - 550$^{o}$C resulted in elevated ash contents (Table 4). Sequential extractions indicate that some of the most abundant elements, such as K and Ca, are dominantly in the more labile extraction fractions. Thus, WSBC has the ability to both provide essential nutrients and to exert some control on soil pH.

| Element | Concentration (mg/g) |
|---|---|
| **Al** | 3.94 ± 0.17 |
| **Si** | 47.23 ± 0.10 |
| **Ca** | 6.00 ± 0.46 |
| **Fe** | 4.07 ± 0.05 |
| **Mg** | 3.96 ± 0.32 |
| **K** | 12.37 ± 1.01 |
| **P** | 0.78 ± 0.04 |

***Table 4.*** *Alkaline fusion analysis results for WSBC*

Micronutrient elements, such as Zn and Cu, and potentially hazardous elements, such as Pb, also make up the inorganic chemical composition of WSBC. The Pb levels in WSBC are approximately 8 ppm, within the normal background level of less than 10 ppm in soils (Mulligan *et al.*, 2001). The total Cu concentration, approximately 46 ppm, was within what are considered the average levels of Cu in rural soils between 2 to 100 ppm (Mulligan *et al.*, 2001); most of the total Cu was unlikely to be released as it is strongly bound to organic matter and clay minerals (Fig. 1). The total concentration of Zn in WSBC is 1081 ppm.. Approximately 83% of total Zn belongs to the exchangeable/acid soluble fraction; thus, as much as 897 ppm Zn could be easily leached from WSBC (Fig. 1, Table 3). In contrast to Zn, most Pb (75%) and Cu (42%) was associated with the more recalcitrant residual fractions. Accordingly, the Cu and Pb from WSBC would be less likely to be leached than Zn.

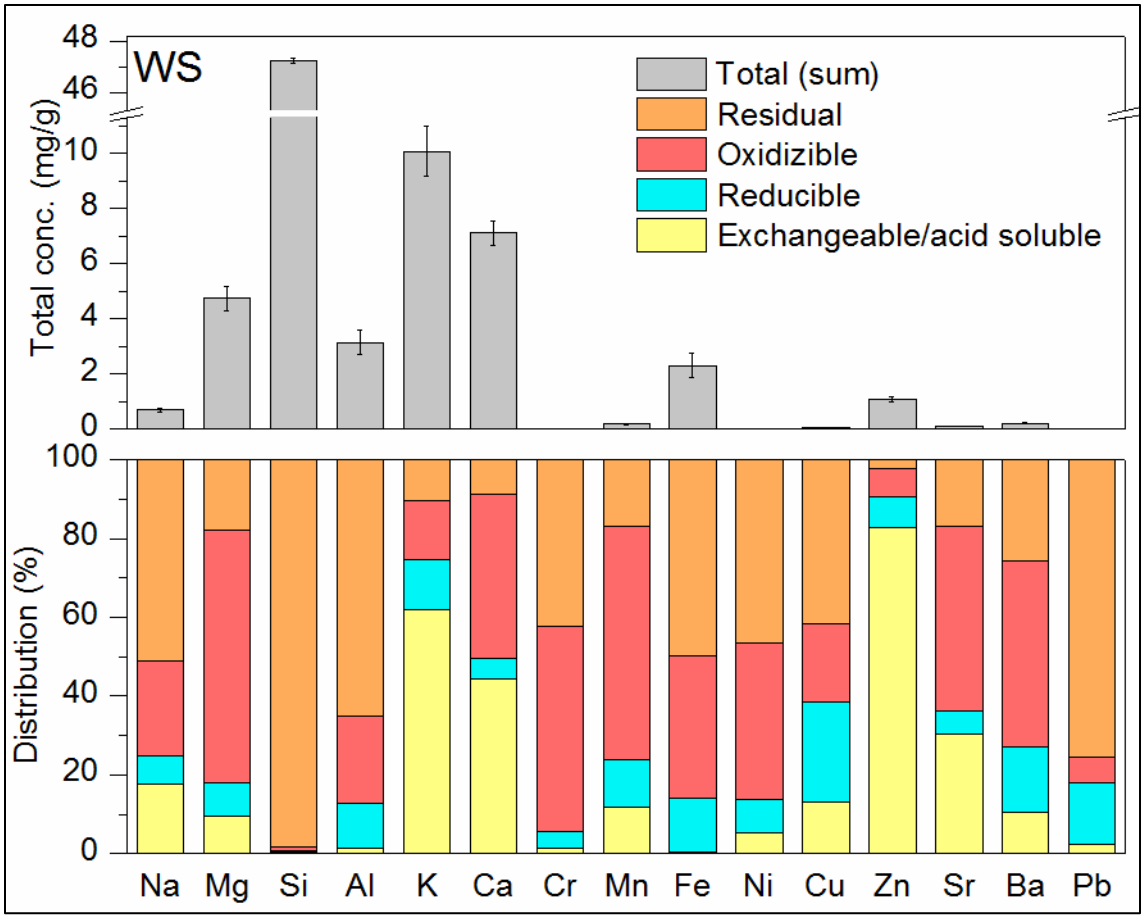


***Figure 1.*** *Sequential extraction distribution of elements from WSBC with total, residual, oxidizable, reducible and exchangeable/acid soluble fractions*

The surface morphology of unwashed WSBC was evaluated by SEM, which shows elongated WSBC grains of varied size, with most grains having an average length of approximately 1 mm (Fig. 2). Images of the three different orientations indicate that the physical morphology of WSBC is strongly controlled by the structure of the parent wheat straw biomass. For example, there is evidence in WSBC particles of channels along the growth (longitudinal) direction of the wheat straw (Mohanty *et al.*, 2013; Figs. 2 A, B, and C). There is also considerable variation among the surface morphologies of individual WSBC particles. For example, some particles have a relatively smooth surface and retain physical properties of the original wheat straw (*e.g.* Fig. 2C), while other biochar particles are rougher and fractured (*e.g.* Figs. 2A and 2B). There were two

distinct features in the image in Fig. 2C: (1) stomata, which are conduits innate to plants that aid and control gas exchange, remained relatively unchanged after pyrolysis of WS, and (2) numerous silicon nodules with heterogeneous distribution. These nodules likely explain why Si is the second most abundant element in the suite of elements found in WSBC, after C.

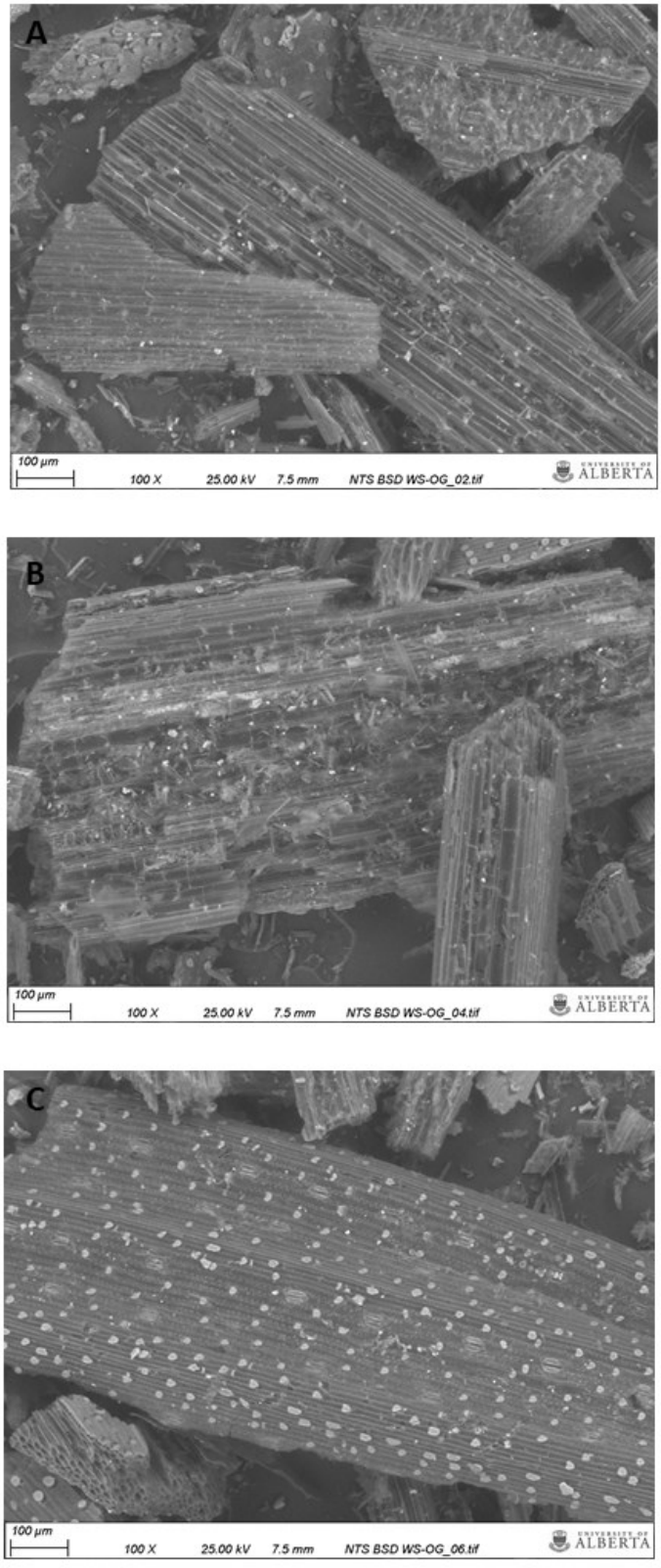


***Figure 2.*** *Scanning electron microscopy (SEM) images of unwashed WSBC at 100x at different orientations (A, B, and C)*

X-ray diffraction was performed on WSBC to quantify its crystalline phases (Fig. 3). The diffraction peaks identified in the biochar were matched to quartz, calcite and silicon carbide (Fig. 3A), while halite, albite and chalcopyrite and quartz were also found (Fig. 3B). Calcite and quartz are commonly found in biochar as a result of the reaction between $CO_2$ and alkaline metals and oxyhydroxides during the pyrolysis process (Kim *et al.*, 2011; Kloss *et al.*, 2012; Mohanty *et al.*, 2013). In addition, albite, a plagioclase feldspar, and halite were also found in the XRD spectra of WSBC. Considerable concentrations of silica are expected to be found in straws and grasses from Si adsorption during genesis, and this is reflected in the elemental composition of WSBC (Fig. 1, Table 3).

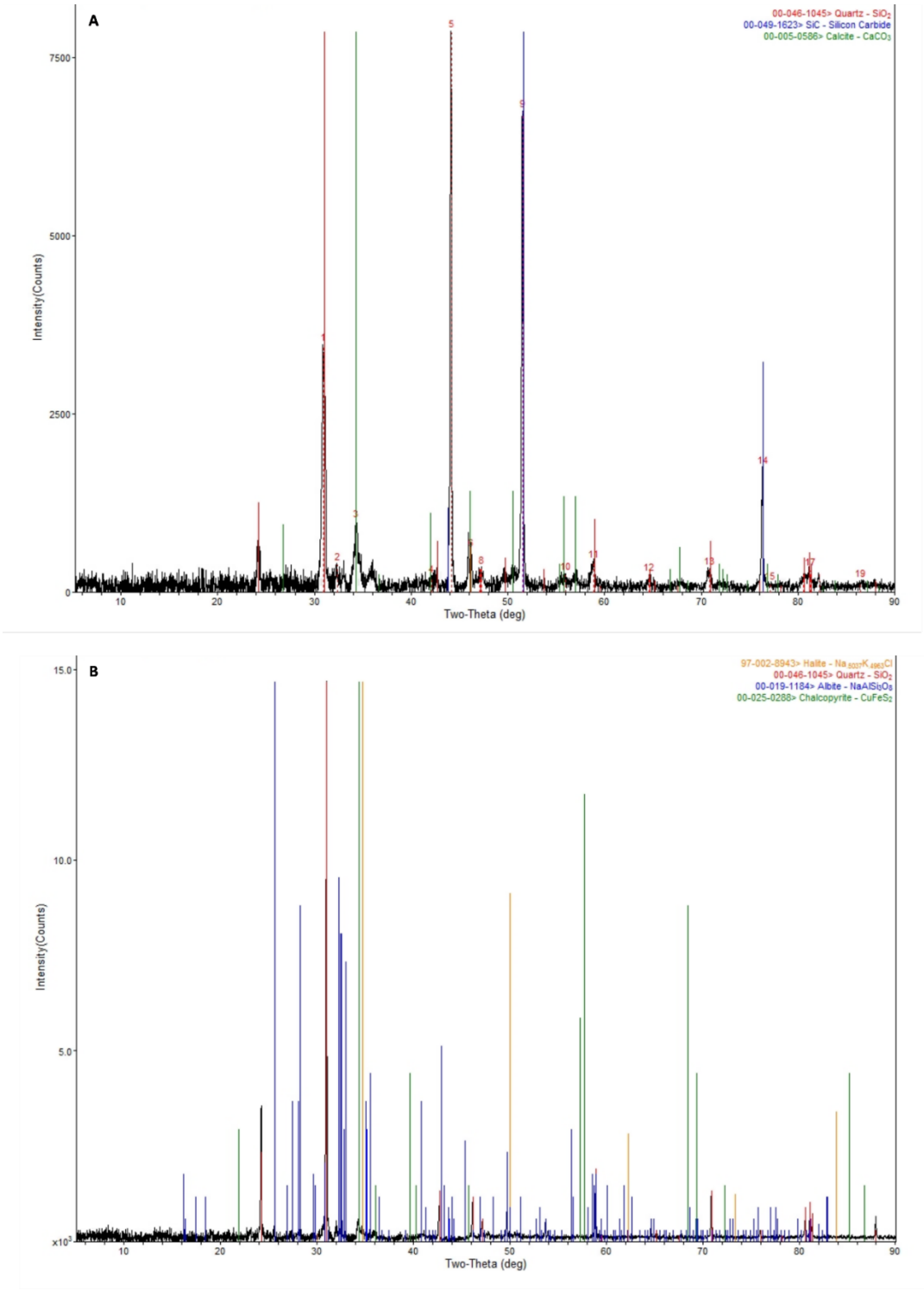


***Figure 3.*** *XRD analyses of: (A)WSBC showing the peak-fitted crystalline phases quartz (red), calcite (green) and silicon carbide (blue), and (B) WSBC showing the peak-fitted crystalline phases quartz (red), albite (blue), halite (yellow) and chalcopyrite (green)*

The XRD spectral features of chalcopyrite in WSBC poorly matched with the chalcopyrite fit from the ICDD and ICSD diffraction pattern databases (Fig. 3B). This implies that chalcopyrite does not belong to the real mineral suite of WSBC. In addition, the finding of silicon carbide, SiC, was unexpected; to our knowledge, there are no reports of SiC in biochar at 550$^{o}$C. Elevated concentrations of Si and C in Si-rich plants, such as rice husk and wheat straw, provide the elements needed to produce SiC under the right thermochemical conditions (Liu *et al.*, 2013). In fact, charcoals have been used in the production of both silicon carbide and calcium carbide (Titiladunayo *et al.*, 2012). However, nucleation of SiC can only be achieved at elevated temperatures between approximately 1500$^{o}$C to 2200$^{o}$C (Nagamori *et al.*, 1986). The pyrolysis temperature of WSBC was considerably cooler, and it is therefore highly unlike that SiC belongs to the mineralogical suite of WSBC, and may instead be an error in the modelling of the diffraction spectra. If SiC was a component of WSBC, it would represent a novel route of producing SiC at low temperature (500$^{o}$C).

In order to find evidence of the SiC presence in WSBC, Raman spectroscopy analysis on unwashed WSBC was performed. The Raman spectra of SiC contains two unique spectral features in the form of the traverse optical (TO) and longitudinal (LO) phono modes observed at ~794 cm$^{-1}$ and ~968 cm$^{-1}$, respectively (Feng *et al.*, 1988; Perova *et al.*, 2010). However, neither the TO or the LO bands were found on the unwashed WSBC and Cr-laden WSBC (see section 3.5.3, Fig. 29), which confirms that the SiC obtained from the XRD modelling does not belong to the mineral suite of WSBC.

*3.1.1 Recalcitrance and stability of WSBC*

The recalcitrance of a biochar is defined as its longevity to remain in soil or aqueous systems, and directly relates to its potential to sequester C. Generally, the recalcitrance of a biochar towards microbial or chemical degradation depends on the C structure of the biochar, which is controlled by the pyrolysis conditions and the composition of the original feedstock (Ahmad *et al.*, 2012). There are two parameters used to describe the stability and degree of carbonization of structural C in biochar: the molar ratios of H/C and O/C. The H/C ratio is used to describe the aromaticity of chars (Ahmad *et al*., 2012), while the O/C ratio is indicative of the physicochemical stability and polarity of biochar (Ahmad *et al*., 2012; Spokas, 2010). The C structures of biochar are formed by multiple processes including dehydration, decarboxylation, dehydrogenation, demethylation and cyclisation as a result of the increased temperature of pyrolysis, leading to thermal decomposition of the original biomass (Wang *et al.* , 2013). The H/C and O/C ratios are both affected by the pyrolysis temperature, since increasing temperatures will lead to greater losses of functional groups, and major elements, such as C, H, N, O (Wang *et al.*, 2013). Thus, values of H/C and O/C are indicators of the relative stability of WSBC when it is exposed to the environment.

The H/C and O/C ratios obtained for WSBC from previous work (Alam *et al.*, 2016) were 0.4 and 0.09, respectively. The initial O/C molar ratio of wheat straw has a value of approximately 0.68 (Spokas, 2010); therefore, a decrease to 0.09 indicates a highly aromatic and stable structure of WSBC. For instance, previous work by (Ahmad *et al*., 2012) obtained H/C ratios for soybean stover and peanut shell derived biochar produced at 700ºC and 300ºC with values of 0.74 - 0.67 and 0.19 - 0.25, respectively. The decrease in H/C ratio was an effect of the highly carbonization and aromaticity of BC produced at 700ºC compared to 300ºC. Furthermore, based on the results from Xiao *et al.* (2016), the association between biochar pyrolysis temperature and H/C ratio could

provide a smart quantitative relationship indicating that H/C ratios can be used to predict pyrolytic temperatures and aromatic cluster sizes. Using the rectangle-like polycyclic aromatic ring model of Xiao *et al.* (2016), WSBC, which has a H/C ratio of 0.4, would have a 4 x 4 benzene ring cluster in a rectangular array, with a theoretical size of 0.984 nm. It is likely that after pyrolysis, most of the WS biomass is converted into condensed 4 x 4 benzene ring structures, as indicated by the drastic change in the post-pyrolysis O/C and H/C ratios. As a result of this process, there is an extensive loss of O-containing functional groups that is also reflected in the low O/C value. The pyrolysis of BC between 500ºC and 700ºC, would turn the pyrogenic amorphous C into turbostratic crystallites ,which are misaligned microscopic graphitic crystals (Das *et al.*, 2015; Xiao *et al*., 2014). Based on the O/C molar ratio, which is less than 0.2, WSBC was also expected to have a degradation half-life of at least 1000 years in the environment (Spokas, 2010; Ok *et al.*, 2015). In addition to the O/C molar ratio, the fixed C matter also correlates to the stability and longevity of biochar. As previously indicated, fixed C values of WSBC were below previous wheat straw biochar studies. The elevated levels of mobile C , or also called labile C, at 33% would be beneficial for microbial growth since microbial communities prefer the labile C fraction originating from the condensation of bio oils during cool down post-pyrolysis of biomass (Fellet *et al*., 2011). However, high Si contents in biochar, as observed in WSBC, are believed to promote greater stability, even in the presence of elevated concentrations of mobile C.

Wheat straw is a poaceous (grass-like) plant capable of containing more than 4% Si, forming amorphous Si phytoliths between the cell walls and lumina (Currie & Perry, 2007). Grass-derived BC, especially from staple cereal crops, such as wheat and rice, tend to contain increased Si levels, as is shown and discussed above. Previous experiments demonstrate that rice husk biochar produced at 500ºC was more recalcitrant towards degradation than biochar produced from

the same biomass at 700ºC (Guo & Chen, 2014). The pyrolysis process impacted the BC ash minerals composition, including Si, changing the amorphous silicon components to more crystalline and stable silicon and quartz components at the higher temperature (Guo & Chen, 2014; Xiao *et al.*, 2014). Pyrolysis of high-Si biomass at 500ºC would have exposed the silicon soon after the oxidation of biochar carbon during heating, followed by re-crystallization of Si concurrent to the aromatization of C, yielding intertwined Si and C containing structures and in some cases the encapsulation of C by crystalized Si (Xiao *et al.*, 2014). More evidence supporting additional stability provided by the spatial relationship between Si and C was provided by SEM imaging (Fig. 2). Abundant 10-micron sized silicon crystals were ubiquitous along the tabular plane of WSBC (Fig. 2C). Residual Si was the dominant form of Si in WSBC, comprising approximately 98% of the total Si. Residual Si is considered highly recalcitrant towards dissolution, providing greater stability to the already stable C pool in WSBC. The results here indicate that WSBC is a relatively stable biochar, due to a combination of condensed aromatic C, and intertwined and encapsulated Si and C structures that result from the 500ºC pyrolysis of Si-rich wheat straw.

In general, WSBC could become a realistic tool for $CO_2$ sequestration, as a result of its high aromaticity and stability, fixed matter and resilient Si-C structures. Furthermore, Ca and K, two key cations required for soils fertility and acidity neutralization, were abundant in WSBC, with 62% and 45% available as exchangeable cations, respectively. The concentrations of P and Mg, 0.78 and 3.96 mg $g^{-1}$, respectively, could contribute considerably to soil fertility. WSBC could be utilized as a soil amendment, especially to Si-deprived soils, since Si deprivation is a significant problem in Asia and often results in structurally weaker plants that are prone to abnormal growth, development and reproduction (Currie & Perry, 2007). Although only 0.44% of Si exists in the leachable form in WSBC as tested in the method of von Gunten et al. (2017), the biochar could

still be used to ameliorate Si-deprived soil because leachable Si in WSBC sums to approximately 207 ppm (Table 3), and more recalcitrant Si is likely to leach from WSBC over longer time scales. Even if greater quantities of Si were provided by WSBC, it would not negatively impact plant growth, as Si is the only element that is not toxic to plants when its concentration exceeds plant uptake. Future studies would be needed to elucidate the recalcitrance of WSBC towards degradation and its ability to release Si, nutrients and cations as a soil amendment.

### *3.2 Kinetics studies of Cr(VI) adsorption and reduction by WSBC*

#### *3.2.1 pH and concentration dependencies of Cr(VI) removal by WSBC*

The concentration of Cr(VI) used for the experiments considerably influenced the aqueous speciation of Cr(VI), since the chromate and dichromate species depend not only on the pH of solution, but also on the total concentration of Cr(VI). Therefore, it was critical to understand the relative abundance of Cr(VI) aqueous species, since the speciation controls the way in which Cr(VI) reacts with the WSBC surface. At elevated Cr(VI) concentrations, chromates will polymerize to produce dichromates (Palmer & Wittbrodt, 1991). Based on the three different Cr(VI) concentrations of 170, 700 and 1300 μM Cr, chromate species were expected to strongly dominate, with only low concentrations of dichromates present. Chromate speciation was also affected by the pH of the environment, with greater protonation of chromates at lower pH. The aqueous chromate speciation is described by the following equations:

$$H_2CrO_4 \leftrightharpoons H^+ + HCrO_4^- \; K = 10^{-0.75} \quad (1)$$

$$HCrO_4^- \leftrightharpoons H^+ + CrO_4^{2-} \; K = 10^{-6.45} \quad (2)$$

$$HCrO_4^- + HCrO_4^- \leftrightharpoons Cr_2O_7^{2-} + H_2O \; K = 10^{2.2} \quad (3)$$

Based on the dissociation constants listed in equations (1-3), $HCrO_4^-$, or hydrogen chromate, are expected to be the dominant chromate species in experiments performed between pH 2 to 3. To verify this, speciation plots were produced using the Medusa speciation software (Puigdomenech, 2013) and PHREEQC (Parkhurst & Appelo, 1999) for Cr(VI) concentrations used in our study (Fig. 4 A, B and D). At a Cr(VI) concentration of 170 μM, hydrogen chromate comprised more than 98% of the total Cr, with the remaining ~2% distributed amongst $H_2CrO_4$, $CrO_4^{2-}$ and dichromate. The concentration of dichromate at 170 μM was 1.30% of the total Cr(VI) concentration. At higher the initial Cr concentrations, 700 μM Cr(VI) and 1300 μM Cr(VI), the proportion of dichromate increased to 4.96% and 8.57%, respectively. Chromic acid ($H_2CrO_4$) and chromate ($CrO_4^{2-}$) concentration for all three total Cr concentrations were 0.0036±0.0001% and 0.0401±0.0016%, respectively. Table 5 summarizes the proportion and total concentration of chromates and dichromates at pH 2, at varying Cr(VI) concentrations.

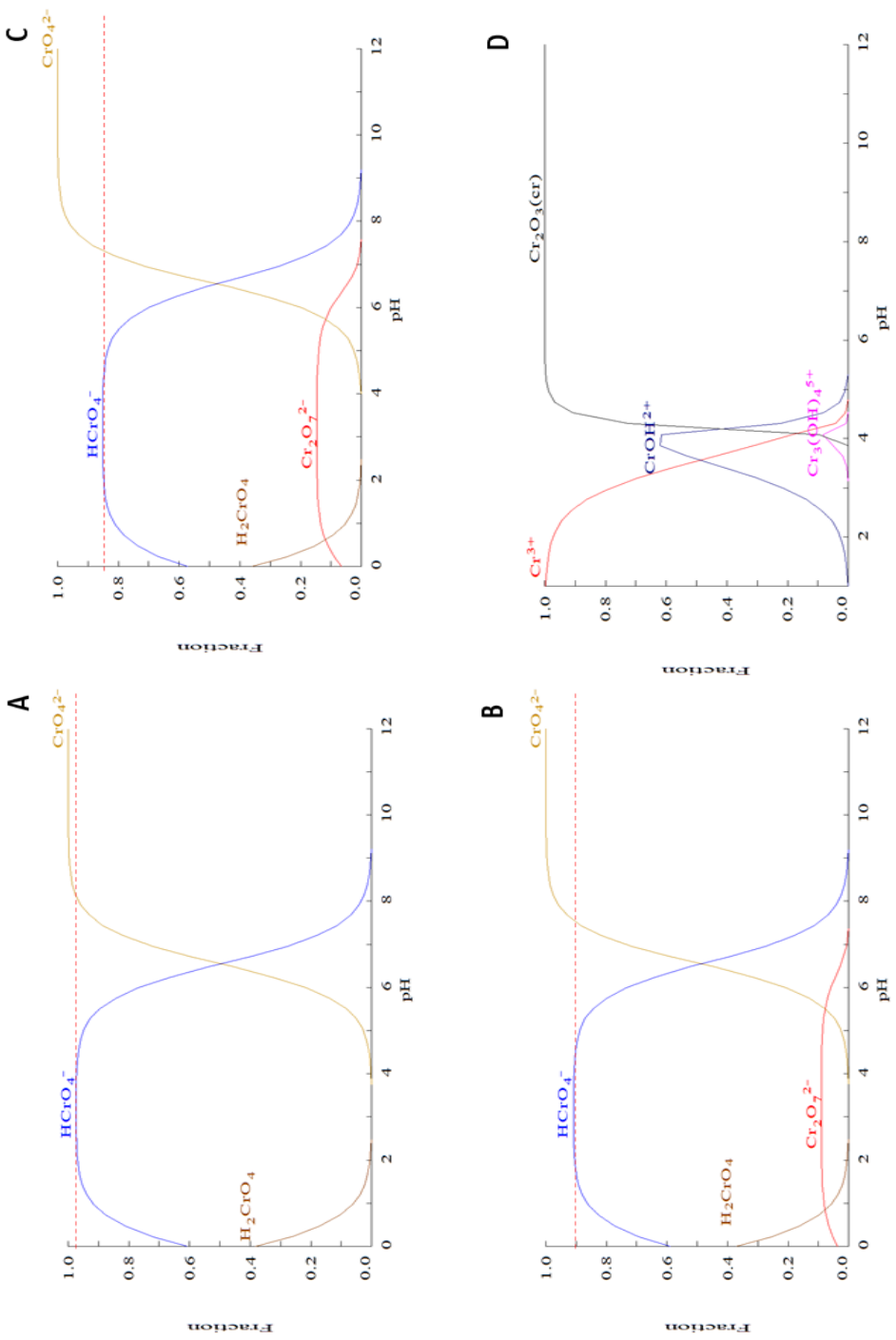


***Figure 4.*** *Calculated Cr(VI) speciation in aqueous systems having total Cr(VI) concentrations of: (A)170 µM, (B)700 µM and (C)1300 µM Cr(VI), at room temperature (23±1°C) and (D) Cr(VI) speciation at 170 µM Cr(III). The red dotted line represents the HCrO4- fraction*

Work by Rai *et al.* (1989) indicated that the removal of Cr(VI) via adsorption is highly dependent on the pH of the system and the speciation of Cr(VI). Since chromates and dichromate are both oxyanions, their intrinsic negative charge would preferentially form complexes with protonated surfaces, especially with greater concentrations of protons ($H^+$) at lower pH. For instance, not only does the pH control the speciation of Cr(VI) in solution, but it is also an important influence on the surface properties of the adsorbent utilized (Deveci & Kar, 2013), in this case WSBC. Previous studies involving the biosorption of Cr(VI) onto biochar have shown that greater Cr(VI) adsorption was achieved at lower pH (Deveci & Kar, 2013; Dong *et al.*, 2011; Mohan *et al.*, 2011; Tytłak *et al.*, 2015). Furthermore, the presence of aromatic structures after the pyrolysis of biomass provides biochar with both disordered polycyclic aromatic hydrocarbon (graphite) sheets capable of transporting π-electrons over long distances, and functional groups capable of adsorbing and reducing metals. Cr(VI), being a powerful oxidant (Cohen *et al*., 2008; Garg *et al*., 2007; Kimbrough *et al*., 1999), could then be reduced to Cr(III) if in contact with an electron donor. It is hypothesized here that with a high enough concentration of protons, and with the likely ability of WSBC to donate electrons, WSBC could adsorb Cr(VI) at low pH, and concurrently reduce Cr(VI) to Cr(III) by electron transfer. Such mechanism of Cr(VI) adsorption is consistent with the degree of Cr(VI) removal from solution observed as a function of pH: 2 > 2.5 > 3. Full removal of Cr(VI) from solution, accounting for only sorption and not considering subsequent Cr(VI) reduction, was achieved at pH 2 and 2.5, but not at pH 3. These results clearly demonstrate that the degree of Cr(VI) sorption to WSBC, and other biosorbents, will be influenced by both the protonation state of surface functional groups and the aqueous speciation of Cr(VI).

| Cr(VI) specie | 170 µM | % | 700 µM | % | 1300 µM | % |
|---|---|---|---|---|---|---|
| $CrO_4^{2-}$ | 6.398E-09 | 3.764E-05 | 2.551E-08 | 3.645E-05 | 4.588E-08 | 3.529E-05 |
| $HCrO_4^-$ | 1.677E-04 | 9.866E-01 | 6.649E-04 | 9.499E-01 | 1.188E-03 | 9.139E-01 |
| $H_2CrO_4$ | 7.085E-08 | 4.168E-04 | 2.804E-07 | 4.006E-04 | 4.999E-07 | 3.845E-04 |
| $Cr_2O_7^{2-}$ | 2.202E-06 | 1.295E-02 | 3.474E-05 | 4.963E-02 | 1.114E-04 | 8.571E-02 |
| **Total** | 1.700E-04 | | 6.999E-04 | | 1.300E-03 | |

***Table 5.*** *Distribution of chromate and dichromate species at pH 2, as a function of Cr(VI) concentration*

The extent of sorption was also controlled by the density of surface sites on WSBC, especially since there is a fixed concentration of surface functional groups per unit of surface. (Rai *et al.*, 1989). The measured BET surface area (SA) of WSBC was 26.64 $m^2$ $g^{-1}$, a greater SA than for other wheat straw derived biochar produced at similar pyrolysis conditions (Ahmad *et al.*, 2014; Cao *et al.*, 2016; O'Toole *et al.*, 2013). The obtained SA value of our WSBC was influenced by the elevated content of ash during the pyrolysis process and the pyrolysis temperature. Ash produced during pyrolysis is known to affect and reduce biochar SA by blocking the micro- and meso-porosity; therefore, it is certain that the SA of unwashed WSBC was affected by the relatively higher ash content. As indicated by Raveendran & Ganesh (1998), the ash content in the biochar influences the adsorption rate of iodine by directly affecting its SA. As pyrolysis temperature increases during biochar production, so does the SA of biochar, yet the concentration of surface functional groups will decrease, particularly for O-containing functional groups (Ahmad *et al.*, 2014). This explains why biochars produced at high pyrolysis temperatures, having elevated SA, tend to be physically or chemically treated to regain the surface functionality lost during pyrolysis, while preserving the high SA developed.

It should be noted, however, that generalization of SA values and surface functionalities cannot be made from biochar produced from the same biomass, since even biomasses of the same type can vary in their chemical and structural characteristics. For example, previous biochar work

by Mohanty *et al.* (2013) produced wheat straw derived biochar at 450°C, with both slow and fast heating rates, yielding SA values of 178 and 184 $m^2 g^{-1}$, respectively. Wheat straw derived biochar, produced with both low and high heating rates by Mohanty *et al*., (2013), exhibited greater SA than WSBC (26.64 $m^2 g^{-1}$). An increased in SA for WSBC could have been achieved by the application of post-pyrolysis treatment techniques, such as simple biochar washing or de-ashing procedures (Raveendran & Ganesh, 1998).

The kinetics experiments focused on Cr(VI) concentrations between 1.7 μM and 13 μM, which fell within the known ranges of Cr(VI)-containing wastewaters (Owlad & Aroua, 2009). Results indicate that both the Cr(VI) sorption (Fig. 5C, 5D) and reduction (Fig. 5A, 5B) kinetics were similar, and followed an exponential decay trend. The adsorption mechanism involves the binding between Cr(VI) oxyanion species and protonated surfaces of WSBC, which was then limited by the degree of protonation of the system, while the reduction capacity of Cr(VI) to Cr(III) by WSBC was directly affected by the adsorption mechanism, since adsorption must first happen before any electron transfer can occur. Previous studies of Cr(VI) adsorption to biomass have shown that adsorption of Cr(VI) oxyanions at acidic pH is rapid (Tytłak *et al*., 2015).

Our data suggests that the Cr(VI) sorption process involved two phases: a short-lived and faster initial removal period, followed by a longer period of slower Cr(VI) removal from solution. Previous studies demonstrated that biochar could remove between 78% and 80% of the total initial Cr(VI) within the first two hours (Dong *et al.*, 2011; Wang *et al.*, 2010). In experiments with 170 μM Cr(VI), WSBC removed between 50% to 57% of the total Cr(VI) from solution within 2 hours for experiments conducted at pH 2, 2.5 and 3 (Fig. 5C). The kinetics experiments conducted with 700 μM Cr at pH 2 also displayed a similarly fast initial removal mechanism, with as much as 48% of Cr(VI) removed during the first 2 hours (Fig. 5D). The faster initial removal of Cr(VI) displayed

by WSBC was not as effective as the initial removal rates from Dong *et al*. (2011) and Wang *et al*. (2010). This finding might suggest that WSBC is a less effective biochar in comparison to the sugar beet tailing derived biochar and the wheat straw derived biochar from those respective studies. Yet, significant differences including the biosorbent loading and pH between those studies and the current study can also explain the relatively lower efficiency of WSBC to remove Cr(VI) within the first two hours. The Cr(VI) removal experiments using sugar beet tailing derived biochar by Dong *et al*. (2011) were produced under similar pH conditions (pH 2), however, their biochar loading (2 g $L^{-1}$) was twice as much as the one used in this study (1 g $L^{-1}$). Twice the biochar loading would provide twice the number of available sorption sites, resulting in more rapid removal of Cr(VI) from solution. On the other hand, the removal of Cr(VI) using wheat straw derived biochar by Wang *et al*. (2010), was elucidated using the same biosorbent loading as this study (1 g $L^{-1}$); nonetheless, their pH was fixed at 1 while this study focused in pH between 2 to 3. This comparison of rates between similar Cr(VI) removal studies using biochar indicates that biosorbent loading, pH and initial Cr(VI) concentration can influences Cr removal kinetics.

The rather rapid initial Cr(VI) removal rate of WSBC decreased after the first two hours of reaction, followed by a considerably slower removal rate thereafter. Generally, we found that WSBC has the ability to remove at least 88% of the initial 170 μM Cr(VI) from solution at pH 3 after approximately 15 days, and fully removes this concentration of Cr(VI) from solution at pH 2 and 2.5 after 4.51 and 12.41 days, respectively. The removal of 661.12 μmol of Cr(VI) was per gram of WSBC was achieved at the higher concentration of 700 μM Cr(VI) at pH 2 in 89.18 days. 936.21 μmol of Cr(VI) was removed per gram of WSBC when the initial Cr(VI) concentration was 1300 μM after 66.08 days. Full removal of Cr(VI) from solution was only achieved at lower Cr(VI) (170 μM Cr(VI)) concentration and at pH 2 and 2.5. WBSC did not have the ability to fully

remove Cr(VI) at pH values greater than 2.5, or at concentrations of Cr(VI) higher than 170 μM Cr(VI) in less than 2.5 months, with a loading of 1 g $L^{-1}$ WSBC. In summary, WSBC was an effective biosorbent for Cr(VI) removal in acidic media, with total sorption taking between days to months for complete Cr(VI) removal from aqueous systems.

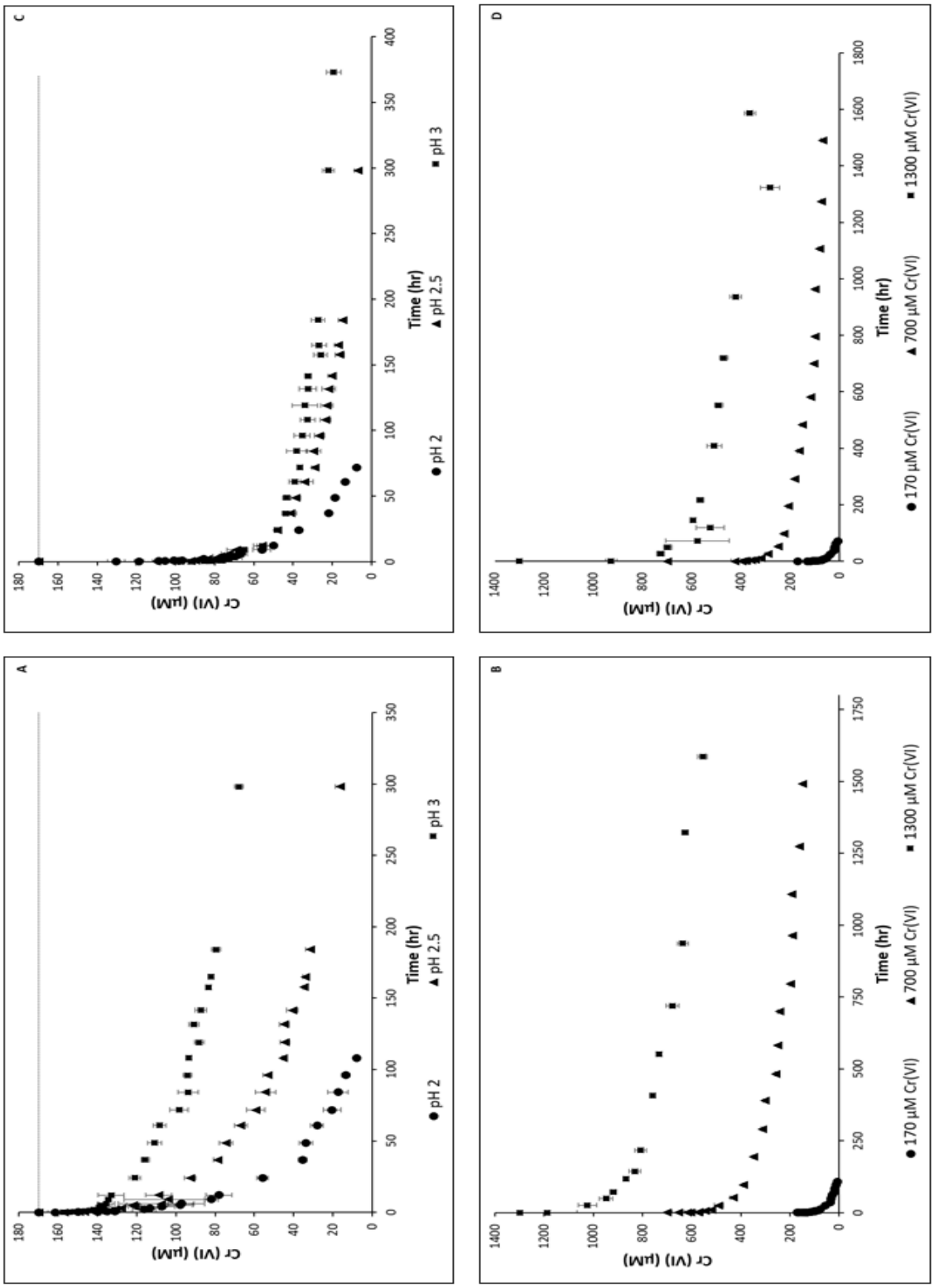


***Figure 5.*** *Change in Cr(VI) concentration from reduction and adsorption experiments. Reduction plots of Cr(VI) μM vs Time (hr) as a function of pH (A) and Cr(VI) concentration (B). Sorption plots of Cr(VI) μM vs Time (h) as a function of pH (C) and Cr(VI) concentration (D)*

While the adsorption of Cr(VI) decreases the aqueous Cr concentration, reduction to Cr(III) via the transfer of electrons from the biochar provides a mechanism to immobilize Cr. Without reductive immobilization, the adsorbed Cr(VI) could be desorbed to solution if the system were to experience an increase in pH. With this in mind, the Cr(VI) reduction capability of WSBC was measured concurrently to the Cr(VI) sorption experiments, that is, as a function of pH (Fig. 5A) and Cr(VI) concentration (Fig. 5B). As mentioned above, Cr(VI) adsorption kinetics matched closely to Cr(III) reduction kinetics, suggesting that adsorption was the rate-limiting step in chromate reduction, and not electron transfer from WSBC. However, there is a secondary lag between the reduction and the sorption rates, likely caused by the time needed to transfer electrons following Cr(VI) adsorption. Complete reduction of hexavalent chromium requires a three-electron transfer, along with protons, to produce Cr(III), as follows (Wang *et al.*, 2010):

$$Cr_2O_7^{2-} + 14H^+ + 6e^- \leftrightharpoons 2Cr^{3+} + 7H_2O \; E_0 = +1.33V \quad (5)$$

$$CrO_4^{2-} + 8H^+ + 3e^- \leftrightharpoons Cr^{3+} + 4H_2O \; E_0 = +1.48V \quad (6)$$

$$HCrO_4^- + 7H^+ + 3e^- \leftrightharpoons Cr^{3+} + 4H_2O \; E_0 = +1.35V \quad (7)$$

$$H_2CrO_4 + 6H^+ + 3e^- \leftrightharpoons Cr^{3+} + 4H_2O \; E_0 = +1.33V \quad (8)$$

Based on the Cr(VI) concentration vs. time graphs, we can empirically describe the reduction of Cr(VI) based on pH and concentration changes. Although Cr(VI) sorption by WSBC was rapid for the first two hours, reduction of Cr(VI) to Cr(III) was slower. While the amount of Cr(VI) removed via adsorption for pH 2, 2.5 and 3 was between 50% to 57% within the first two hours of experimentation, adsorption of Cr(VI) appeared to have a short lived instantaneous sorption mechanism. Within the first two minutes, WSBC adsorbed between 26% and 45% of the initial Cr(VI) concentration, with an average of 35±8% of Cr(VI) removed to adsorption in the first two minutes (Fig. 5C and 5D). During the same time span of approximately two minutes,

reduction of Cr(VI) to Cr(III) ranged between 5% and 9%, with an average of 7±1% of removal of Cr(VI) via reduction by WSBC. Reduction of Cr(VI) to Cr(III) greatly lagged the adsorption rates even when the initial Cr(VI) concentrations were relatively low. Equations (5 – 8) describe how the reduction of chromates or dichromates requires both electrons and protons, and from this we can infer that the rate of Cr(VI) reduction depends both on the efficiency of electron transfer from WSBC and pH. The ratio between Cr(VI), protons and electrons is 1:7:3, and so the availability of protons strongly controls the Cr(III) formation rate. Generally, Cr(VI) is a powerful electron acceptor, and will be easily reduced to the trivalent form under highly acidic conditions and if electron donors are present. In our experiments conducted between pH 2 to 3, the proton concentration in solution was well-buffered; only a limited pH change was observed, with a ±0.09 pH unit change at pH 2, ±0.08 pH unit change at pH 2.5, and ±0.50 change at pH 3, as a result of the consumption of protons by the reduction of Cr(VI) to Cr(III). This indicates that biosorbents, such as WSBC, could be ideally applied for treating acidic industrial effluents, such as electroplating wastewaters and acid mine drainage that often contain elevated Cr(VI) concentrations in acidic system. It is also important to mention that no dissolution of WSBC was observed at any pH. This can be correlated to the high recalcitrance and stability of WSBC (see section 3.1.1). In particular, although Si in the biochar will slowly leach over time, it will remain relatively stable under acidic pH since the facile dissolution of Si only occurs above pH ~9 (Alexander *et al.*, 1954). Therefore, high-Si WSBC can thrive in low pH systems in comparison to many other sorbents which would more rapidly dissolve at such a pH range (2 - 3).

*3.2.1.1 Pseudo-first-order kinetics model for Cr(VI) reduction at pH 2, 2.5, and 3*

Kinetics data from the Cr(VI)-WSBC metal reduction experiments were modeled to determine the order and rates of Cr(VI) reduction kinetics for experiments conducted at pH 2, 2.5, and 3. The adsorption and reduction of Cr(VI) by WSBC was also tested at circumneutral pH (pH 6.7); however, no measurable amount of Cr(VI) was removed from solution during the span of these batch experiments (data not shown). Such results influenced the decision to focus on applications of WSBC at acidic pH, especially between 2 to 3. Previous Cr(VI) reduction studies were able to demonstrate that the removal of Cr(VI) using biosorbents usually followed a pseudo-first-order kinetics model (Hsu *et al.*, 2009). A pseudo-first order kinetic model describes a second-order reaction that appears to be first-order, and it arises when one of the reactants in the system is presented in great excess, thus regarded as a "constant", over the other reactant in the system. Our data kinetics were plotted as $Ln(C/C_0)$ vs. time (h), where the $C_0$ is the initial Cr(VI) concentration or Cr(VI) at t = 0 and C is the Cr(VI) concentration as time increases. Such plots are used to determine the pH dependency and potentially calculate the intrinsic (pH independent) rate constant. Model first-order fits are good evidence that the reduction of Cr(VI) by WSBC in acidic solution followed a pseudo-first-order reduction rate law (Fig. 6). The linear correlation coefficient, *R*, for the model fits to pH experiments at pH 2, 2.5 and 3 were 0.962, 0.904 and 0.820, respectively. These high *R* values indicate that Cr(VI) reduction by WSBC matched the pseudo-first-order model. In order to determine the true order of the reaction, a very similar approach to the studies conducted by Gould (1982) was done; instead of plotting the natural log of the rate constant (*K*') as a function of natural log of the activity of protons, the log of (*K*') was plotted against the pH of the pH series experiments.

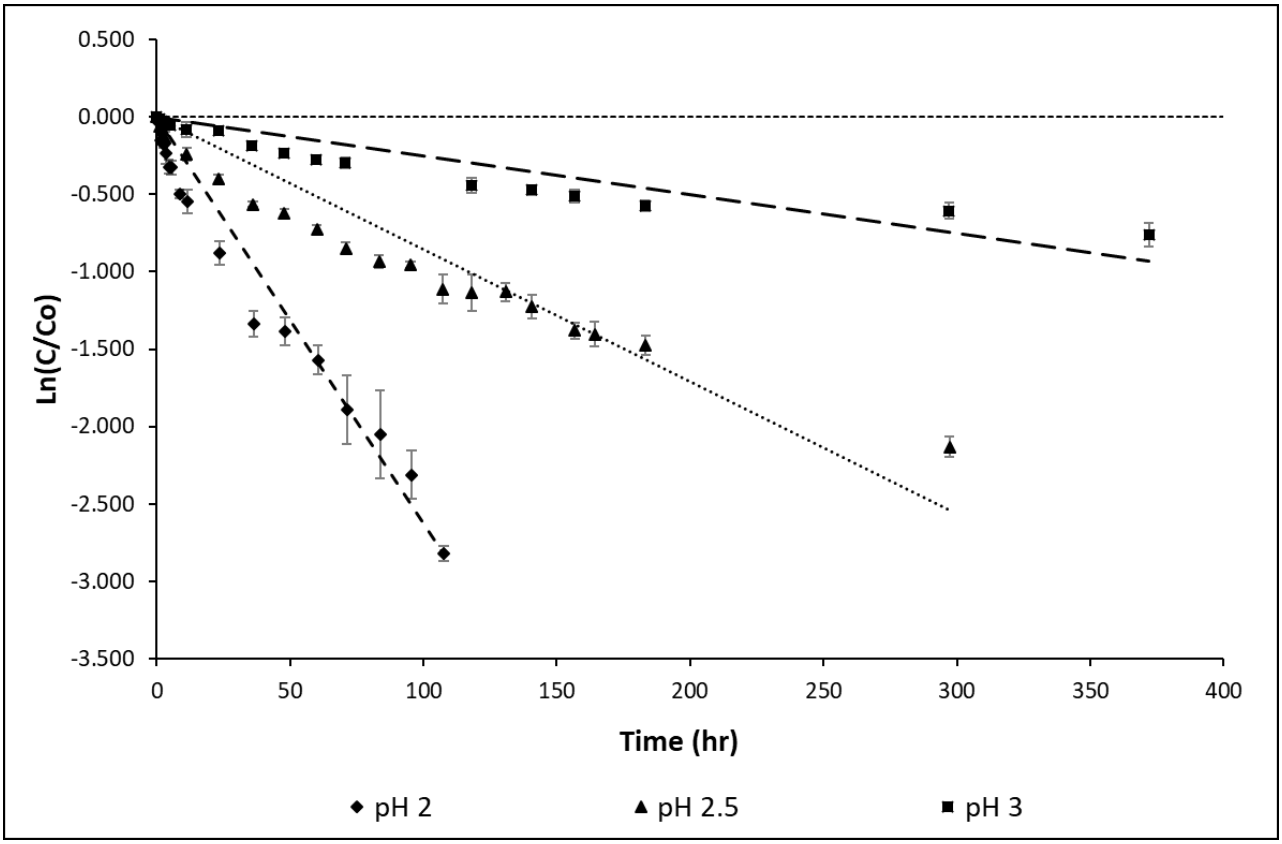


***Figure 6.*** *Pseudo-first order fits of Cr(VI) as a function of pH 1 g $L^{-1}$ WSBC and 170 µM Cr(VI)*

The high heterogeneity of the surface of biochar, as indicted by previous papers (*e.g.* Agrafionti *et al.*, 2014a; Agrafioti *et al.*, 2014b; Inyang *et al.*, 2016), adds challenges to developing acceptable reduction kinetics models. However, the application of a rate law to the reduction data, as we have done here, in some cases allows for further modeling of concentration-independent rate constants ($K_{int}$). The first step is to calculate the observed rate ($K_{obs}$), which accounts for the instantaneous change in Cr(VI) concentration within any given time frame during the Cr(VI) reduction process, according to:

$$\frac{\Delta Cr(VI)}{\Delta(Time)} = K_{obs} \quad (9)$$

where $K_{obs}$ is recorded in units of μM $hr^{-1}$. From the $K_{obs}$ values, it is then possible to obtain *K*', a general intrinsic rate, which considers initial aqueous Cr(VI) concentrations:

$$K_{obs} = K'[\mathrm{Cr(VI)}] \quad (10)$$

the resulting *K*' is in units of $hr^{-1}$, and is the concentration-independent intrinsic rate constant. In order to calculate $K_{int}$, an even more general rate constant that is independent of both the initial Cr(VI) concentration and solution pH, the *K*' values for the pH 2, 2.5, and 3 Cr(VI)-WSBC experiments were calculated and then plotted against the pH. The fit to the log(*K*') vs pH (-log $\alpha_{[H+]}$) data was also linear, indicating that Cr(VI) reduction had a dependency on pH. The slope of the plot from the Log(*K*') vs pH had an almost perfect fit with an $R^2$ value of 0.99 and a slope of -0.757 (Fig. 7). A slope value of -1 would indicate a perfect first-order dependence on protons; while the calculated slope is somewhat less, because this is a pseudo-first-order system, it was deemed the rate to be consistent with first order in pH.

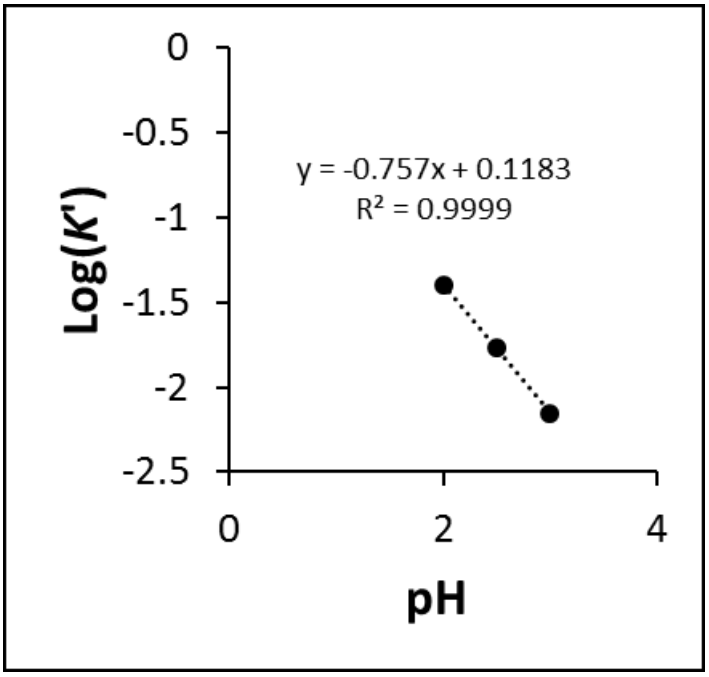


***Figure 7.*** *Log of the rate constant as a function of pH*

The pH-independent intrinsic rate of Cr(VI) reduction by WSBC was calculated from *K*'. As discussed above, the intrinsic rate ($K_{int}$) is useful because it can be used to calculate the instantaneous rate of Cr(VI) reduction ($K_{obs}$) at any given Cr(VI) concentration and pH. The intrinsic rate of Cr(VI) was calculated by the following equation:

$$K_{int} = K'[\mathrm{H}^+] \quad (11)$$

where *K*' was in units of $hr^{-1}$, $[H^+]$ was in M and $K_{int}$ was in $hr^{-1}$ $M^{-1}$. The overall intrinsic rate, combining data from the three experiments at pH 2, 2.5 and 3 at 170 µM Cr(VI), was calculated as 5.459 ± 1.502 $M^{-1}$ $hr^{-1}$. The overall rate law for Cr(VI) reduction by WSBC, a combination of equations 9, 10 and 11, is:

$$-\frac{d[\mathrm{Cr(VI)}]}{dt} = K_{obs} = K_{int}[\mathrm{Cr(VI)}][\mathrm{H^+}] \quad (12)$$

The rate law described in equation 12 allows for the calculation of the reaction rates at any pH and aqueous Cr(VI) concentration. From the calculated rate constants (*K'*), reaction half-lives were then determined for the pH series experiments. In addition, the rate constants were compared with the results of similar Cr(VI) reduction studies utilizing biosorbents. For example, Hsu *et al.* (2009) utilized black carbon derived from burning rice straw (RSBC) to reduce Cr(VI) as a function of pH between pH 3 and 7. The rate constants determined in our study were consistent with those in Hsu *et al.* (2009) (Table 6). Although these authors did not conduct Cr(VI) reduction studies at pH lower than 3, their data show increasingly rapid Cr(VI) reduction with decreasing pH as in our study. At pH 2, the natural log of the rate constant of Cr(VI) reduction by WSBC was -1.40, corresponding to a half-life of 17 hours, while the natural log of Cr(VI) reduction by black carbon at pH 3 was -1.56, a half-life of 25 hours. This direct comparison of Cr(VI) reduction at pH 3 indicates that RSBC had greater reduction capacity at pH 3, making black carbon a better biosorbent for Cr(VI) removal via reduction than WSBC. It might also be expected that BC has greater Cr(VI) reduction capacity at pH 2 than does WSBC. Relatively higher capacity of RSBC over WSBC was attributed to the greater biosorbent loading, which used twice as much biomass (2 g $L^{-1}$) as used in this study, and that RSBC underwent HCl and HF treatment to remove Si and inorganic salts to increase its surface area up to 249 $m^2$ $g^{-1}$. Overall, the unwashed WSBC with a loading of 1 g $L^{-1}$ efficiently removes Cr(VI) from acidic solutions, and with higher loading and pretreatments, WSBC could provide even greater removal rates.

| Sorbent | pH | $K'$ ($hr^{-1}$) | log $K'$ ($hr^{-1}$) | half life (hr) | $K_{int}$ ($M^{-1}$ $hr^{-1}$) | ref |
|---|---|---|---|---|---|---|
| WSBC | 2 | 0.040 | -1.40 | 17 | 5.459 ± 1.502 | this work |
| | 2.5 | 0.017 | -1.77 | 41 | | |
| | 3 | 0.007 | -2.15 | 99 | | |
| RSBC* | 3 | - | -1.56 | 25 | - | Hsu et al., 2009 |
| | 4 | - | -2.22 | 116 | | |
| | 5 | - | -2.74 | 381 | | |
| | 6 | - | -3.06 | 803 | | |
| | 7 | - | -3.62 | 2886 | | |

RSBC* refers to black carbon produced from rice straw

***Table 6.*** *Pseudo-first-order rate constants and half-lives of Cr(VI) reduction by WSBC at pH 2, 2.5 and 3, in comparison with the reactions rates and half-lives of Cr(VI) reduction by RSBC found in literature*

*3.2.2 Removal kinetics of Cr(VI) as a function of Cr(VI) concentration*

The reduction of Cr(VI) by WSBC was also tested as a function of Cr(VI) concentration. As previously mentioned, the concentrations of Cr(VI) were 170 μM, 700 μM and 1300 μM Cr(VI). Plotting the natural log of $C/C_0$ as a function of time produced similar pseudo-first order fits (Fig. 8). First-order kinetics were again plotted for the reduction of Cr(VI) across the three different initial Cr(VI) concentrations tested (Fig. 8).

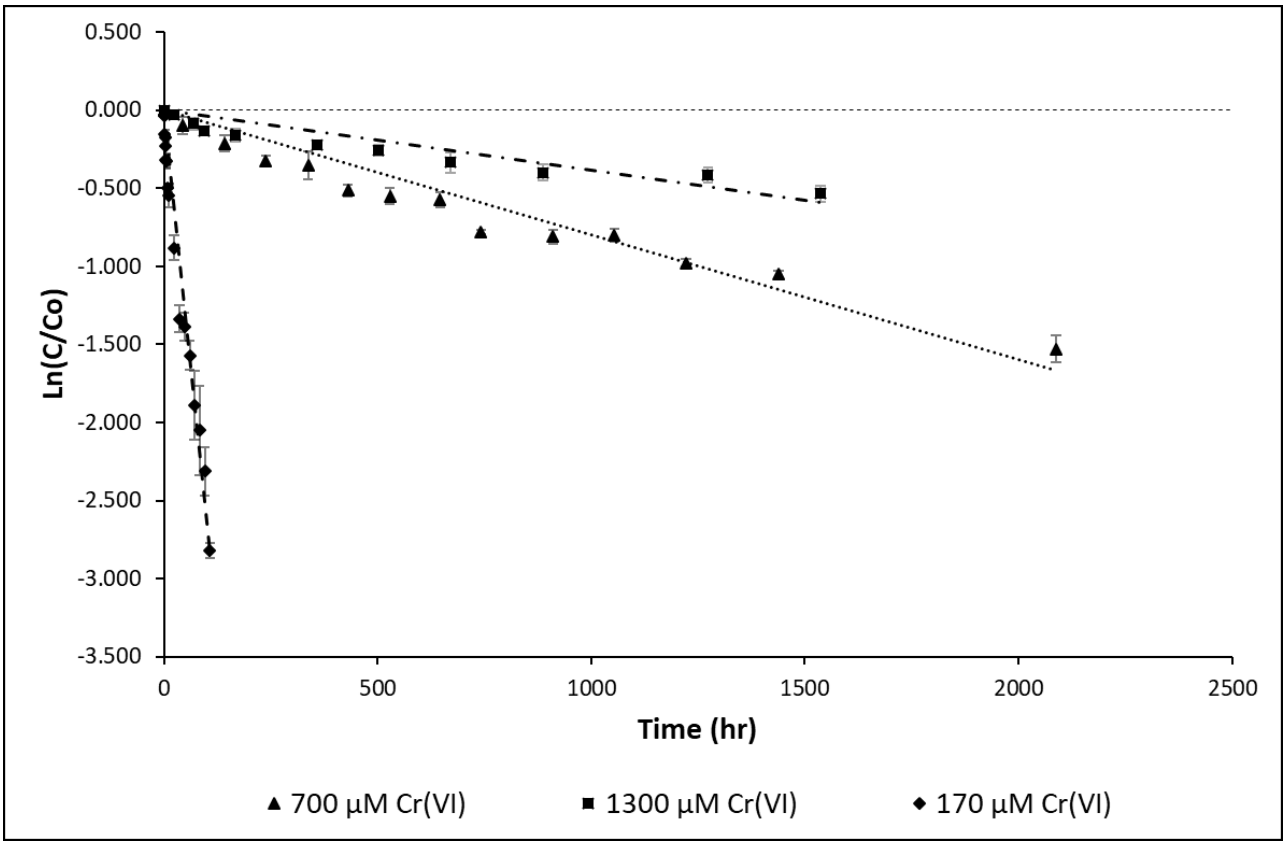


***Figure 8.*** *Pseudo-first order fits of Cr(VI) as a function of Cr(VI) concentration with 1 g $L^{-1}$ WSBC and pH 2*

The system itself became more complex to analyze at increasing Cr(VI) concentration, due to the considerable changes in the proportions of chromate and dichromate species in solution with increasing total Cr(VI) concentration in solution (see Section 3.2.1.). In the pH series experiments, a simpler system involving a constant and initially low concentration of Cr(VI) lead to only minor changes in the various chromate and dichromate proportions and, therefore, limited the impact on the overall Cr(VI) reduction mechanism. However, as the concentration of Cr(VI) increases in these experiments, the proportion of both chromate and dichromate varies, likely affecting the overall reduction mechanism. To determine if the pseudo-first-order model was the best fit for data from the increasing Cr(VI) concentration experiments, a comparison between pseudo-first-order and second-order-plots kinetics fits was made (Figs. 9 – 11).

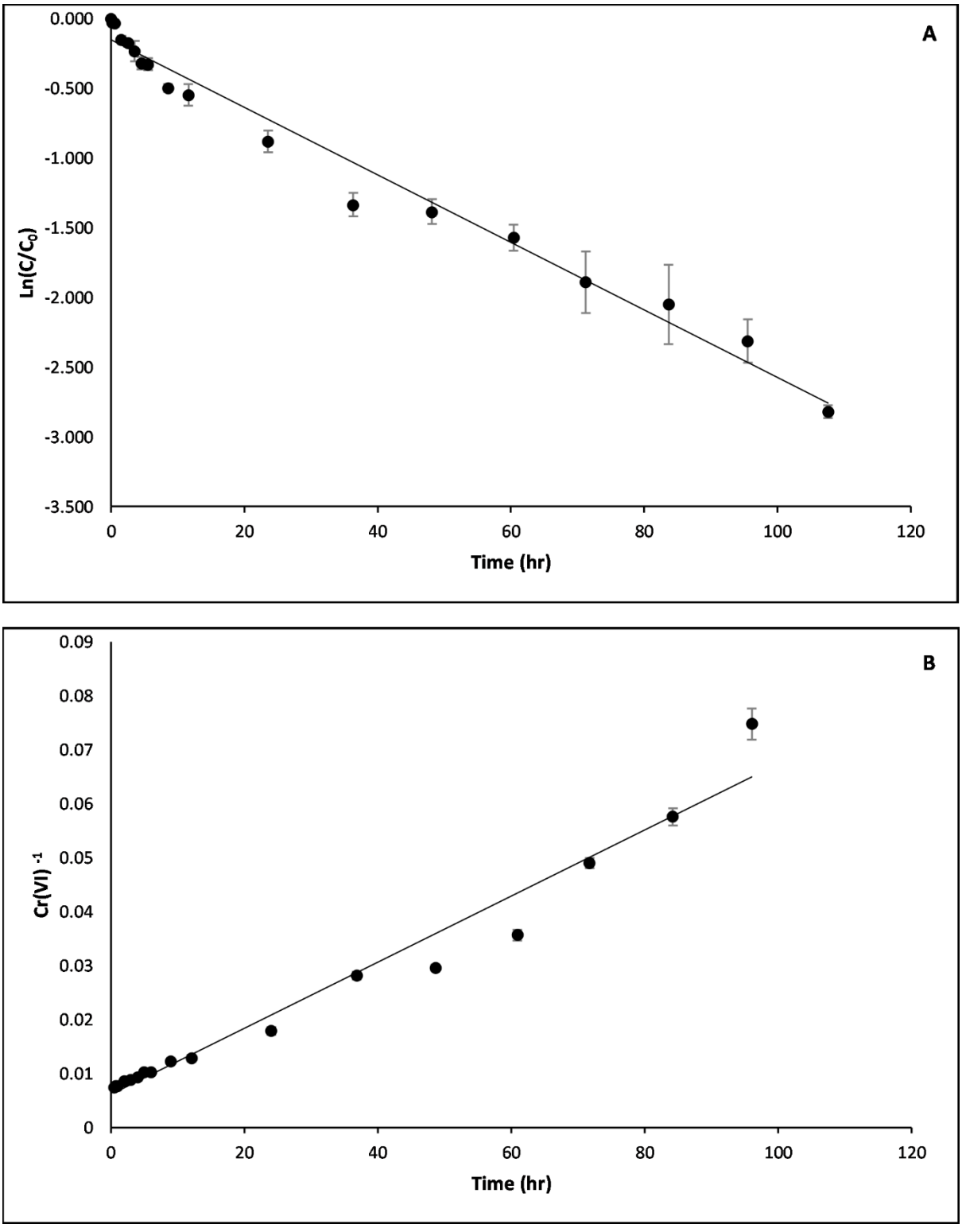


***Figure 9.*** *Kinetics plots of Cr(VI) reduction with an initial Cr(VI) concentration of 170 µM. (A) Pseudo-first-order reaction model and (B) second-order reaction model*

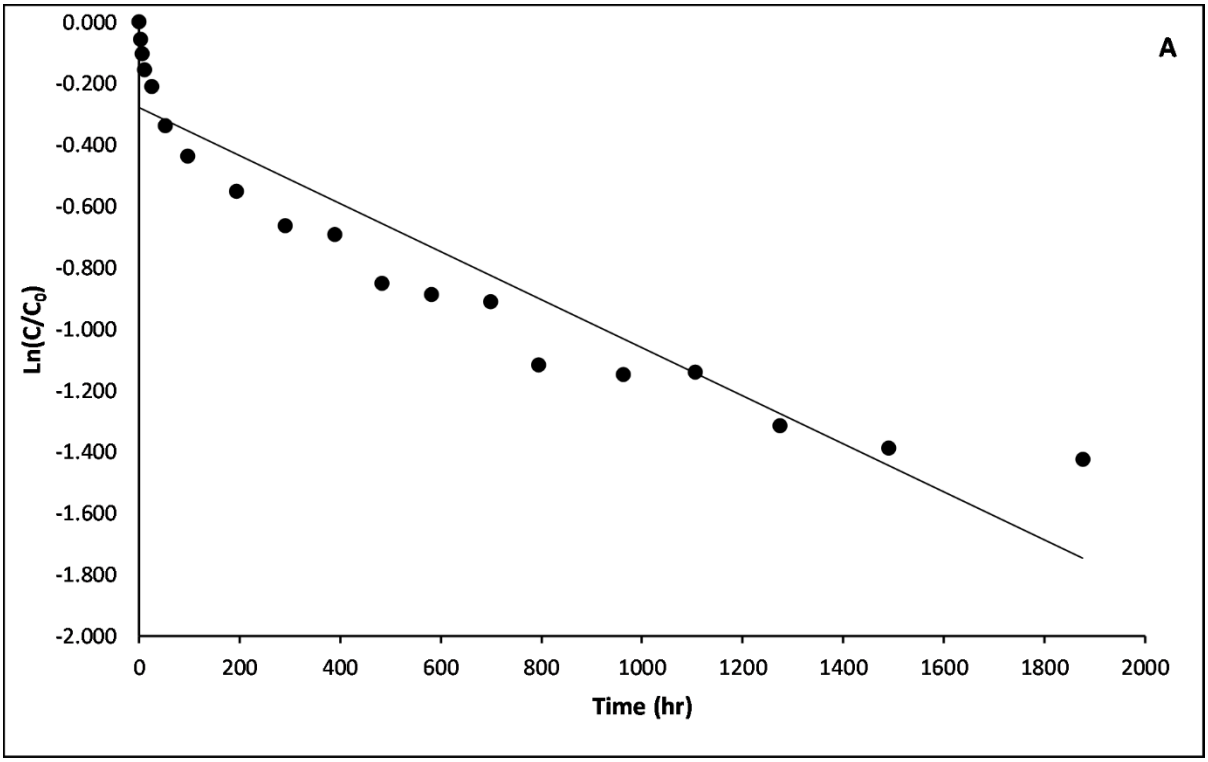


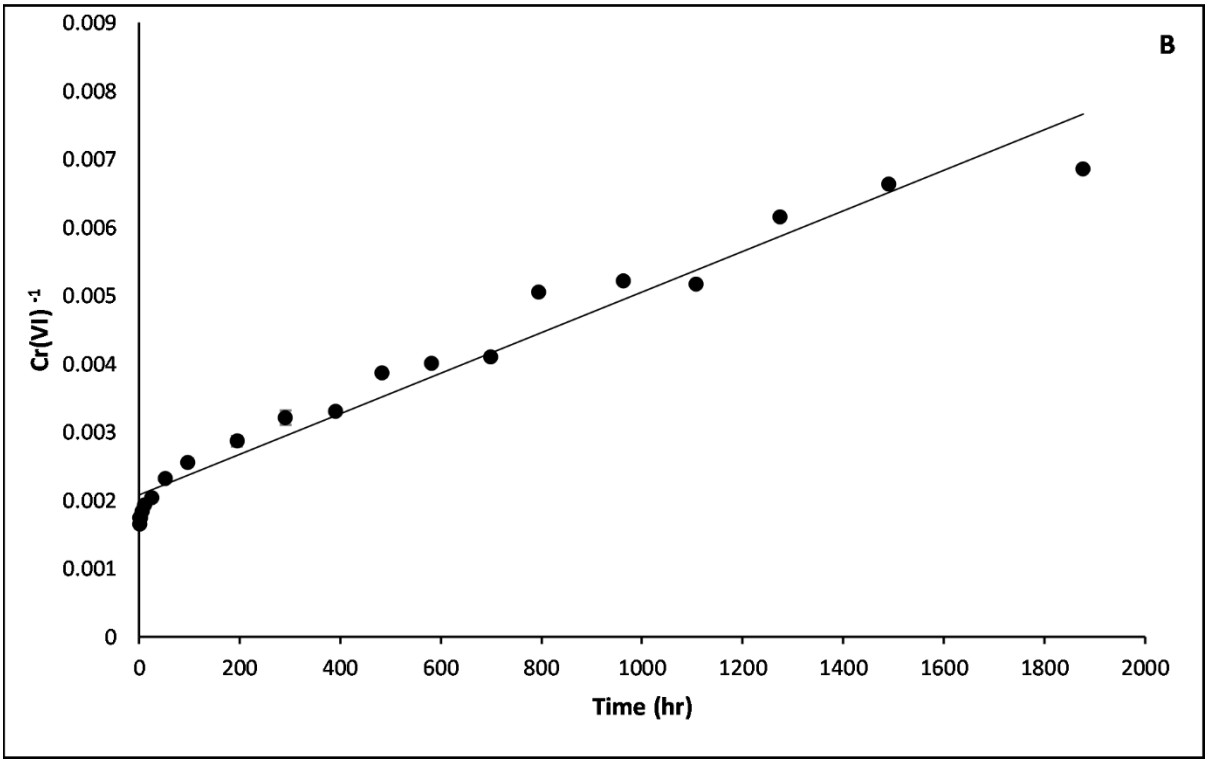


***Figure 10.*** *Kinetics plots of Cr(VI) reduction with an initial Cr(VI) concentration of 700 µM. (A) Pseudo-first-order reaction model and (B) second-order reaction model*

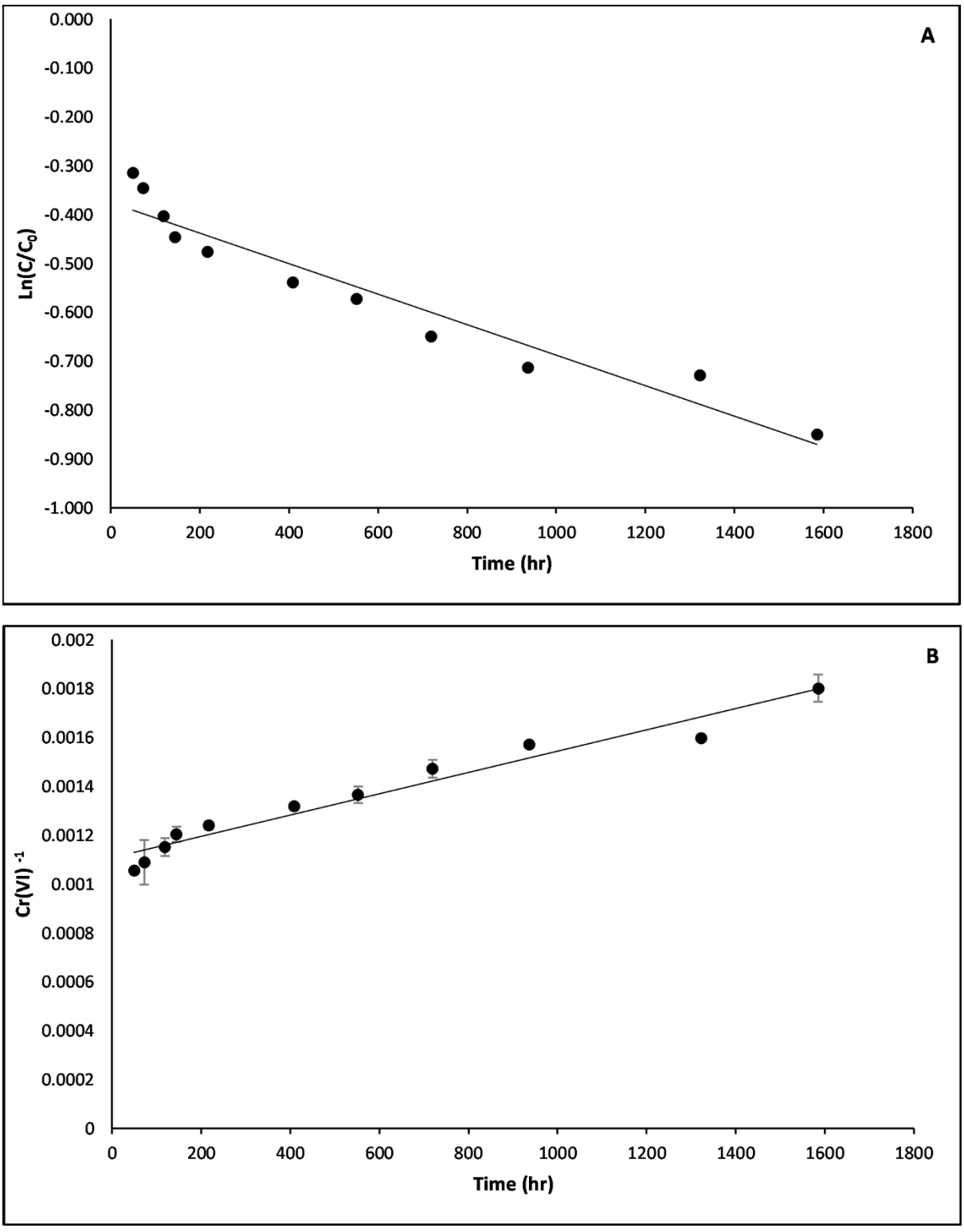


***Figure 11.*** *Kinetics plots of Cr(VI) reduction with an initial Cr(VI) concentration of 1300 μM. (A) Pseudo-first-order reaction model and (B) second-order reaction model*

Comparison between the pseudo-first-order reaction (Figs. 9A, 10A, 11A) and second-order reaction models (Figs. 9B, 10B, 11B) were made to determine if the increase of Cr(VI) concentration affected the pseudo-first-order model fits achieved in the pH series (Fig. 6). The coefficients of determination are summarized in Table 7 for both pseudo-first-order and second-order Cr(VI) reduction models for all three initial concentrations utilized. At elevated initial Cr(VI) concentrations, especially at 700 and 1300 μM Cr(VI), the second-order reduction kinetics model provides a better fit than does the pseudo-first-order model. At 700 μM Cr(VI), the pseudo-first-order kinetics model gives an $R^2$ value of 0.8815, while the $R^2$ of the second-order kinetics model was 0.9632. Identical results were obtained from the experimental data of the experiments utilizing initial 1300 μM Cr(VI). The second-order kinetics model yielded a coefficient of determination of 0.9545, while the pseudo-first-order kinetics model gave 0.9302. Yet, at lower concentrations, 170 μM Cr(VI), contrasting results to the 700 and 1300 μM Cr(VI) were achieved. The coefficient of determination for the pseudo-first-order and second-order kinetics model at 170 μM Cr(VI) are 0.9803 and 0.9686, respectively. The comparison between models at lower Cr(VI) clearly indicates that the pseudo-first-order model has a better fit for the 170 μM Cr(VI), consistent with the pH series data fits (Fig. 6). However, employing the second-order kinetics model results in better fits for 700 and 1300 μM Cr(VI) reduction data.

| Cr(VI) (μM) | 1st order $R^2$ | 2nd order $R^2$ |
|---|---|---|
| 170 | 0.9803 | 0.9686 |
| 700 | 0.8815 | 0.9632 |
| 1300 | 0.9302 | 0.9545 |

***Table 7.*** *Coefficient of determination for both first- and second-order reduction kinetics models with increasing initial Cr(VI) concentration*

A possible explanation for the change in modeled kinetics order between the 170 μM Cr(VI) and higher concentrations experiments might be attributed to changes in Cr(VI) speciation within the system. An increase in chromate concentration would give rise to greater polymerization, potentially adding complexity to the system. Work by Park *et al*. (2007) demonstrated that the removal rate of Cr(VI) as a function of initial Cr(VI) concentration and biosorbent concentration followed a pseudo-first order kinetics model. On the other hand, removal of approximately 480 μM Cr(VI) with biochar by Deveci & Kar (2013) attributed the removal mechanism to follow a pseudo-second order kinetics model. At much greater Cr(VI) concentrations, the kinetics model is expected to deviate from the pseudo-first order model since Cr(VI) will stop being the rate limiting reactant; therefore, the rate law and intrinsic rates were only obtained for experiments with 170 μM Cr(VI) since they follow a pseudo-first order model. Further work will be needed to completely elucidate the kinetics of Cr(VI) reduction as a function of increasing Cr(VI) concentration, with a special focus on experiments at higher initial Cr(VI) concentrations. Furthermore, while the reduction kinetics model proposed here (Eqn. 12) is independent of both the pH and initial Cr(VI) concentration, it still depends on the sorbent concentration. As the reduction rate of Cr(VI) is expected to change with changing WSBC loading, further experiments as a function of biochar concentration could be conducted to further generalize the rate law given in Eqn. 12.

Overall, the rates obtained in the pH experiments and the order of reaction from both the pH and Cr(VI) dependent studies provided us with a rate law able to predict the reduction and evolution of Cr(VI) at pH values less than 3, which are consistent with industrial wastewater streams that contain Cr.

*3.2.3 Total Cr, Cr(III) and Cr(VI) evolution in kinetics experiments*

Aliquot sampling from the adsorption experiments allowed for the measurement of Cr(VI) by the DPC method, but also of the determination of the Total Cr and Cr(III) concentrations in solution via ICP-MS. Since there are no protocols to directly determine the concentration of Cr(III), the following equation was utilized:

$$\mathrm{Cr_{total}} = \mathrm{Cr(VI)} + \mathrm{Cr(III)} \quad (13)$$

where Cr(III) was obtained by the difference between the total input Cr concentration, and the Cr(VI) left in solution at a given point in a reduction experiment. Multiple studies have utilized this approach as one of the first lines of evidence of Cr(VI) reduction via production of Cr(III) (Dong *et al.*, 2011; Park *et al*., 2008a). This part of the study focused only on quantifying changes in solution Cr concentration and valence; the mobile Cr is only to be accounted in solution as the Cr(VI) and Cr(III) removed from solution by WSBC was removed from the system. The focus here was on the pH series experiments, since pH effects are key in determining the Cr(VI) removal and Cr(III) generation efficiency of WSBC. The results of plotting the aqueous concentrations of various Cr pools (170 μM) vs. time (h) is shown for pH 2, 2.5, and 3 in Fig. 12.

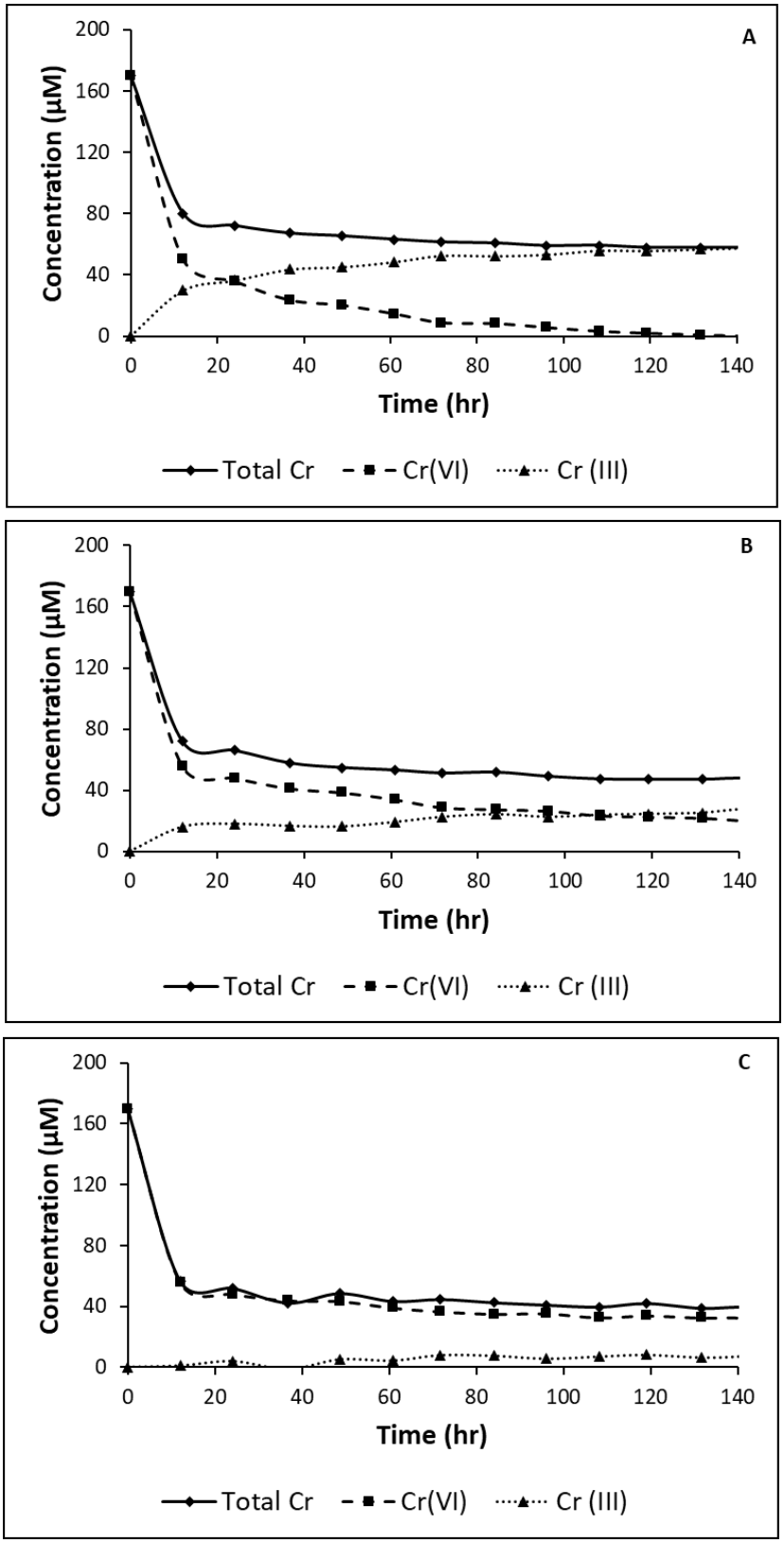


***Figure 12.*** *Evolution of Total Cr, Cr(III) and Cr(VI) over 140 hours at (A) pH 2, (B) pH 2.5, and (C) pH 3*

The evolution of total Cr, Cr(VI) and Cr(III) differs considerably as a function of pH (Fig. 12). A rapid decrease in total Cr and Cr(VI) was observed during the first 12 hours. As previously mentioned, the decrease in Cr(VI) concentration was rapid during the first two hours in the adsorption experiments. Cr(III), as anticipated from the reduction kinetics, was more gradually produced, in contrast to the rapid removal of Cr(VI) and total Cr. One of the greatest differences between the pH series experiments was that complete removal of Cr(VI) from the system was only achieved at pH 2 after 140 hours. At pH 2, all the initial Cr(VI) added to the system has been reduced to Cr(III) after 140 hours; some of the Cr(III) is left in solution, while some is immobilized within and on the surface of WSBC. Increasing pH from pH 2 to 3 resulted in an increase in residual Cr(VI) in solution, as well as a decrease in Cr(III) produced. However, at elevated pH, the adsorption of cationic Cr(III) to the less-protonated (i.e., more negative) surface of WSBC was also more likely to have occurred.

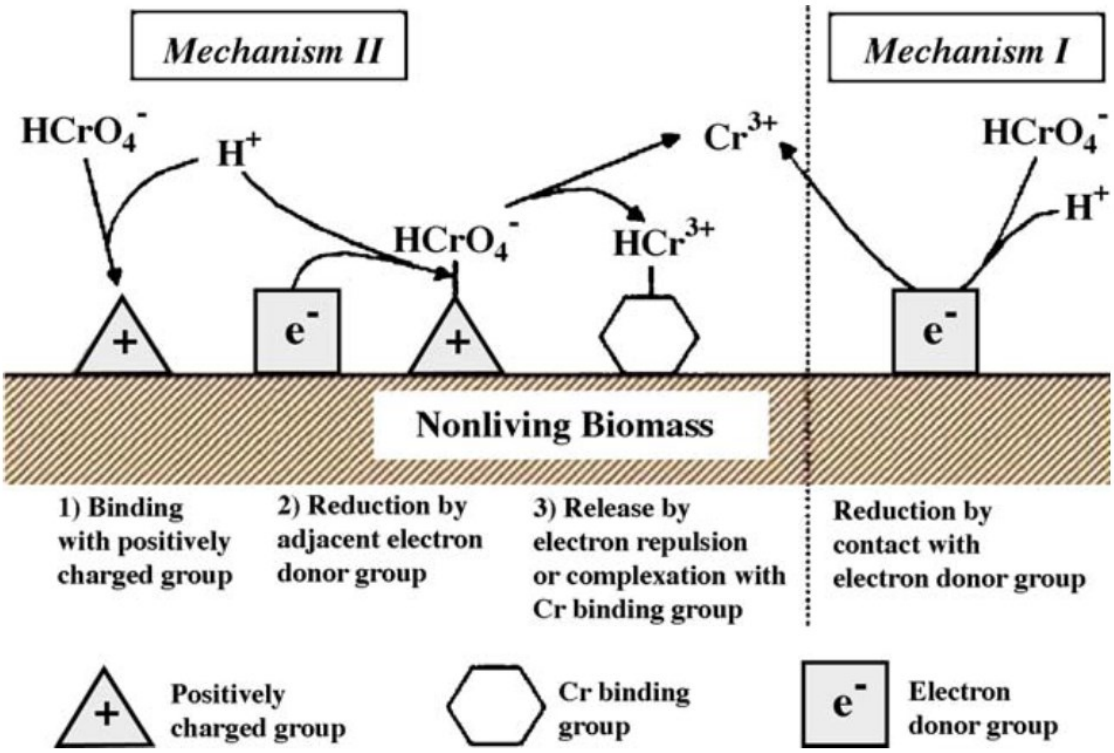


***Figure 13.*** *Reduction mechanisms of Cr(VI) by biomass. Mechanism I describes the direct Cr(VI) reduction by biomass, while Mechanism II describes the indirect Cr(VI) reduction by biomass (adopted from Park et al., 2006)*

The evolution of Cr(III) and residual concentrations of total Cr and Cr(VI) in solution are related to the mechanism of Cr(VI) removal by biomaterials. Previous studies have indicated that the removal of Cr(VI) by biosorbents, especially electron donors, is via adsorption-coupled-reduction (Park *et al.*, 2007; 2006), which can follow two mechanisms: direct and indirect adsorption-coupled-reduction of Cr(VI) (Fig. 13.). The direct reduction of Cr(VI) involves contact with the donor group or functional groups capable of reducing Cr(VI), with the resulting Cr(III) remaining in solution or forming complex with the Cr-binding functional groups of WSBC (Fig. 13, Mechanism I). Further explanation of the Cr-binding functional groups will be given in the XAS and FTIR results sections below. As Park *et al.* (2006) indicate, indirect Cr(VI) reduction requires three steps: (1) the binding or adsorption of the anionic Cr(VI) to the protonated surface

of the biomass, WSBC in this case, (2) Cr(VI) reduction to Cr(III) via the electron transfer from adjacent electron-rich donor groups, and (3) the release of Cr(III) cations via electronic repulsion with the protonated WSBC surface, or the complexation of the Cr(III) to Cr-binding groups of WSBC (Park *et al.*, 2008b; Park *et al.*, 2006).

Reduction of Cr(VI) to Cr(III) requires an electron donor, and the consumption of protons from solution. At pH 2, all of the Cr(VI) was removed from solution by the transformation to Cr(III); however, the high degree of protonation of WSBC surface functional groups at pH 2 would result in the electrostatic repulsion of more of the resulting cationic Cr(III) from the surface of the biochar than at higher pH. Thus, although all of the Cr in solution was reduced after 140 h, the total Cr concentration in solution remains relatively high. Furthermore, Cr(III) exhibits a tendency to form complexes with naturally occurring materials, such as amino, fluvic, humic and other acids, and will remain in solution even above pH 7 where Cr(III) would be predicted to precipitate to $Cr(OH)_3$ (Kotasâ & Stasicka, 2000). Although less reduction will occur at pH 2.5 and 3, considerable Cr(VI) was still removed from solution via adsorption. The lesser amount of Cr(III) measured in solution at pH 2.5 and 3 reduction experiments than in the pH 2 experiments was likely due to the decrease in biochar surface protonation, promoting greater Cr(III)-WSBC binding as the pH increased above 2. Nonetheless, some Cr(III) was still measured in solution at pH 3, likely via the repulsion of Cr(III) from the protonated WSBC surface at low pH and the possible formation of soluble organometallic Cr(III) species. This was the reason why subsequent reduction of Cr(VI) to Cr(III) in acidic conditions requires the addition of lime to hydrolyze and precipitate the mobile Cr(III) into $Cr(OH)_3$, preventing the migration and potential reoxidation of Cr(III) to Cr(VI). Thus, a subsequent base addition may have to be employed if WSBC were utilized to remove Cr(VI) in systems with pH less than 3.

*3.2.4 Electron transfer in chromium-biochar redox reactions*

Biomaterials have a known quantity of electrons or electron charge density that is expected to decrease as the number of electrons consumed via electron transfer increases over time. For instance, BC has the ability to transport π-electrons across the aromatic benzene rings composing its carbonaceous structure. Transformation of Cr(VI) to Cr(III) requires the transfer of 3 electrons, but in going from Cr(VI) to Cr(III), several intermediate Cr(V) and Cr(IV) species are formed (Eqns. 5 – 8).

| Time (hr) | Time (d) | µmol e- $m^{-2}$ | µmol e- $m^{-2}$ $d^{-1}$ | Change in e- transfer |
|---|---|---|---|---|
| 96.900 | 4.038 | 34.804 | 8.620 | 83.46% |
| 963.000 | 40.125 | 57.210 | 1.426 | |
| ***Initial conditions: pH 2, 0.1 g L*** $^{-1}$ WSBC, and initial Cr(VI) of 700 µM | | | | |
| 118.700 | 4.946 | 48.586 | 9.824 | 80.50% |
| 936.083 | 39.003 | 74.719 | 1.916 | |
| ***Initial conditions: pH 2, 0.1 g L*** $^{-1}$ WSBC, and initial Cr(VI) of 1300 µM | | | | |

***Table 8.*** *Electron transfer capability of WSBC at elevated Cr(VI) concentrations (700 and 1300 µM at 107.8 ± 15.4 hours and 949.5 ± 19.0 at pH 2*

At pH 2, the electron density was determined by considering the WSBC loading, initial Cr(VI) concentration and the changes in Cr(VI) concentration over time, assuming all Cr(VI) removal occurred via the adsorption-coupled-reduction outlined above. Longer term electron transfer densities were calculated for the higher Cr(VI) concentrations experiments, by selecting two time periods each from each of the 700 and 1300 µM Cr(VI) kinetics experiments series (Table 8). Since in the 700 and 1300 µM Cr(VI) experiments the entire pool of Cr(VI) was not reduced, Cr was not the rate-limiting species. Thus, those experiments were selected to give an idea of the

total labile electron transfer capacities of WSBC. For both the 700 and 1300 μM initial Cr(VI) concentrations, the number of electrons transferred were almost an order of magnitude greater for samples taken at approximately 4 days than after approximately 40 days. Full reduction of Cr(VI) at the lowest concentration, 170 μM, at pH 2 was attained after approximately 4.5 days; thus, these experiments were not considered for this analysis. Two different approaches were taken: (1) calculating the overall transfer of electrons per square meter of WSBC surface area, and (2) determining the observed rate of transfer of electrons per square meter per day of experimentation. Utilizing the SA of WSBC (Table 2), the transfer capacity per square meter of WSBC was obtained. As Cr(VI) reduction proceeded, the pool of labile electrons decreased, and the average distance an electron had to travel to reduce Cr(VI) at the WSBC surface increased. Secondly, and more important was to determine the transfer capacity of WSBC per unit of time, which is indicative of the capacity of WSBC to transfer electrons over time, considering the ongoing loss of electrons to concurrent Cr(VI) reduction. The instantaneous electron transfer rate of WSBC with 700 μM Cr(VI) decreased from 8.620 to 1.426 e- $m^{-2}$ $d^{-1}$ from day 4 to day 40, while in the experiments using 1300 Cr(VI), the rate of electron transfer decreased from 9.824 to 1.916 e-$m^{-2}$ $d^{-1}$ (Table 8). These represent 83.46% and 80.50% decreases in electron transfer for the 700 Cr(VI) and 1300 Cr(VI) experiments, respectively. At elevated Cr(VI) concentrations (≥ 700 μM Cr(VI)), a relatively constant transfer of electrons was observed, independent of Cr(VI) concentration, which was expected to slowly decrease over time. Although the reduction capabilities of WSBC were never completely exhausted, the decrease in the electron transfer rate was consistent with the use of electrons for the transformation of Cr(VI) to Cr(III). Unlike pH (proton availability), which was buffered by the acidity of the surrounding aqueous solution, the quantity of electrons per SA

of BC will decrease over time until the electron transfer capacity of BC is exhausted and WSBC can no longer be the catalyst for the Cr(VI)/Cr(III) redox process.

*3.3. Surface functionality of WSBC and the binding environment of Cr(VI) and Cr(III)*

Biomass contains a mixture of organic and inorganic components that are capable of providing suitable reactive sites for both organic and inorganic species to be adsorbed or chelated (Nanda *et al.*, 2013). The most important organic constituents of plant biomass are hemicellulose, cellulose and lignin. The ratio between hemicellulose, cellulose and lignin is unique to every plant, with major differences in ratios found between woody and grassy biomass. Lignocellulosic biomass, such as wheat straw, often contains 10 – 25% lignin, 35 – 55% cellulose, and 20 – 40% hemicellulose (Nanda *et al.*, 2013). Lignin is a key constituent of plants since it acts as a binding agent between cellulose and other materials (Flogeac *et al.*, 2003). Cellulose is also one of the most abundant constituents of plant biomass and the most abundant biopolymer on the Earth, which is known to greatly contribute to the structural integrity of plant cell walls (Wang & Lee, 2011). As well as cellulose, hemicellulose contributes to the strengthening of the plant cell walls. Not only are these materials abundant in lignocellulosic biomass, but there have been previous studies showing that reduction of Cr(VI) to Cr(III) was attained using these components alone. For example, work by Wang & Lee (2011) elucidated the Cr(VI) reduction capabilities of cellulose at pH 2. It was shown that the oxidation of lignin from lignocellulosic material occurs concurrently to Cr(VI) reduction (Dupont & Guillon, 2003), and also that lignin moieties are capable of forming inner-sphere complexes with Cr(III) (Wu *et al.*, 2008). There are multiple constituents in biomass capable of binding Cr(VI) and aiding in its reduction.

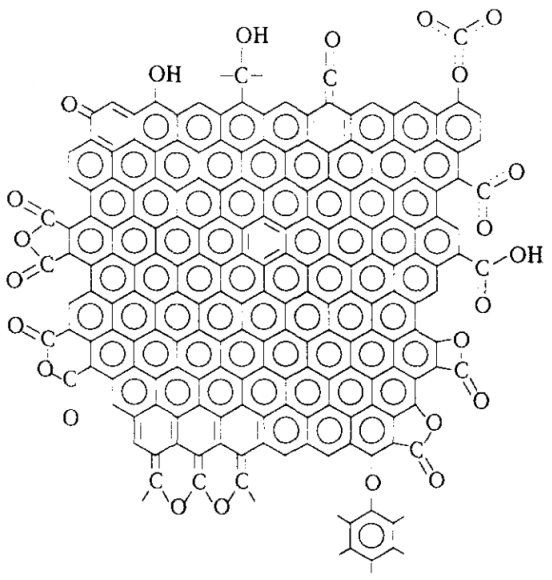

***Figure 14.*** *Schematic representation of surface functional groups in carbon* (modified from Fanning & Vannice, 1993)

The ability of biomass, especially lignocellulosic biomass, to form complexes with Cr is attributed in part to the existence of surface functional groups. Spectrometric studies of cellulose, hemicellulose, and lignin have indicated that such components are composed of alkene, aldehyde, esters, aromatics, ketones, alcohols, and different O-containing functional groups (Flogeac *et al.*, 2003; Yang, 2007). However, the surface functionality of lignocellulosic material is expected to change once biomass undergoes thermal conversion via pyrolysis. The pyrolysis parameters will have a considerable influence on the thermal decomposition of the intrinsic components of the initial lignocellulosic, resulting in an overall decrease of O- and H-containing functional groups and the increase in aromatic carbon-carbon double bonds (Kim *et al.*, 2011). Indeed, biomass undergoing pyrolysis experiences a decrease in H/C and O/C molar ratios, related to decarboxylation, decarbonylation, dehydrogenation, demethoxylation and demethylation processes (Kim *et al.*, 2011; Kloss *et al.*, 2012). Nonetheless, the pyrolytic decomposition of biomass components can also produce other functional groups, such as the formation of carboxylic

and carbonylic groups via decomposition of carbohydrates (Kloss *et al.*, 2012). It has been reported that surface functional groups, in particular O-containing functional groups, will tend to be attached to the periphery or at defect sites, such as vacancies in the spheroidal ordering of the graphitic layers encompassing the very disordered nucleus of biochar (Fig. 14; Fanning & Vannice, 1993), and the contribution of those functional groups may aid in the sorption and reduction of redox sensitive heavy metals.

To provide a deeper understanding of the ability of WSBC to transform Cr(VI) to Cr(III) via adsorption-coupled-reduction, a spectroscopic analysis of Cr-laden WSBC was conducted. FTIR was applied to investigate the changes in functional groups in WSBC as the adsorption-coupled reduction of Cr(VI) to Cr(III) and then Cr(III) sorption took place over time. X-ray absorption spectroscopy (XAS) was also utilized to elucidate both the valence state of Cr and the local coordination (binding) environment of Cr bound to WSBC. XAS is based on the absorption of high-energy monochromatic X-rays by a given element with their characteristic absorption edge region (Park *et al*., 2008b). Two regions of the resulting XAS spectra are normally utilized: the X-ray Absorption Near Edge Structure (XANES) region, and the X-ray Absorption Fine Structure (EXAFS) region. XANES data were used to determine the average oxidation states of Cr in Cr-laden WSBC. EXAFS is used for the identification of the coordination environment of metal ions in environmental samples, i.e., the types of functional groups to which Cr(III) was bound in WSBC. Combined, the spectral results from FTIR, XANES, and EXAFS provide complementary information about the oxidation state of Cr and the binding of Cr(III) to WSBC functional groups.

*3.3.1. Oxidation state and bonding of Cr to WSBC*

The local molecular coordination of Cr(III) bound to WSBC functional groups was determined using Cr *K*-edge XANES. Several reference materials were utilized to differentiate both the oxidation state of Cr and its coordination environment. Specifically, potassium dichromate salt was analyzed to collect a reference spectrum representative of the Cr(VI) oxidation state. Three different reference materials were used to represent the functional groups capable of Cr(III) complexation. Cr(III) hydroxide was utilized to represent the Cr(III) – OH complexes; Cr(III) acetate represented the complexation between Cr(III) and carboxyl groups; and Cr(III) acetylacetonate was utilized to represent the Cr(III) – carbonyl complexes (Shen *et al.*, 2010; Shen *et al.*, 2012). The Cr-laden WSBC samples analyzed came from experiments conducted at pH 2, 2.5 and 3.7, with an initial Cr(VI) concentration of 170 μM to elucidate the change in Cr binding environment as a function of pH. The resulting XANES spectra of the reference materials and the Cr-laden WSBC at pH 2, 2.5 and 3.7 are shown in Fig. 15. The XANES spectrum of potassium dichromate shows the characteristic and prominent pre-edge peak of Cr(VI) located at approximately 5990 eV, which is caused by the transition of 1s to 3d electrons to an unoccupied antibonding tetrahedral orbital (Shen *et al.*, 2010). According to Flogeac *at al.*, (2003), the empty d-orbital, $3d_0$, increases the transition probability from 1s to 3d, which enhances the pre-edge intensity. $Cr^{3+}O_6$ compounds have an octahedral geometry; thus, it is impossible for such compounds to have a center of symmetry, as opposed to centrosymmetric tetrahedral $Cr^{6+}O_4$ compounds, due to the mixing of Cr(3d) and O(2p).

Although Cr(III) compounds also have a pre-edge peak at approximately 5985 eV from the 1s to 3d excitation, it is not nearly as prominent as the Cr(VI) pre-edge peak. The lack of this pre-edge feature from any other reference material was the main indicator that Cr was in its reduced

state. Cr(III) acetate, Cr(III) hydroxide and Cr(III) acetylacetonate all show the small peak at approximately 5985 eV, which was not present in the Cr(VI) XANES spectra and can serve as a second line of evidence for Cr(VI) reduction. Nonetheless, apart from the small peak at approximately 5985 eV (Fig. 15), all of the Cr(III) reference compounds had very different post-edge adsorption patterns that distinguish them from each other, and allow them to be used to distinguish different binding environments of Cr(III) to WSBC functional groups.

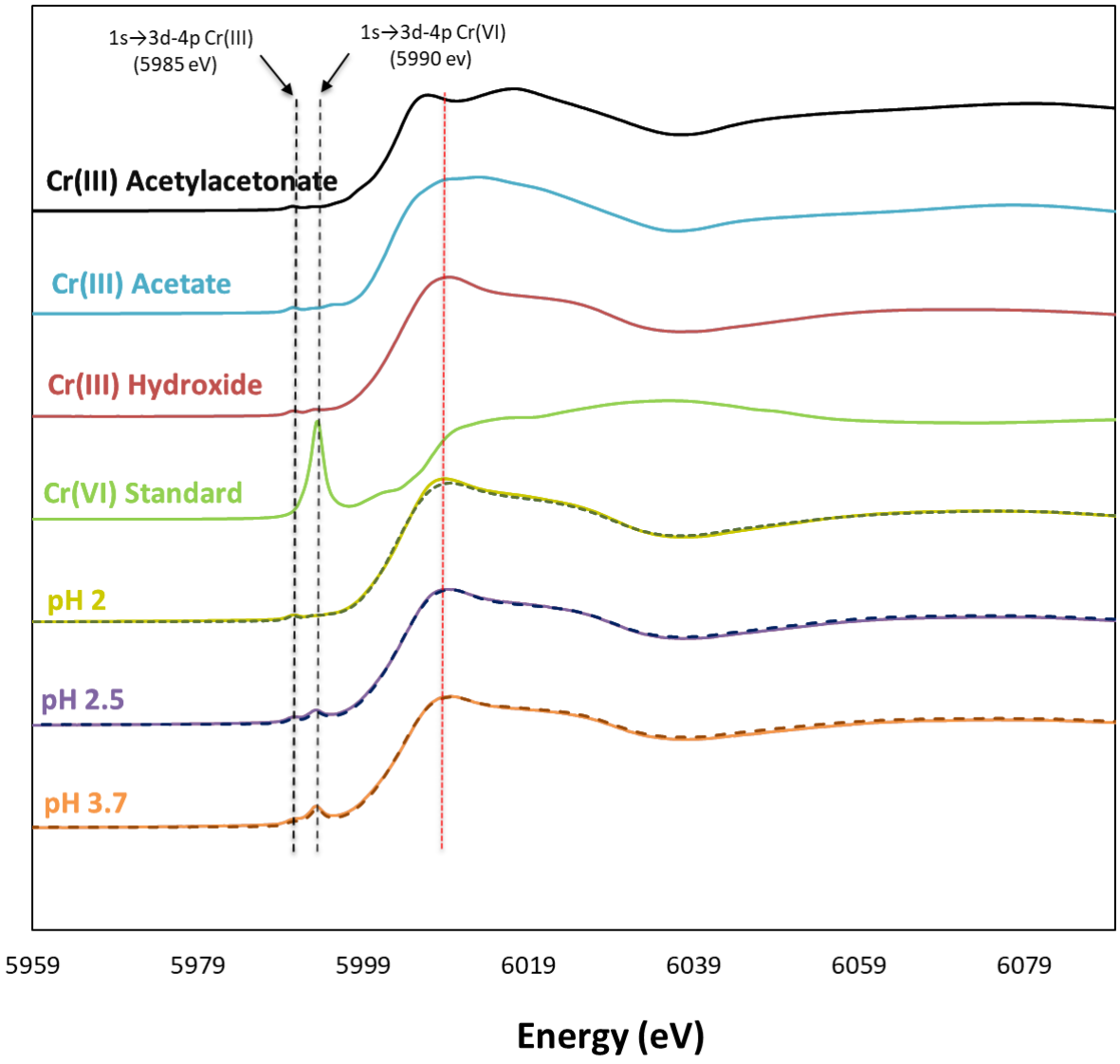


***Figure 15.*** *Cr K-edge XANES for reference materials: Cr(III) acetylacetonate, Cr(III) acetate, Cr(III) hydroxide, and potassium dichromate Cr(VI). As well as the Cr-laden WSBC solids at: pH 2, pH 2.5, and pH 3.7. Correlation between the reference material and the Cr-laden WSBC samples is portrayed by a reference line (dotted red line)*

Analysis of the XANES spectra of Cr-laden WSBC at pH 2, 2.5 and 3.7 indicate that distinct pre-edge Cr(VI) feature at 5990 eV is not as prominent as the one observed from the Cr(VI) reference material. In addition, the small pre-edge peak at 5985 eV, shared by all Cr(III) reference standards, was also present. The decrease in the Cr(VI) pre-edge peak of combined with the

appearance of the Cr(III) pre-edge peak is evidence of the reduction of Cr(VI) to Cr(III) by WSBC. The relative size of the Cr(VI) also indicate the proportion of this species in the samples, and is evident that the Cr(VI) pre-edge peak increased with increasing pH, which describes the lower redox potential of WSBC with lower concentration of protons in solution as described in previous sections. The XANES spectra indicate that most of the Cr bound to WSBC is in trivalent form, providing direct evidence that Cr(VI) reacted with WSBC to form Cr(III)-WSBC complexes, as was hypothesized from the wet chemical data.

| Sample | Proportion of the reference material in sample (%) | | | | R factor ( x $10^{-4}$) |
|---|---|---|---|---|---|
| | $K_2Cr_2O_7$[a] | $Cr(OH)_3$ | Cr(III)AC[b] | Cr(III)AA[c] | |
| Cr-WSBC pH 2 | Nil | 74.00% | 26.00% | Nil | 17.96 |
| Cr-WSBC pH 2.5 | 6.00% | 86.10% | Nil | 7.90% | 5.99 |
| Cr-WSBC pH 3.7 | 12.70% | 77.40% | Nil | 9.90% | 5.40 |

[a] $K_2Cr_2O_7$ represents Cr(VI)

[b] Cr(III)AC represents Cr(III) acetate

[c] Cr(III)AA represents Cr(III) acetylacetonate

***Table 9.*** *Linear combination fitting (LCF) results for the resulting XANES spectra of Cr-laden WSBC at pH 2, 2.5, and 3.7*

Using the three Cr(III) standards and the Cr(VI) standard, LCFs were performed on the XANES spectral results to account for (1) the average valence state of Cr bound to the WSBC sample in question, and (2) the distinct Cr(III)-containing complexes. The LCF results are represented by the dashed lines on the pH 2, pH 2.5 and pH 3.7 sample spectra (Fig. 15) and indicate the mathematical correlation between the Cr-laden WSBC samples and the Cr reference materials. Table 9 shows the LCF results for Cr-laden WSBC at different pH. The fraction of bound Cr(VI) decreased as a function of pH, from 13% to below the detection limit as the pH went from pH 3.7 to 2, respectively. The XANES results of Cr-laden WSBC at pH 2, were consistent with the full reduction of Cr(VI) observed at pH 2 obtained from the chemical analysis (Fig. 5A).

As discussed above, pH 2 was the best system to achieve full Cr(VI) removal with WSBC at the 170 µM Cr(VI) condition.

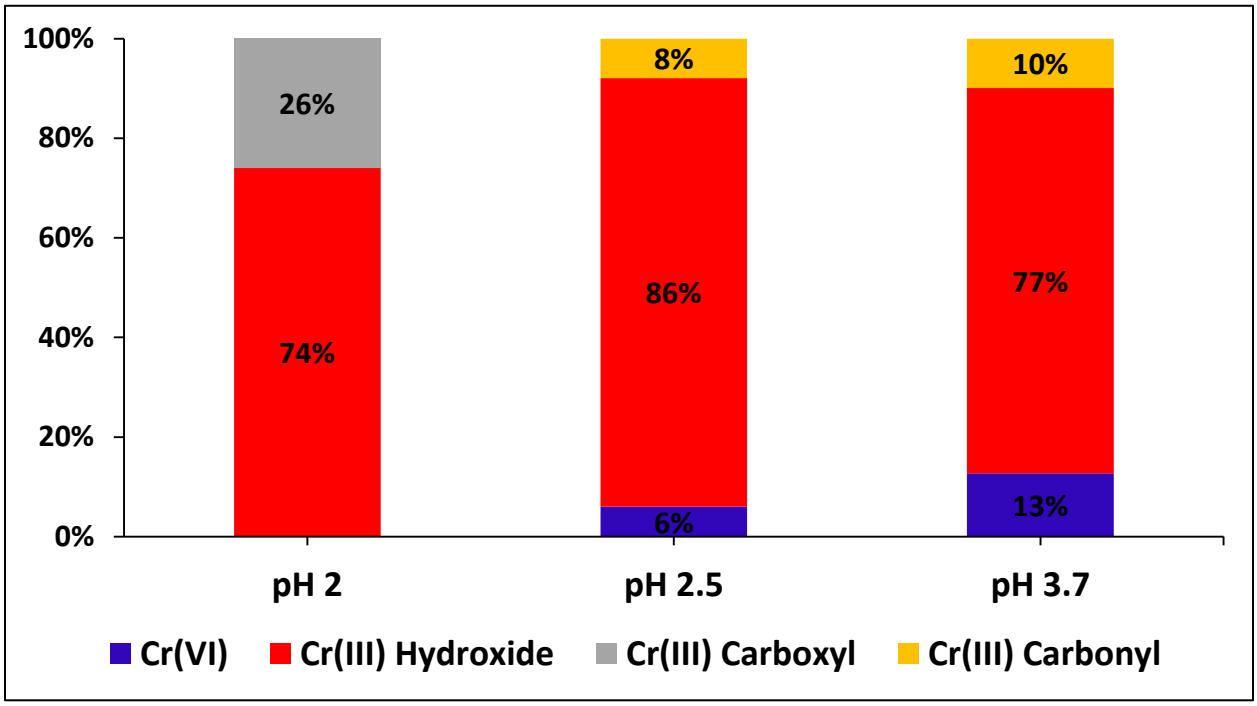


***Figure 16.*** *Schematic representation of LCF results on Cr complexes evolution at a function of pH*

The contributions of various surface functional groups to the complexation of Cr(III) changes considerably as a function of pH amongst the hydroxylic, carboxylic and carbonylic moieties modeled in the LCF results (Fig. 16). The reduction of Cr(VI) causes the concurrent oxidation of biochar carbon, including surface moieties. According to Park *et al.* (2007), the oxidation of lignin moieties for Cr(VI) reduction leads to the formation of hydroxyl and carboxyl groups. Wang *et al.* (2009) found that the reduction of Cr(VI) with wheat straw derived black carbon led to the formation of hydroxylic and carboxylic groups. The reduction of Cr(VI) will result in the oxidation of WSBC, generating greater quantities of hydroxyl moieties capable of forming complexes with Cr(III). Hydroxyl moeities induce the formation of Cr(III)-hydroxyl

surface complexes or polynuclear Cr species, with the possibility of forming Cr(III)-hydroxides precipitates (Shen *et al.*, 2012). The fraction of Cr(III)-OH complexes was consistently high, between 74% to 86% of the total surface-bound Cr pool. Cr(III)-OH displayed an increase in proportion from 77% to 86% as the pH decreased from 3.7 to 2.5, due to the increase in OH- formation caused by the concurrent increase in Cr(VI) reduction and the decrease of bounded Cr(VI) from 13% at pH 3.7 to 6% at pH 2.5. However, Cr(III)-OH displayed a decrease in proportion from 86% to 74% when the pH further decreased to pH 2. The oxidation of phenolics and hydroxyl moieties will lead to the formation of quinones containing carbonyl groups, which would contribute to the 10% proportion of Cr(III) – carbonyl complexes observed at pH 3.7 (Elovitz & Fish, 1995). The overall fraction of Cr(III) – carbonyl complexes decrease from 10% to 6%, and finally to below the detection limit as the pH decreases from 3.7 to 2. As Cr(VI) reduction continues to take in place, further oxidation of carbonyl groups would lead to the formation of carboxylic moieties which are also capable of forming stable complexes with Cr(III) (Choppala *et al*., 2012; Dupont & Guillon, 2003; Elovitz & Fish, 1995; Park *et al*., 2008b; Santos *et al*., 2002; Shen *et al*., 2010; Wang & Lee, 2011). Between pH 2 to 3.2, Arslan & Pehlivan (2007) indicated that carboxyl groups will deprotonate to $COO^-$ which can then bind to the Cr(III) cations, increasing the Cr(III)-carboxyl fraction up to 26% at pH 2. This mechanism of functional group development explains the decrease of Cr(III) – carbonyl and Cr(III) – OH at pH 2, and concurrently an abrupt increase in Cr(III) – carboxylic complexes due to the combined formation of carboxylic groups by the oxidation of hydroxylic, phenolic and carbonylic groups (Table 9, Fig. 16).

*3.3.2. Infrared spectra of Cr-laden WSBC*

To complement the XANES analyses, infrared spectroscopy was used for Cr-laden WSBC from the 12-hour interval time series, at pH 2, and 170 µM of initial Cr(VI). The infrared spectra of Cr-laden WSBC are shown in Fig. 17 for wavenumbers between 600 and 1800 $cm^{-1}$, and Fig. 18 for wavenumbers between 2700 and 3700 $cm^{-1}$.

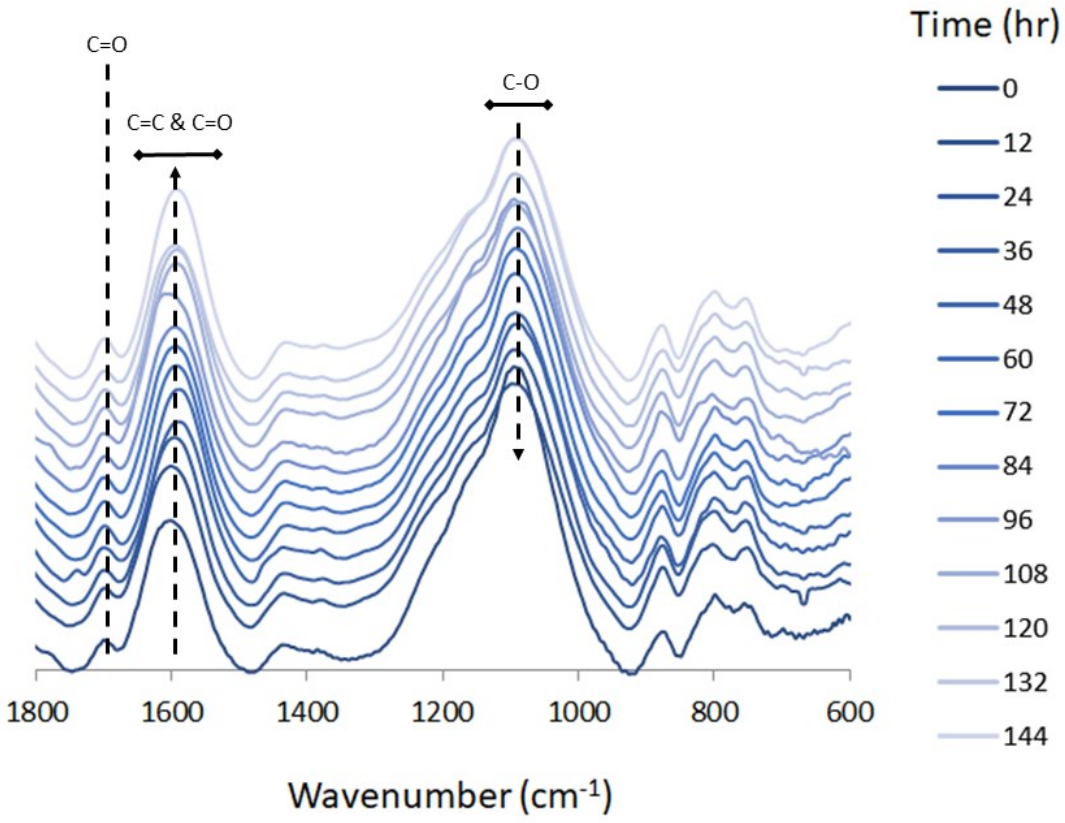


***Figure 17.*** *Infrared spectra of Cr-laden WSBC samples taken at pH 2 every 12 hours, between 600 and 1800 $cm^{-1}$*

The first area of interest is between the 600 and 1800 $cm^{-1}$ wavenumber region that includes distinctive series of patterns for organic compounds, and the double bond region. Over the span of 6 days, there were measurable changes in bands located near the 1600 $cm^{-1}$ and 1100 $cm^{-1}$ regions.

The first change involves the 1600 $cm^{-1}$ region, with an overall increase in intensity and shift to lower wavenumbers after 24 h. Changes in the infrared spectral band near 1600 $cm^{-1}$ can include changes in C=O groups belonging to carboxylic groups and C=C bonds that involve aromatic C=C (Hsu *et al.*, 2009; Hsu *et al.*, 2009b; Zhang *et al.*, 2010). Previous studies have associated the increase near 1600 $cm^{-1}$ to the production of carboxyl functional groups from the consequent oxidation of biochar and other moieties, such as phenols (Elovitz & Fish, 1995; Shen *et al*., 2012). In addition, the shift to lower wavenumber is the result of a carboxyl or carbonyl group complexing with Cr(III); thus, we can assume that not only is the reduction of Cr(VI) to Cr(III) producing carboxylic or carbonyl moieties but that Cr(III) is undergoing complexation with these newly formed surface functional groups. Wang & Lee (2011) reduced Cr(VI) at pH 2 using lignocellulosic material, and their infrared analyses results indicated that the increase in the region between 1640 and 1460 $cm^{-1}$ resulted from the formation of carboxyl groups from the oxidation of C-OH groups concurrent to the reduction of Cr(VI). Up to 26% of the total Cr in our pH 2 experiments was bound to carboxyl groups, as indicated in the XANES LCF results (Fig. 16); this result matches the infrared spectral results that indicate that reduction of Cr(VI) produced greater quantities of carboxylic moieties capable of complexation with trivalent Cr. Production of carbonyl groups due to oxidation of biochar moieties from Cr(VI) redox reactions would promote the subsequent binding of Cr(III) to form Cr(III)-carbonyl complexes, as shown in the XANES LCF results of Cr-laden WSBC at pH 2 and pH 3 (Fig. 16).

The second area of interest encompasses the region between approximately 1300 $cm^{-1}$ and 1000 $cm^{-1}$. In contrast to the increase in intensity shown in the 1600 $cm^{-1}$ region, there was an obvious decrease in spectral intensity once Cr(VI) reacted with WSBC at pH 2. Important functional groups can be found in the range between 1000 $cm^{-1}$ and 1300 $cm^{-1}$, such as the C-O

bond belonging to ester groups, and the C-OH groups belonging to phenolic groups (Fanning & Vannice, 1993). This region was difficult to analyze and the exact functional groups being affected by Cr-WSBC reactions is not entirely clear since there are overlapping peaks belonging to ester and phenolic moieties in this region. However, as indicated by Fanning & Vannice (1992), based on the combined analysis of features in the 3500 $cm^{-1}$ and 1200 $cm^{-1}$ regions, it was determined that evidence of phenols was present in the infrared features of WSBC. The reduction mechanisms of Cr(VI) with alcohol groups have been previously elucidated, and such reactions share similarities with the reduction pathways of Cr(VI) with phenols (Elovitz & Fish, 1995). These previous studies have demonstrated that the reduction of Cr(VI) with phenols involved first the oxidation of phenol groups to produce carbonyl-containing quinone groups (Choppala *et al*., 2012; Elovitz & Fish, 1995; Fanning & Vannice, 1993; Santos *et al*., 2002). An intermediate step was proposed, involving the formation of a chromate ester before the rapid decomposition by an inner-sphere electron transfer, forming quinone groups in the process. The oxidation of phenols during Cr(VI) reduction is a plausible mechanism promoted by WSBC, since phenols exhibit a higher electron density because of the aromatic ring attached to the hydroxyl group. Therefore, components of the biochar, especially phenolic moieties, and the biochar itself were oxidized concurrently to Cr(VI) reduction, yielding carbonyl and carboxyl groups as indicated by the increase in the C=O region between 1700 $cm^{-1}$ and 1500 $cm^{-1}$, and the decrease in bands between 1300 $cm^{-1}$ and 1100 $cm^{-1}$.

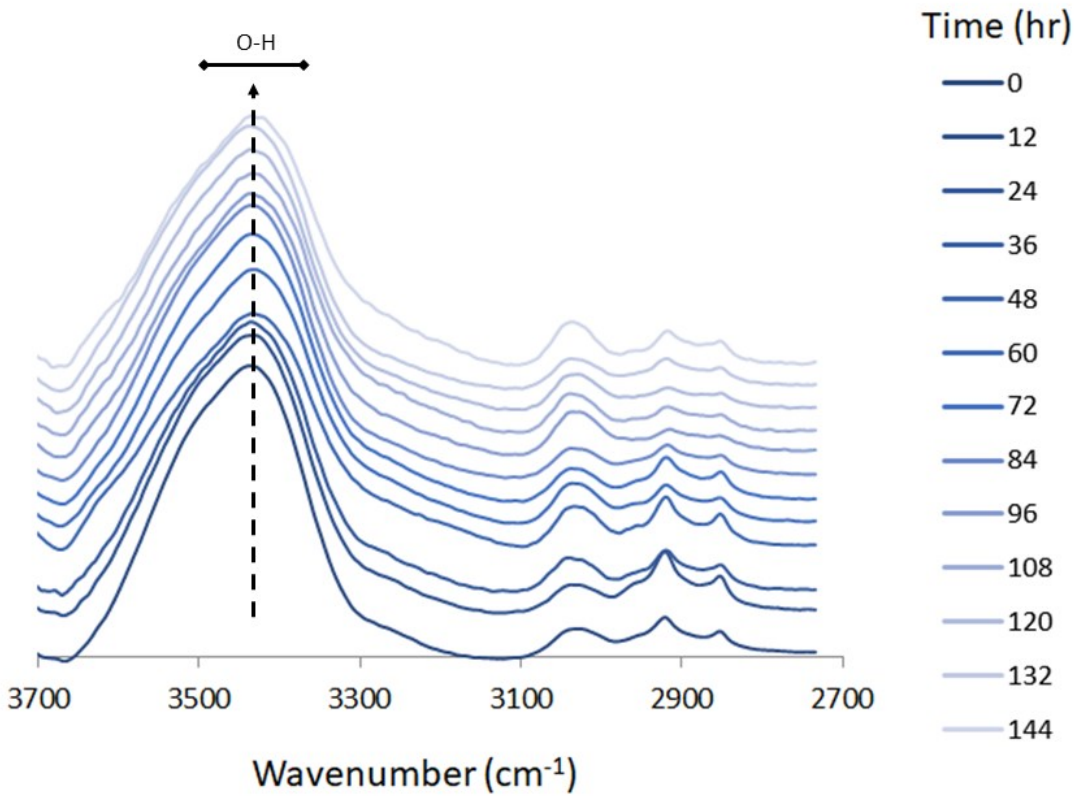


***Figure 18.*** *Infrared spectra of Cr-laden WSBC samples taken at pH 2 every 12 hours, between 2700 and 3700 cm$^{-1}$*

The third area of focus was between the 3700 cm$^{-1}$ and the 2700 cm$^{-1}$ wavenumber range (Fig. 18). This range included the OH bend/stretching of phenols and alcohol groups between 3200 cm$^{-1}$ and 3640 cm$^{-1}$ and the primary amine groups between 3354 cm$^{-1}$ and 3358 cm$^{-1}$ (Tytłak *et al.*, 2015). There was a visible increase in the OH region, while there was no change in the primary amine group region. This indicated that the reduction of Cr(VI) resulted in the production of hydroxyl moieties over time. That the production of hydroxyl moieties capable of forming complexes with Cr(III) occurred was further supported by the previously discussed XANES results. Hydroxyl groups, apart from the phenolic moieties, could have also aided in the reduction of Cr(VI) (Choppala *et al*., 2012).. Thus, it was deduced that reduction of Cr(VI) causes the

oxidation of WSBC, which leads to the formation of OH groups at the surface of WSBC, along the formation of additional carbonyl and carboxyl groups capable of forming complexes with Cr(III). The OH contribution was not only supported from the strong evidence shown in the XANES fitting results, but also from the fact that hydroxyl and carboxyl groups are important in the removal of heavy metals (Khare *et al.*, 2013; Mohan *et al.*, 2014; Park *et al.*, 2011).

*3.4 Binding environment of Cr to WSBC*

The EXAFS part of the XAS spectra were analysed for Cr-laden WSBC samples at pH 2, 2.5 and 3.7, to determine the local coordination environment of Cr in WSBC. The model structures of all reference materials, including the structures of Cr(III) hydroxides, Cr(III) carboxyl, Cr(III) carbonyl and Cr(VI), are portrayed in Fig. 19. Fig. 20A shows the fitted Fourier Transform (FT) derived from the EXAFS spectra of each sample. An optimized hydroxide – acetate model was obtained by combining the Cr-hydroxide and Cr-acetate models derived from the measured XANES and EXAFS spectra of the Cr(III) hydroxide and Cr(III) acetate reference materials. These spectra were further used in R space curve fitting (Fig. 20B). The Cr-laden WSBC sample spectra was fit between $k$ = 3 to 11 $Å^{-1}$ (Fig. 20A) using the theoretical parameters from the hydroxide – acetate shells in the range of R = 1 to 5 Å. The results of the shell-by-shell fitting, along with the optimized hydroxide – acetate model, are given in Table 10.

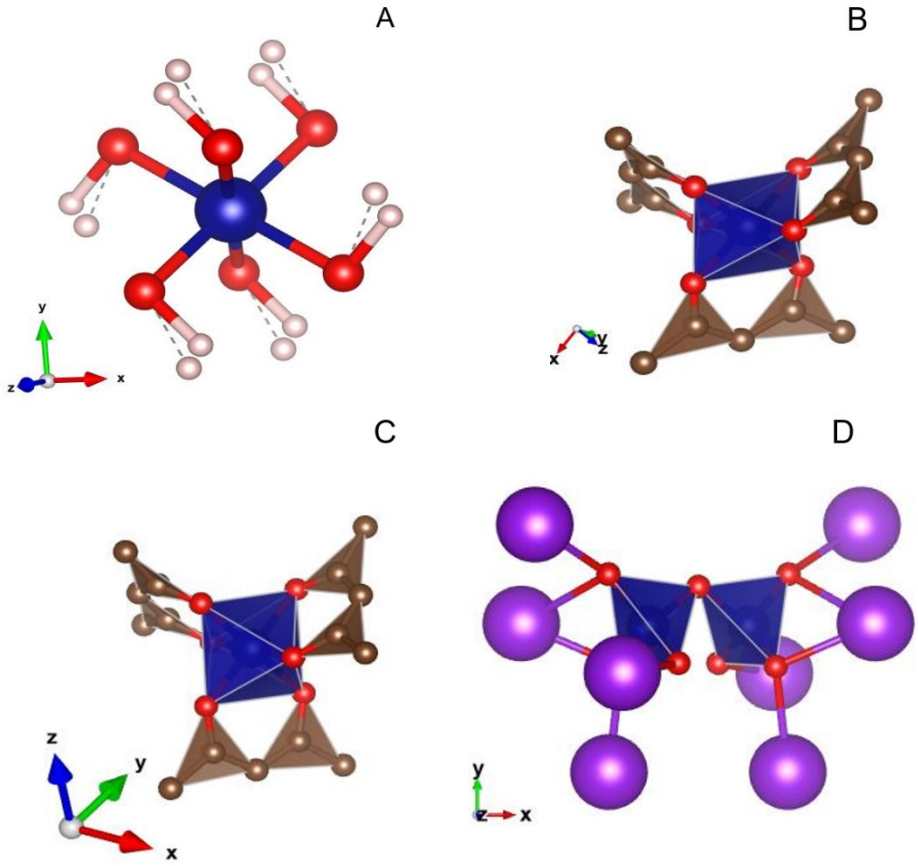


***Figure 19.*** *Structural models of: Cr(III) hydroxide as CrOOH (A), Cr(III) – carboxyl as Cr(III)-acetate, Cr(III) – carbonyl as Cr(III) acetylacetonate, and Cr(VI) as* $K_2Cr_2O_7$

The first shell in the fitted FT was determined to be a Cr–O coordination. The Cr–O R distance was calculated to be 2 Å with a CN of 6, consistent with the octahedral structure of Cr(III) from previous studies (Gardea-Torresdey *et al.*, 2000; Lindqvist-Reis *et al.*, 1998; Rao *et al.*, 2002). On the contrary, Cr(VI) is tetrahedrally coordinated with a Cr-O distance of less than 1.9, often reported to be approximately 1.6 Å (Hsu *et al.*, 2009; Parsons *et al.*, 2002). The lack of tetrahedral Cr-O shells, especially at pH 2, provided further evidence of the near-complete reduction of Cr(VI) to Cr(III) by WSBC, complementing the kinetics and XANES LCF results. In

this case, the Cr-O shell indicates the coordination of Cr with hydroxyl functional groups *et al*., 2012), as well as carboxylates functional groups (Dupont & Guillon, 2003; Park, *et al*., 2008).

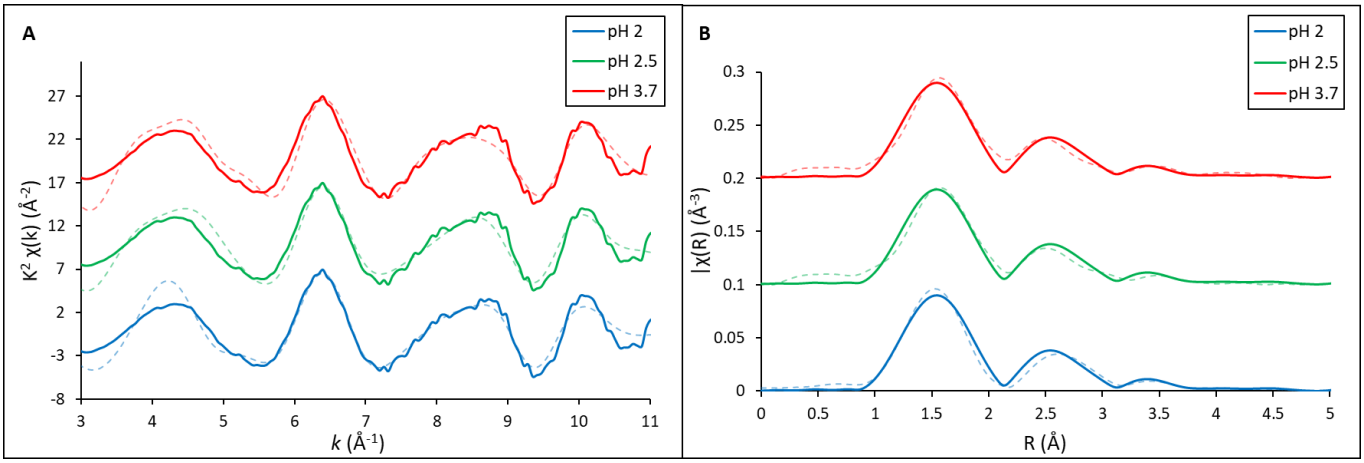


***Figure 20.*** *EXAFS results, including: k-k2–weighted spectra (A), and Fourier transformed EXAFS (B) of Cr-laden WSBC samples at pH 2, 2.5 and 3.7*

The second peak observed in the Radial Structure Function (RSF) was modelled using a Cr–Cr shell; however, the data was also consistent with a Cr-C bond model. The detection of a Cr–Cr shell would provide evidence for the precipitation of Cr(III) and Cr(III)-bearing solids at the surface of WSBC, following the reduction of Cr(VI) (Hsu *et al.*, 2009). Previous EXAFS of Cr(III) hydroxides have reported an atomic distance of 2.98 Å for the Cr-Cr shell (Fendorf *et al.*, 1994; Fendorf, 1995; Roussel *et al.*, 2001). However, there is considerable variation in the coordination numbers attributed to α–CrOOH and γ–CrOOH structures (Ohta *et al.*, 2012). α–CrOOH corresponds to a layered Cr(III) hydroxide structure, with a CN of 6, while γ–CrOOH is related to the amorphous Cr(III) hydroxide structure, with a CN of 1.5 (Christensen, 1976; Ohta *et al.*, 2012). Based on the current RSF results of Cr-laden WSBC, CN were between 2.5 to 2, consistent with an amorphous Cr(III) hydroxide precipitate phase following Cr(VI) reduction. The CN of Cr-Cr shells of Cr-laden WSBC agreed with the results obtained from Fendorf (1994), who

simulated Cr(III) hydroxides nucleating at the surface of $SiO_2$ invoking a γ–CrOOH structure, with a CN between 2.3 – 2.9. The low CN of Cr-Cr could also result from XAS analyses themselves, since it tends to describe the bulk state of an element in a sample, and would average the combination of Cr(III) hydroxides precipitates at the surface with other Cr(III) that is bound to WSBC via surface complexation (Hsu *et al.*, 2009). Although precipitation of Cr is expected at higher pH since the hydrolysis of Cr(III) increases rapidly with increases in pH, the precipitation of Cr(III) hydroxide at WSBC surface cannot be ruled out. The atomic distance of approximately 3 Å with a CN of ~6 matches the Cr-C RSF from Cr(III) acetylacetonate (Ohta *et al.*, 2012). Although not a true carboxyl group, but rather a ketone group, such a match could indicate the presence of Cr(III)-carboxyl and -carbonyl shells. However, the low scattering capacity of C, as a result from the decreasing backscattering of C as wavenumber (*k*) increases, increased the uncertainty of the fitting of the Cr-C shell path (Ohta *et al.*, 2012).

| Path | pH2.0 | | | pH2.5 | | | pH3.7 | | |
|---|---|---|---|---|---|---|---|---|---|
| | CN | R | DW | CN | R | DW | CN | R | DW |
| Cr-O | 6.0 | 2.0 | 0.0069 | 6.0 | 2.0 | 0.0054 | 6.0 | 2.0 | 0.0084 |
| Cr-Cr | 2.5 | 3.0 | 0.0084 | 2.0 | 3.0 | 0.0084 | 1.9 | 3.0 | 0.0084 |
| Cr-C1 | 6.0 | 3.1 | 0.0093 | 6.0 | 3.0 | 0.0093 | 5.7 | 3.0 | 0.0093 |
| Cr-C2 | 5.8 | 3.3 | 0.0084 | 7.7 | 3.2 | 0.0084 | 3.8 | 3.3 | 0.0084 |
| Cr-C3 | 7.6 | 4.1 | 0.0084 | 3.9 | 4.0 | 0.0084 | 4.0 | 4.0 | 0.0084 |
| Cr-C4 | 3.6 | 4.3 | 0.0100 | 0.4 | 4.8 | 0.0100 | 3.2 | 4.6 | 0.0100 |

***Table 10.*** *EXAFS curve-fitting summary for Cr-laden WSBC at pH 2, 2.5 and 3.7, along with the optimized hydroxide – acetate model including coordination numbers (CN), radial distances (R), and the Debye–Waller factor (DW)*

EXAFS, along with IR and XANES results, indicate that Cr-laden WSBC contains Cr(III) hydroxide precipitates along with Cr(III)-carboxyl complexes. Greater proportions of precipitates are expected to be formed as the pH is increased; however, there is convincing evidence for the complexation of Cr(III) with carboxylates, carbonyl-containing groups and hydroxyl groups, with some Cr(III) hydroxide precipitates forming following reduction of Cr(VI) to Cr(III) with WSBC. The high concentration of Cr(III) in the aqueous system (Fig. 12) can be then correlated to the formation of soluble organometallic Cr(III) species (e.g., such as Cr(III)-carboxyl and Cr(III)-carbonyl complexes) and the limited precipitation of $Cr(OH)_3$ at pH less than 3.7.

### *3.5 Spatial distribution of Cr in Cr-laden WSBC*

#### *3.5.1 Morphology of Cr-laden WSBC*

The adsorption-coupled-reduction of Cr(VI) with WSBC produced some major changes in the surface functionality of WSBC, as described in the previous sections. To determine if any Cr(III) precipitates post Cr(VI) reduction were present on the WSBC surface, SEM analyses of the original WSBC (Fig. 21) were compared to those of Cr-laden WSBC at pH 2 with 170 μM Cr(VI) (Fig. 22), 700 μM Cr(VI) (Fig. 23), and 1300 μM Cr(VI) (Fig. 24).

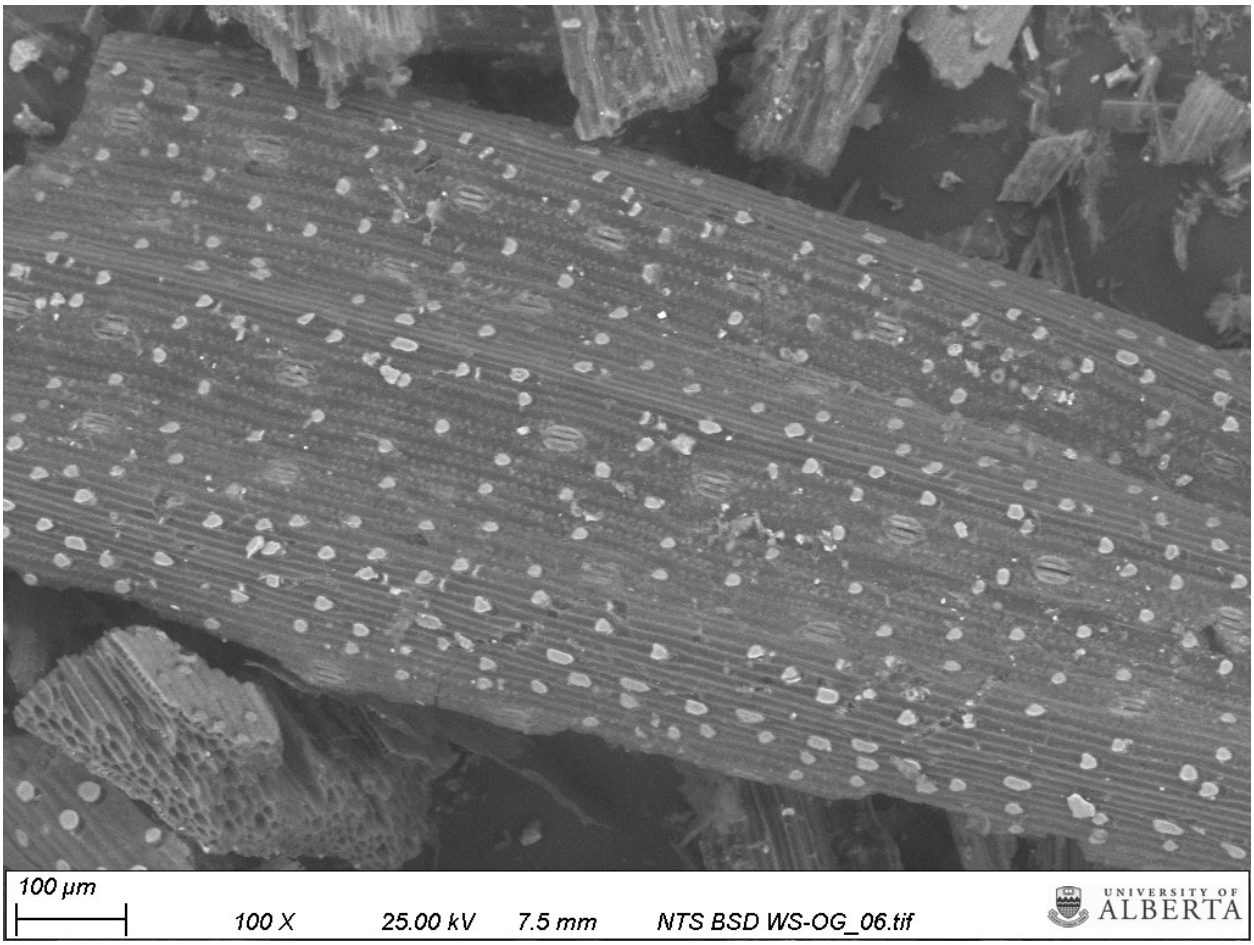


***Figure 21.*** *SEM image of original WSBC at 100x magnification*

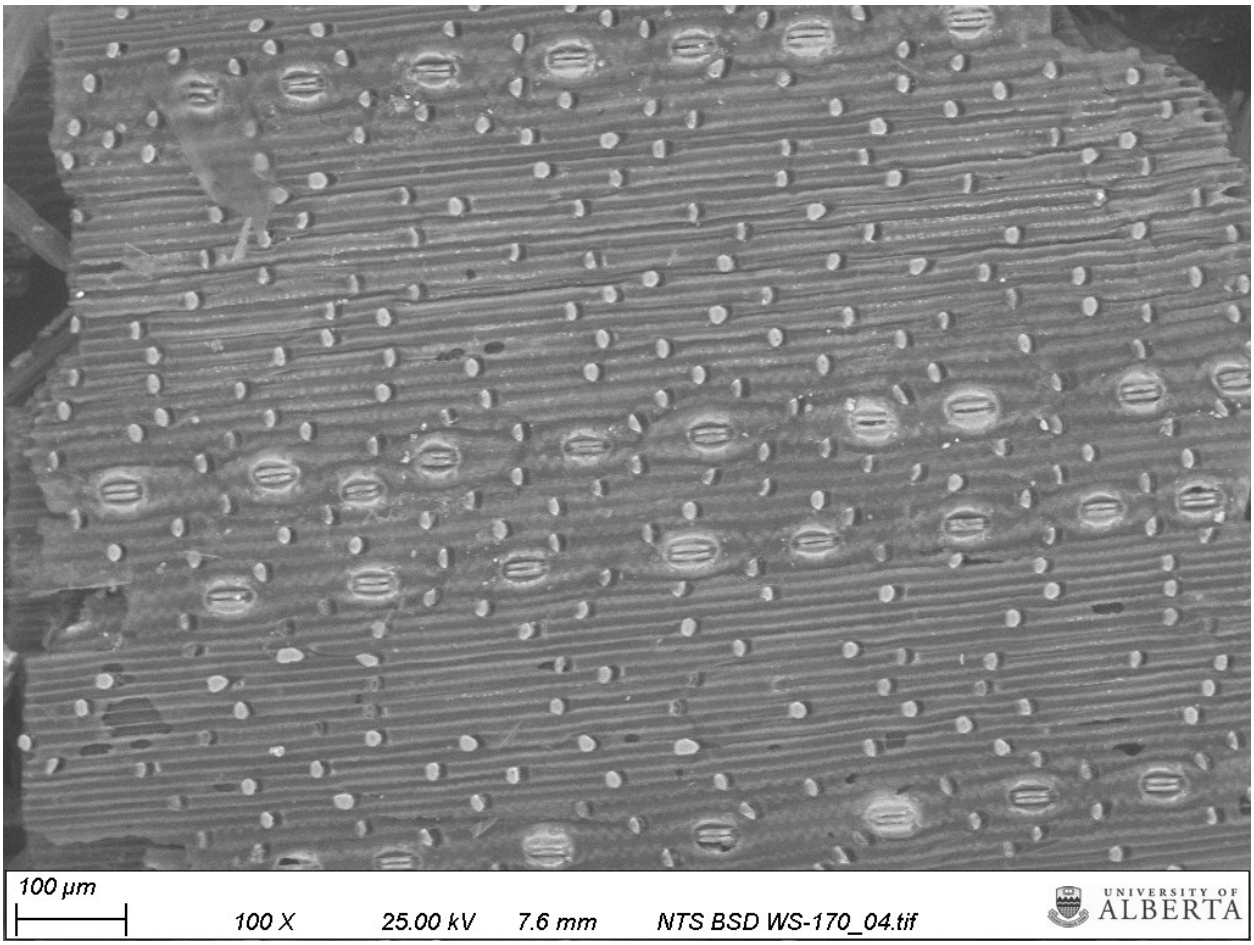


***Figure 22.*** *SEM image of Cr-laden WSBC with initial 170 µM Cr(VI) at 100x magnification*

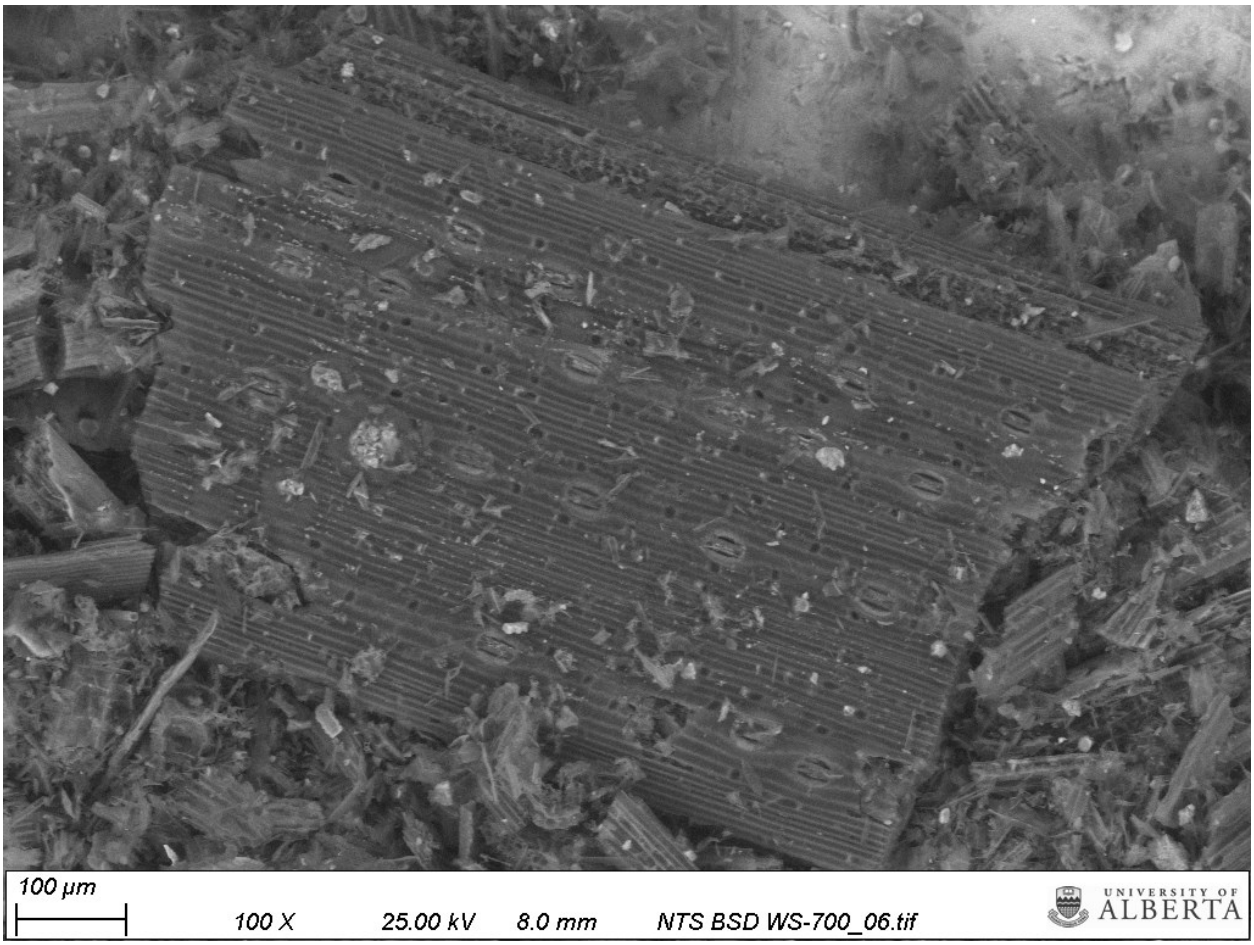


***Figure 23.*** *SEM image of Cr-laden WSBC with initial 700 µM Cr(VI) at 100x magnification*

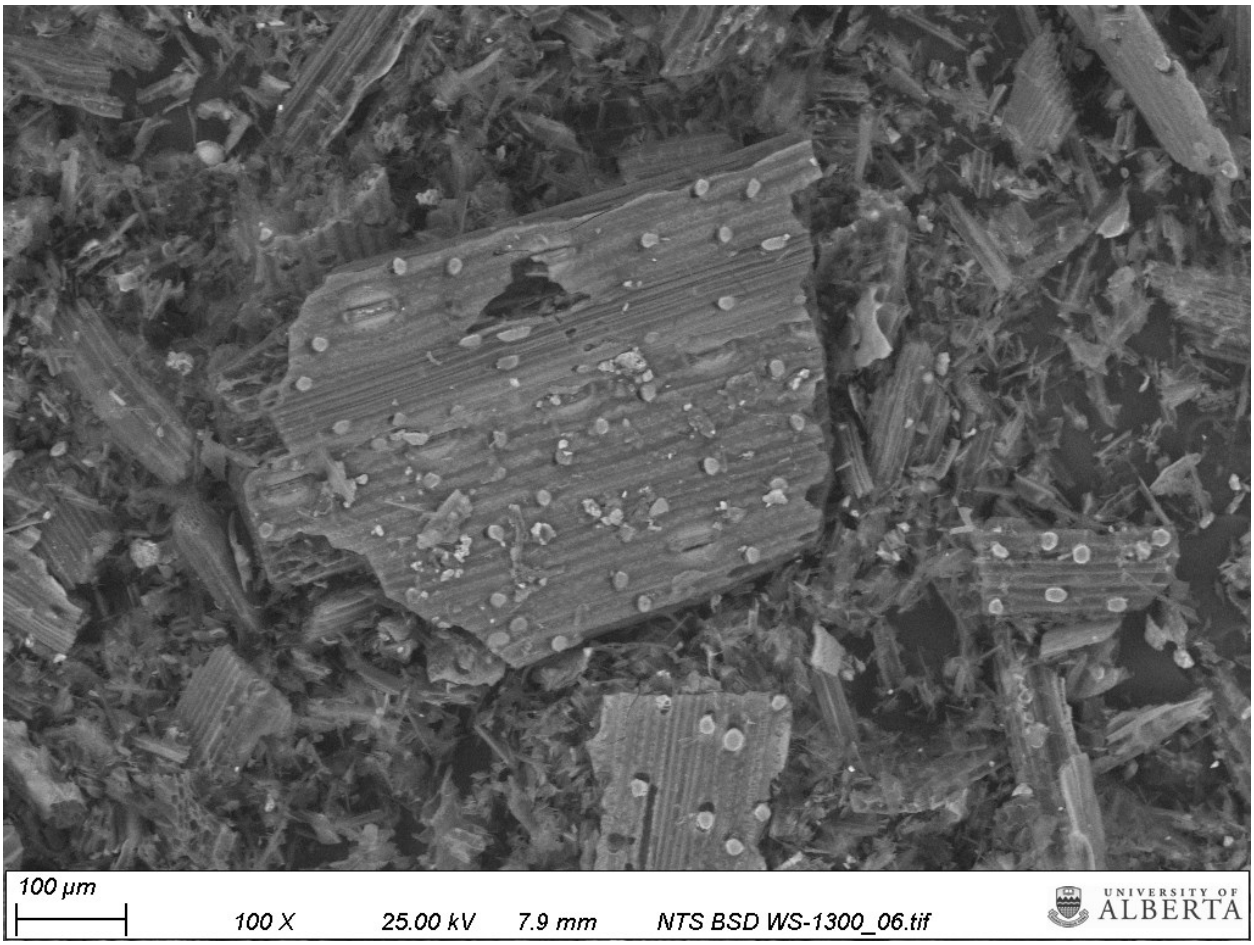


***Figure 24.*** *SEM image of Cr-laden WSBC with initial 1300 µM Cr(VI) at 100x magnification*

The SEM results of Cr-laden WSBC samples and raw WSBC indicated that there were no observable changes in morphology in WSBC as the Cr(VI) concentration increased from zero to 1300 µM Cr(VI). Work done by Ahmadi *et al*. (2016) demonstrated the removal of Cr(VI) with dew melon peel derived biochar, and indicated that the interaction of Cr(VI) with biochar resulted in a decrease of protrusions and roughness at the surface of the biochar; however, such changes were not observed in WSBC. It proved challenging to compare the WSBC solids from the various experimental conditions, since the samples contained intact and degraded biochar material, regardless of whether the sample contained Cr(VI). Comparisons were performed only for biochar grains that were at least 500 µm along the transverse section, parallel to the stromata. The stromata

were relatively unchanged in all solids, as well as the morphology and distribution of concentrated amorphous Si nodules at the surface of the biochar. EDS spectra were also collected, and provide evidence of the Cr loading present in each of the samples (Fig. 25).

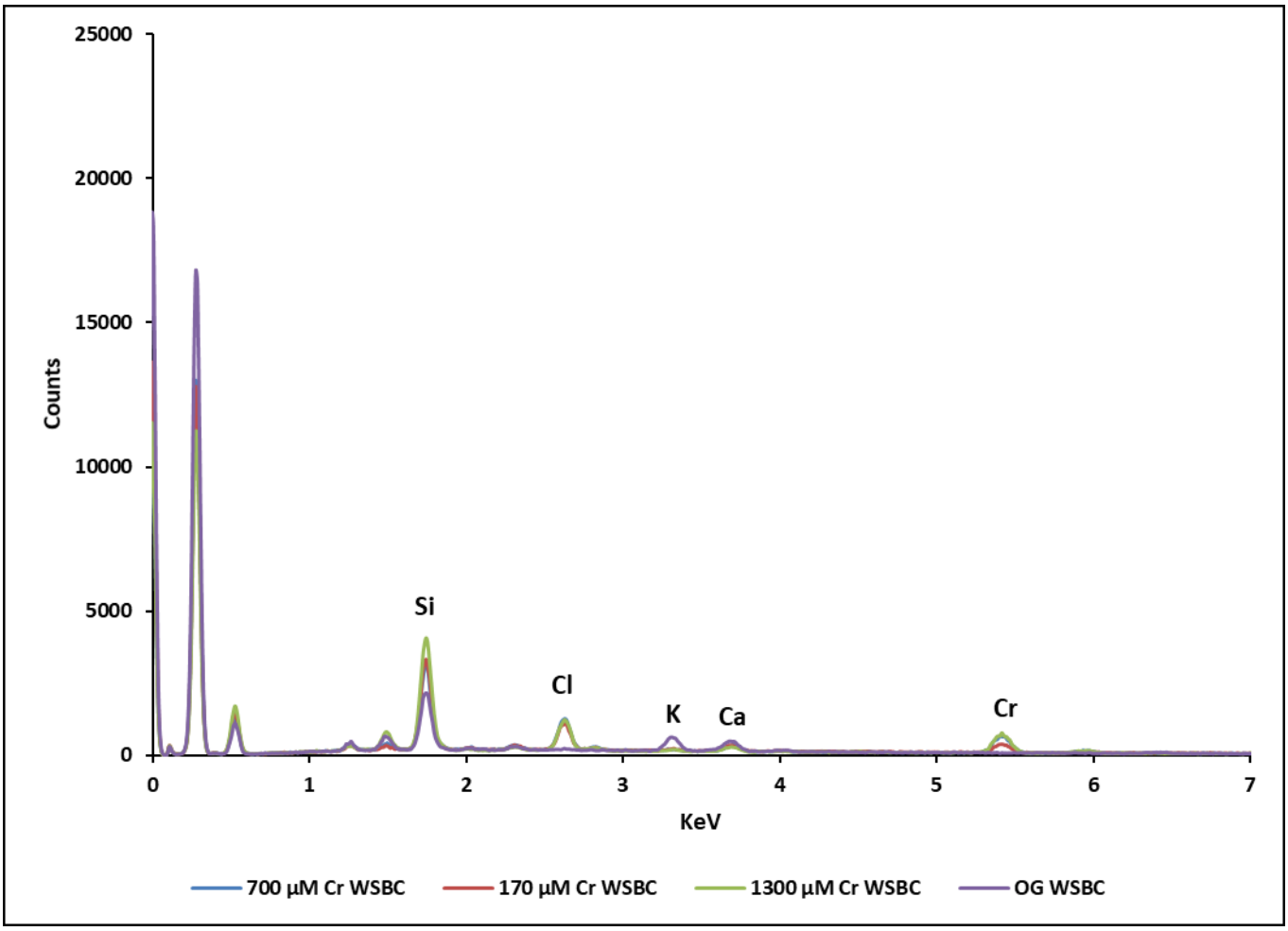


***Figure 25.*** *EDS results of original and Cr-laden WSBC with 170, 700, and 1300 µM Cr(VI)*

WSBC is comprised of fibrous channels with varying pore sizes that could provide access for Cr(VI) diffusion (Choppala *et al*., 2012; Khare *et al*., 2013). The lack in morphological changes has two possible explanations: (1) the high stability and recalcitrance of WSBC from its high aromaticity and Si content prevents structural damage even under acidic conditions or from the redox reactions with Cr(VI), and (2) nanoscale Cr(III) precipitates are formed, but were too small

to image by SEM analysis. Nonetheless, the surface of WSBC, before and after Cr adsorption and reduction processes, remained unchanged in the SEM analyses, with no obvious formation of surface precipitates and any changes in morphology.

### *3.5.2. Distribution of Cr in Cr-laden WSBC*

In order to determine the distribution of Cr in Cr-laden WSBC samples, thin sections of Cr-laden WSBC at pH 2 and 2.5 were made. To identify a subset of grains to analyze, back-scatter electron (BSE) images, produced at the electron probe microanalyzer (EPMA) of high Cr locations, with their respective X and Y coordinates, were obtained. Locations of prominent Cr content were then analyzed in VESPERS to produce XRF maps of Cr and were correlated with their respective BSE images. BSE images correlated with their respective Cr fluorescence map of Cr-laden WSBC at pH 2.5 and pH 2 are portrayed in Fig. 26 and 27, respectively. Combination of both techniques provided us compelling evidence of the distribution of Cr at the surface of individual WSBC grains at the micron scale.

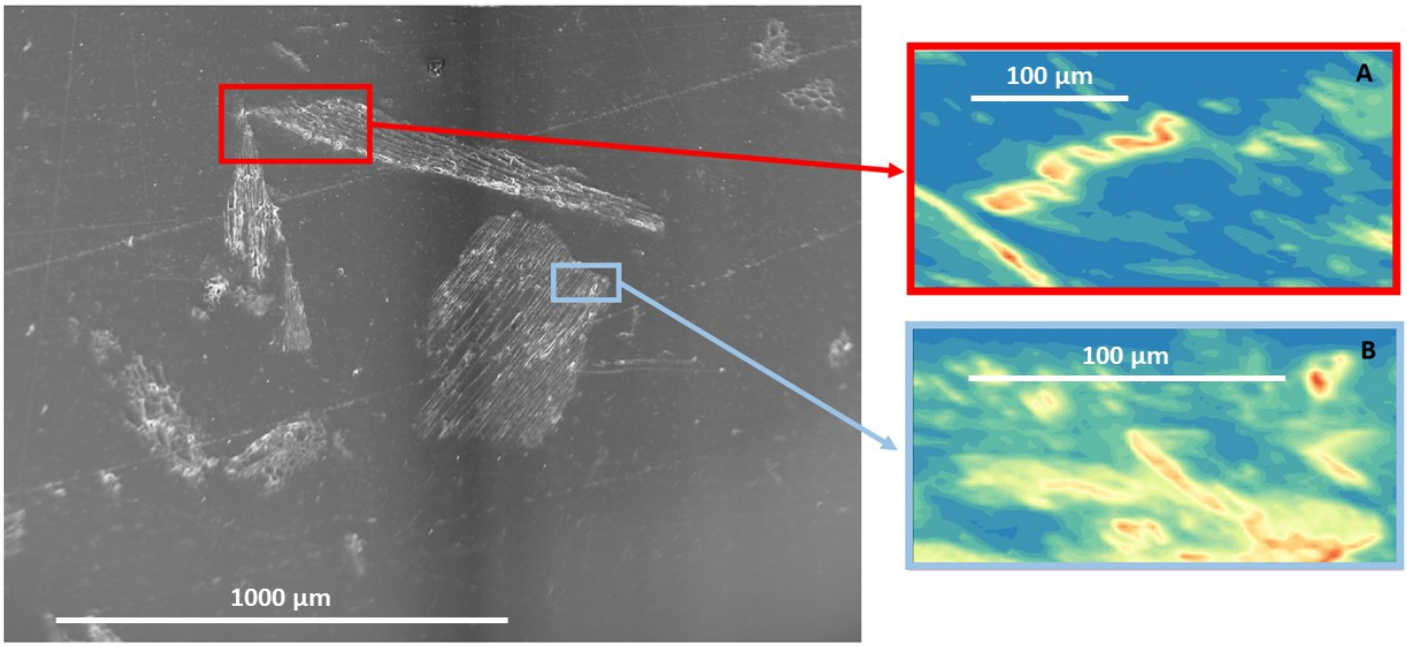


***Figure 26.*** *Correlated BSE maps of Cr-laden (pH 2.5) WSBC with Cr fluorescence map at two different localities, displaying the heterogeneous Cr distribution and high-density Cr localities*

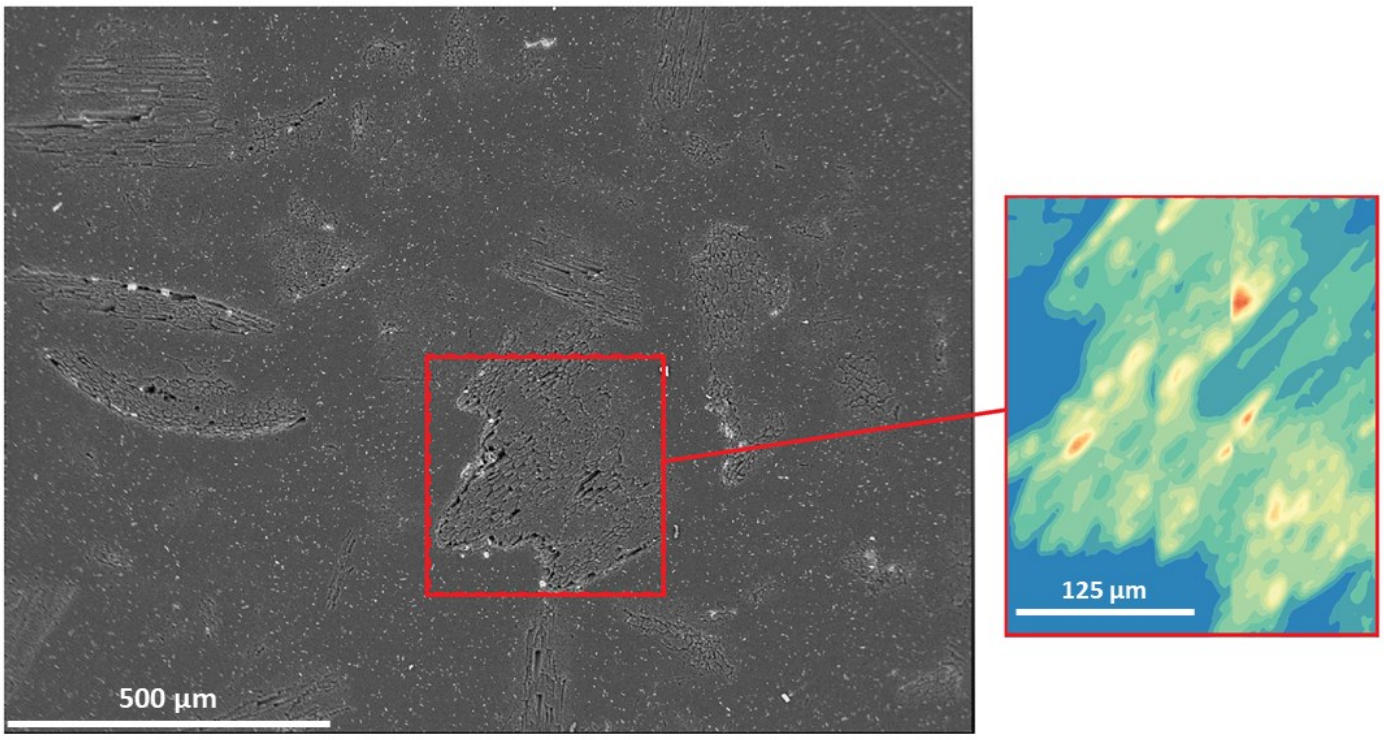


***Figure 27.*** *Correlated BSE maps of Cr-laden WSBC (pH 2) with Cr fluorescence map of a single WSCB grain, displaying the heterogeneous Cr distribution and high-density Cr localities*

The Cr fluorescence maps correlated well with the SEM BSE images, as indicated by the clearly similar delineation of the grain-matrix boundary. Two different grains were located and analyzed for the pH 2.5 condition, and consistent results. Fig. 26B shows the highly heterogeneous Cr distribution, which was also found in an SEM-EDX study of Cr(VI) bound to biochar by Tytłak *et al.* (2015). Highly concentrated Cr spots were also observed, for example, in Fig. 26A, near the upper edge of the matrix-biochar boundary. A larger map of Cr distribution was obtained at pH 2, which involved the compilation of several synchrotron XRF maps (Fig. 27.). At pH 2, the heterogeneity of Cr, along the complete grain was obvious, including three spots of high Cr accumulation. In this case, none of these accumulations was near the edges of the grain. Such results confirmed that although distribution of Cr along the biochar is broadly generally heterogeneous, there are some locations that display unusually elevated concentrations of Cr.

*3.5.3 Correlation between aromaticity of WSBC and high Cr localities*

Raman spectroscopy was performed to evaluate the order of the carbonaceous material in WSBC. Previous studies have often focused on the widths, position and ratios of peaks between 1580 to 1610 $cm^{-1}$, attributed to the graphite band (G band), and between 1325 to 1380 $cm^{-1}$, corresponding to the defect band (D band) (Nanda *et al.*, 2013; Zhao *et al.*, 2013). The D band, centered at approximately 1357 $cm^{-1}$, represents the structural defects in highly ordered carbonaceous material (aromatics with $\geq$ 6 rings), and is correlated to in-plane vibrations of $sp^2$-bonded C from such structural defects (Keown *et al.*, 2008; Zhao *et al.*, 2013). The G band, centered at approximately 1580 $cm^{-1}$, originates from the in-plane vibration of $sp^2$ carbon atoms found in graphitic material and the aromatic ring quadrant breathing, with the observed G band resulting from the aromatic

ring system rather than from the low-intensity graphite structures (Chia *et al.*, 2012; Keown *et al.*, 2008; Zhao *et al.*, 2013). Biochar produced at differing pyrolysis temperatures will show considerable differences in the Raman spectra at these band locations. For instance, Kim *et al.* (2011) showed that switchgrass and pine wood biochar produced at 450$^{o}$C contained less highly ordered C–C associated with D bands than did switchgrass and pine wood biochar produced between 600$^{o}$C and 800$^{o}$C. Such results show that with increasing pyrolysis temperature, the D peaks associated with highly ordered carbonaceous structures will increase, since induced C dislocation generates defects more easily at elevated temperature (Xiao & Chen, 2017).

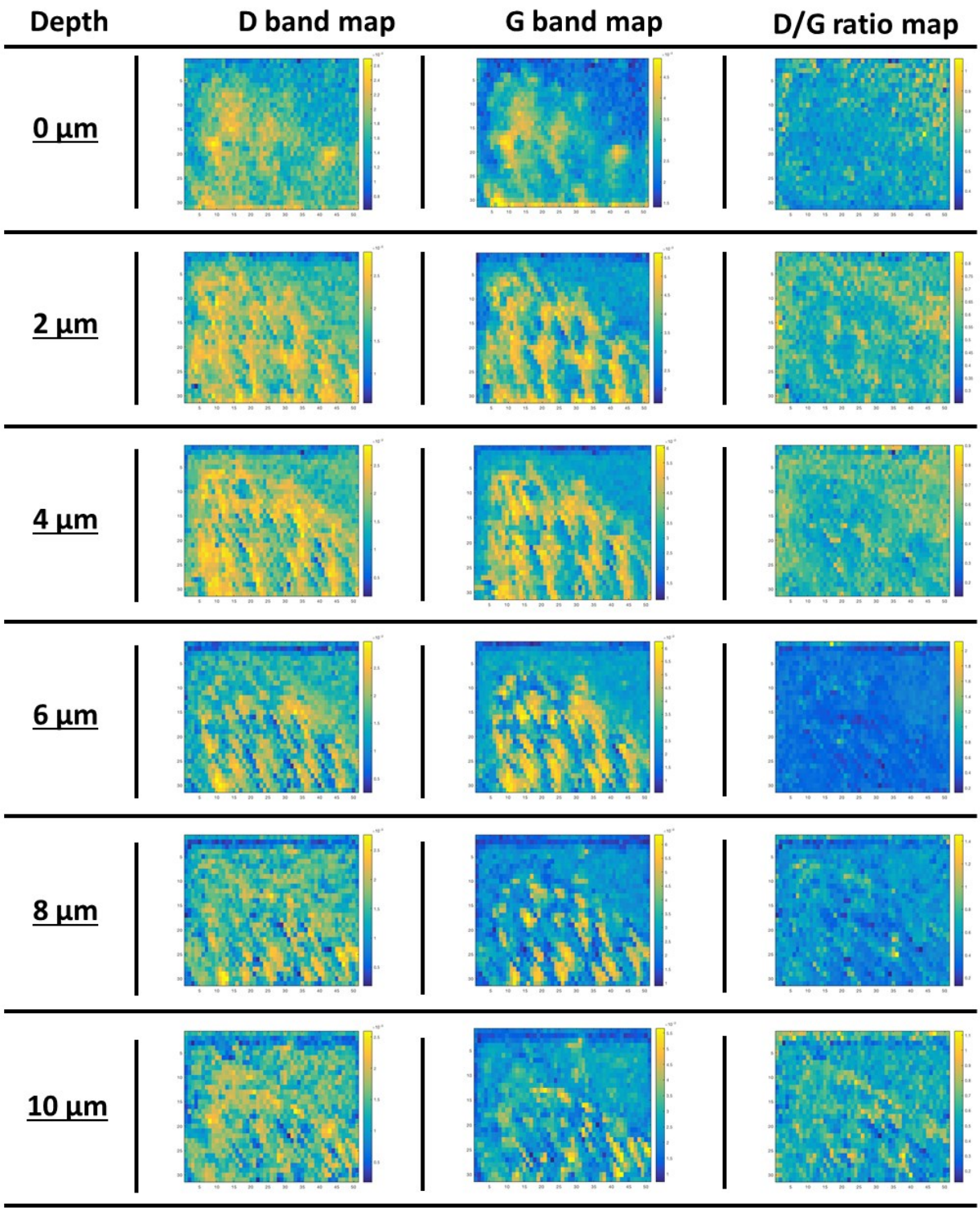


***Figure 28.*** *Raman maps of D band, G band and D/G ratios of Cr-laden WSBC at pH 2, collected at depths of 0, 2, 4, 6, 8 and 10 µm*

By modeling the ratios between D and G bands (D/G) for each sample, the spatial distribution of D/G ratio could be correlated with the high Cr spots. As mentioned in previous sections, a decrease in H/C is the result of biomass undergoing dehydrogenation from the loss of volatiles. Therefore, a higher D/G ratio would indicate more aromaticity contributed by a more extensive aromatic ring system. Biochar is not a well-defined chemical substance and contains multiple forms of C including partly charred biomass, chars, soot and graphite (Keiluweit *et al.*, 2010). The various components of biochar are classified as water-soluble organics, dense aliphatic and insoluble aromatic structures (Xiao & Chen, 2017). A high degree of heterogeneity in WSBC might be expected at the micron scale, due to the numerous types of carbon components comprising its entirety. This would yield varying D/G ratios, from nanocrystalline aromatic clusters to amorphous carbon structures. The low H/C and high D/G regions due to the nanocrystalline benzene ring cluster regions could provide enhanced regions for electron transfer and reduction of Cr(VI) to Cr(III). To evaluate this possibility, a comparison between the synchrotron XRF Cr maps and the D/G ratio Raman spectroscopy maps was made, to provide a possible explanation for the micron-scale regions of high Cr accumulation.

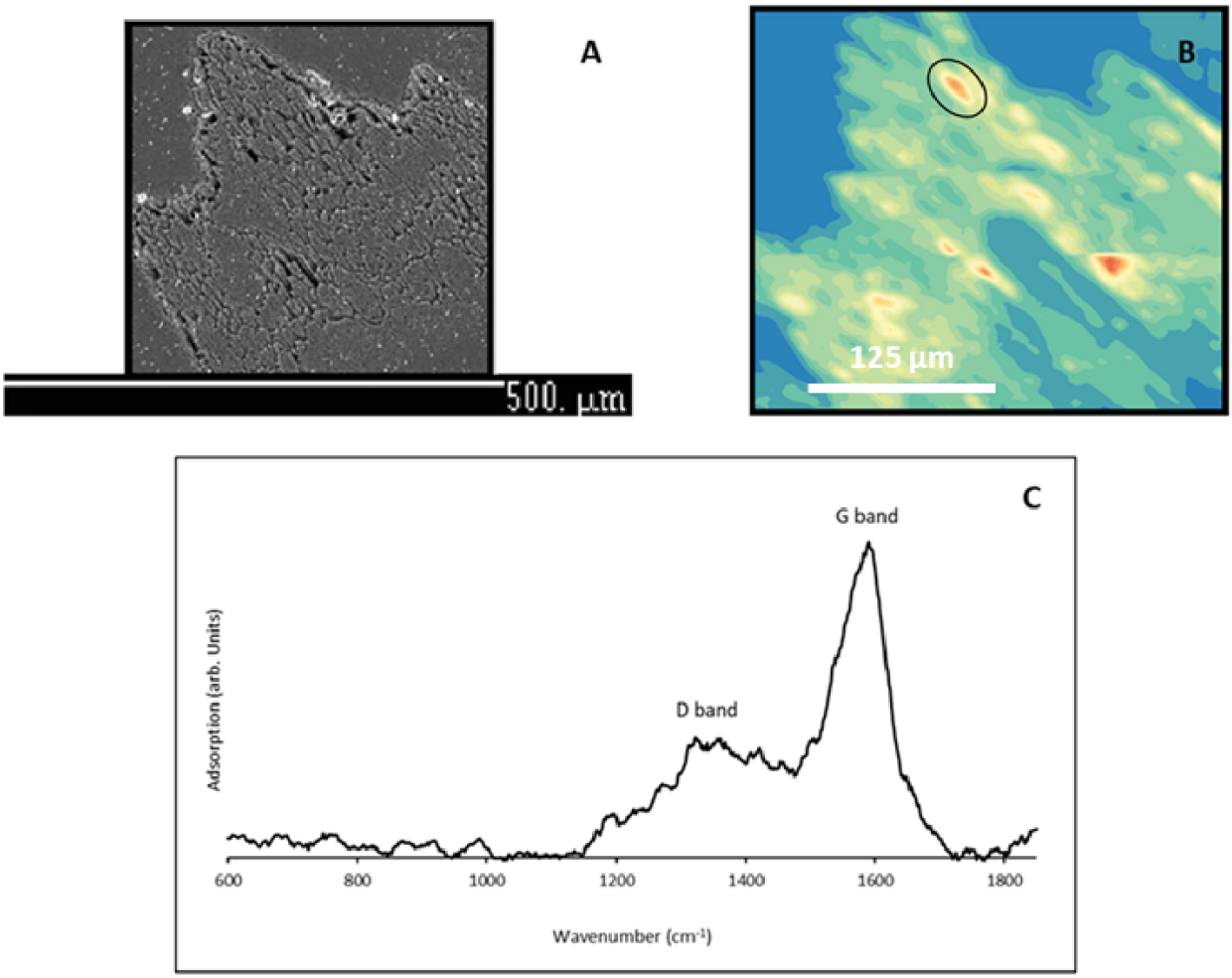


***Figure 29.*** *Scanning electron (A) and XRF Cr maps of Cr-laden WSBC at pH 2. Average Raman spectra of Cr-laden WSBC at pH 2, showing D and G bands (C)*

D band, G band and D/G ratio maps were subsequently generated using Matlab at the depths measured by Raman ranging from 0 µm (the biochar surface) to 10 µm, in 2 µm increments (Fig. 28). The grain boundary is well defined in the Raman microprobe maps, and it comprises the biggest peak in the corresponding Raman spectra of the Cr-laden WSBC grain (middle peak in Fig. 29A & 29B). Overall, the average D/G ratio for WSBC at all depths was 0.5482±0.0343, with the highest D/G ratio located at 8 µm depth with, near the bottom right corner of the map. Just as in the study of Xiao *et al.* (2016), the bulk D/G ratio was slightly above the ratio of

electrochemically prepared graphene quantum dots. This was expected, since high-Si biomass and similar pyrolysis parameters were employed in their study and in ours (5$^{o}$C min$^{-1}$ to a final 500$^{o}$C). Therefore, graphene quantum dot-like structures may be present in WSBC.

Comparison of XRF Cr maps with D/G ratio maps could link the high Cr localities to regions of increased carbon order in WSBC – regions which should have higher capacity to transfer electrons by moving electrons across connected benzene rings. Only one high Cr density spot could only be correlated (Fig. 29B. circled in black). The distribution of D/G maps at all different depths, from 0 to 10 μm, displayed a highly homogeneous ratio, with little pervasive evidence linking increased Cr density with high D/G ratio locations. Only at 8 μm depth was one spot located that could potentially relate to the high Cr spot. However, since only one spot was found at all depths mapped, it suggests that not only is the D/G ratio of WSBC highly homogenous, but also that the high Cr locations are unlikely to be related with isolated high aromatic localities. To reach a conclusive answer, a more extensive Raman mapping study would need to be conducted, including further XRF microprobe mapping of micron-sized regions of high Cr accumulation.

## CONCLUSIONS AND FUTURE DIRECTION

Biochar derived from wheat straw, provided by the ABI, was analyzed for its physicochemical characteristics, and tested for its removal capacity of Cr(VI) from aqueous solutions. Intermediate pyrolysis temperature combined with slow heating rate developed a biochar containing higher proportion of ashes in comparison to previous WSBC produced under similar pyrolysis parameters. The elevated ash content of WSBC was the result of the thermal decomposition of biomass containing elevated concentrations of Si and alkali and alkaline elements at 500 to 500$^{o}$C. The elevated levels of ash from the pyrolysis mechanism of WS influenced the SA of WSBC;

however, the SA of WSBC (26.64 $m^2$ $g^{-1}$) was well within normal ranges as indicated by previous wheat straw derived biochar studies. The pH of WSBC was abnormally low at 6.7, with regards to the average wheat straw derived biochar pH of ~9. The pH anomaly was again affected by the concentration of alkali and alkaline elements. The relative concentrations of such elements, including Na, K, Ca and Mg, were 50 % less than the wheat straw derived biochar displaying high alkaline pH; the reduced amount of alkali and alkaline metals influenced the pH and was explained by the electrical conduction and pH relationship. WSBC, having less alkali and alkaline elements, would provide a lower EC value since high pH were attributed to the hydrolysis of higher concentration of salts, alkali and alkaline metals.

Sequential extractions and alkaline fusion analyses results of WSBC revealed that it has potential as a future soil amendment. The concentration of alkali and alkaline in metals in WSBC could promote the neutralization of acidic soils, even with a circumneutral pH of 6.77. Si, being the second most abundant element after C, could provide a variety of benefits, influencing both the soil systems and plant growth. In fact, the concentration of Si in WSBC was so high (46 mg $L^{-1}$) that it could provide additional Si to the soil over long periods of time, especially to Si-depleted soils from the harvesting of rice in Asia as indicated by Song *et al.* (2014). Batch or pilot scale experiments elucidating the agronomic impact of WSBC incorporation to Si-depleted for crop production or Si restauration in soils could be a suitable project for future farming applications. The concentrations of Cu and Pb were within normal soil levels and were dominated by the their residual fraction. In contrast to Cu and Pb, the total Zn was dominated by the exchangeable/acid soluble Zn fraction, with as much as 897 ppm of labile Zn available from leaching from WSBC. A comprehensive soil-WSBC pilot scale study could elucidate the positive effects of WSBC, as well as the side effects by potential leaching of Zn should be considered in the future. The structural

integrity of WSBC was elucidated to determine the recalcitrance of WSBC towards degradation. WSBC exhibited great structural stability and high recalcitrance from the low O/C molar ratio and high Si content results.

Pyrolysis temperatures of 500$^{o}$C-550$^{o}$C resulted in an WSBC with an O/C molar ratio < 1, often indicative of a highly aromatic arrangement. Previous physicochemical analyses on BC produced at different pyrolysis temperatures indicate that a BC with a O/C value less than 0.2 have the structural stability to remain in soils for at least 1000 years. Nonetheless, the higher proportions of mobile C in comparison to other WSBC suggested that WSBC could be at higher risk to degradation from microbial activity. However, microbial activity would only be limited to the labile C and should not have any greater effect on the fixed C portion of WSBC. The elevated concentrations of Si in WSBC were expected to increase the stability and longevity by the formation of intertwined Si-C structures and Si coated C as the result of the pyrolysis of Si-rich biomasses at intermediate temperatures. The purpose of silica in plants is to promote stability by the growth of rigid plant structures, and the pyrolysis of such biomasses would promote structural stability from the formation of Si-C structures involving Si and quartz and aromatic C. H/C molar ratio values and Raman results indicated that WSBC contained 4 x 4 benzene ring clusters and graphene quantum dot-like structures present. As much as 98% of the Si in WSBC was in the residual fraction, indicating that Si in the BC was highly recalcitrant towards dissolution and would aid in the long-term recalcitrance of WSBC in environmental settings. The remaining 2% of Si, especially the 0.44% from the labile Si fraction could be readily used by plants; however, the amount of Si that WSBC would be readily available to soils and plants remains unknown. SEM images of WSBC further confirmed the high Si content of WSBC. Studies involving the oxidation and degradation of WSBC in common soils would provide more detailed capabilities of the

recalcitrance of WSBC to the attacks by microbial biota and the natural chemical degradation processes and environmental oxidation. Such a study could help complement the ability of WSBC to either aid or damage the soil as a soil amendment, and would help promote the understanding of the capabilities of WSBC to retain $CO_2$ over extended periods of time for the determination of degradation rates for a comprehensive $CO_2$ sequestration application. Overall, WSBC was deemed a highly stable biochar capable of providing important macronutrients to soils, with great capabilities of promoting plant stability in Si-depleted soils. Leaching of Zn could potentially induce a negative effect into soil, however, based on the current results of the physicochemical analyzes of WSBC, future applications of WSBC to soils could help with soil amendments, and $CO_2$ sequestration, especially if Zn could be leached from WSBC prior to application. WSBC produced from wheat straw containing Zn and higher alkali and alkaline metals would yield WSBC with a circumneutral pH, essential nutrients and lesser toxic metals, which would involve a more selective biomass approach prior to pyrolysis.

Following the complete characterization of WSBC, the capability of Cr(VI) removal via reduction and adsorption were elucidated for complexation, reaction rates, changes in Cr oxidation, and changes in the morphology of WSBC. Kinetics studies revealed that Cr(VI) was removed from solution with a faster rate at lower pH, and this was explained by the proton-dependent Cr(VI) removal by WSBC. The mechanism was described as an adsorption-coupled-reduction pathway, involving the fast adsorption of Cr(VI) to WSBC followed by the subsequent reduction to Cr(III) by an electron transfer model from the biochar itself to the Cr(VI) oxyanions. The lower pH of solution accelerated the adsorption of Cr(VI) by a quicker complexation between the protonated surface of WSBC and the Cr(VI) oxyanions. In addition, speciation of Cr(VI) was also affected by changing the distribution of chromates and dichromates. Overall, Cr(VI) speciation was dominated

by hydrogen chromates at all Cr(VI) concentrations and pH. Yet, as the Cr(VI) increased from 170 μM to 1300 μM Cr(VI), the concentrations of dichromates increased due to the polymerization of chromates. Changes in Cr(VI), especially at elevated Cr(VI) concentrations, could have resulted in a relative increase in complexity when modelling Cr(VI) reduction kinetics.

Following adsorption, the reduction of Cr(VI) to Cr(III) was attained with the transfer of 3 electrons from the WSBC matrix. Similar to the adsorption process, reduction of Cr(VI) was pH dependent, as described by the stoichiometry of the redox reaction of Cr(VI)-Cr(III) with an electron donor. Seven protons were consumed per unit of Cr(VI) to produce Cr(III), but no changes in pH were observed since all experiments were obtained at pH between 2 to 3, and the acidity of the system provided enough buffering capacity to keep the pH constant. Complete removal of Cr, involving both sorption and reduction, was only attained at lower Cr concentrations and at pH 2 and 2.5. Complete reduction of Cr(VI) was only observed with 170 μM Cr(VI) and at pH 2 within 6 days. The reduction processes at higher pH involved times between 300 and 373 hours, rather than the 120 hours observed at pH 2. At 170 μM Cr, the rate-limiting factor was only the Cr(VI) concentration. Less availability of protons at pH 3 was detrimental to the rate of the Cr(VI) reduction process, and made the reduction of Cr(VI) by WSBC rather ineffective in comparison to pH 2 and 2.5.

At elevated Cr(VI), especially at 1300 μM Cr(VI), the abundant Cr(VI) anions removed the easily accessible electrons resulting in the rapid decrease of reduction potential of WSBC with a two-fold explanation: (1) Cr(VI) would have to diffuse deeper into the biochar matrix to find more electrons, and (2) electrons would had to travel longer distances along the benzene rings of WSBC for redox processes. Both processes greatly affected the reduction of Cr(VI) to Cr(III) at elevated initial Cr(VI) concentration. Plotting the changes in concentration over time yielded

different results for lower concentration studies: (1) at lower Cr(VI) concentrations, it reflected a pseudo-first-order reaction as a function of pH, while with increasing initial Cr(VI) concentrations, the reduction rate model had a better match with a second-order reduction model. Thus, the focus for the reduction model was utilized at lower Cr(VI) concentrations and the pH series. More detailed kinetics modeling, involving intermediate to higher initial Cr(VI) concentrations and higher pH, possibly between 4 and 5, should be pursued following the results from this project. The kinetics model of Cr(VI) by WSBC resulted in a pseudo-first order kinetics with an intrinsic rate of 5.459 ± 1.502 $M^{-1}$ $hr^{-1}$. From the colorimetry and ICP-MS results for removal, complete reduction of Cr(VI) to Cr(III) was obtained at pH 2, yet, approximately 70 μM Cr(III) were left in solution. At pH 3, only 40 μM total Cr was left in solution, with most of the fraction in the Cr(VI) form. This indicated that at pH 2, WSBC did not have the capacity to fully remove Cr(III) from solution, while at pH 3, more total Cr was removed but most of it existed in the hexavalent form. Elevated levels of Cr(III) in solution at pH 2 were attributed to the formation of stable Cr(III) organometallic species, but it was also influenced by the decrease in Cr(III) hydroxide precipitation at pH lower than 5.

Utilizing the Cr-laden WSBC samples from batch kinetics experiments, complexation of Cr(VI) and Cr(III), along with the changes in surface functionality of WSBC, were elucidated using XANES, EXAFS and FTIR. Reference materials of both Cr(III) and Cr(VI), with their respective linear combination fittings indicated that carbonyl, carboxyl and hydroxyl moieties were responsible for the formation of Cr(III) hydroxides and Cr(III) organometallic complexes. Cr(III) hydroxyl dominated at pH 2, 2.5 and 3.7. Cr(III) carbonyl complexes decreased from 10 % to 0% when the pH decreased from 3.7 to 2, indicating that the carbonyl groups which resulted from the oxidation of WSBC also underwent oxidation while the reduction of Cr(VI) took place.

Cr(VI) was not present at pH 2, as previously described by the kinetics results, while a late surge of Cr(III) carboxyl was only observable at pH 2. Total reduction of Cr(VI) to Cr(III) yielded major proportions of hydroxyl and carboxyl groups. Spectral analyses confirmed the evolution and complexation pathways of the Cr species. The surface functional of WSBC changed drastically as the reduction of Cr(VI) took place. Reduction of Cr(VI) was coupled to the oxidation of phenolic groups, which are OH groups located adjacent to benzene rings capable of providing easily electrons for redox, as well as hydroxyl groups, with such oxidation producing carbonyl-containing quinone groups that were capable of Cr(III) complexation. Further oxidation of quinone groups led to the formation of carboxyl groups, which subsequently formed Cr(III) carboxyl groups at pH 2. Complexation reactions of carbonyl, carboxyl and hydroxyl groups with Cr(III) resulted in stable complexes that would remain in solution. Since greater reduction of Cr(VI) was achieved at pH 2, greater concentration of soluble Cr(III) complexes, especially with carboxyl groups, would then be released into solution. EXAFS fits of Cr-laden WSBC samples could confirm the Cr(III) carboxyl/carbonyl and Cr(III) hydroxide species by modelling of Cr-C and Cr-Cr shell fitting, respectively. In addition, the Cr-Cr shell fitting indicated that amorphous Cr(III)-hydroxides (γ-CrOOH) formed at the Cr-WSBC boundary. For a full application of WSBC for the reduction of Cr(VI) and full removal of Cr(III), further treatments should be elucidated to promote Cr(III) sequestration post Cr(VI) removal.

The combination of fluorescence, BSE and Raman maps determined that the distribution of Cr along WSBC was mostly heterogeneous with erratic high-density Cr localities. It is likely that the high heterogeneity of WSBC allows for high aromatic spots that could provide easily accessible electrons to Cr(VI), thus facilitating greater quantities of Cr to accumulate in highly aromatic spots. However, Raman D/G ratio maps indicated that the aromaticity of WSBC was

highly homogeneous between the surface and at a depth of 10 microns into the biochar. Therefore, the presence of high density Cr hotspots is due to an unknown mechanism that could be studied in the future.

Generally, under the right pyrolysis of WS, WSBC could be used as possible soil amendment and such work should the future focus of WSBC. WSBC could still be utilized as a contaminant removal agent, but physical or chemical activation should be considered to some degree, even with simple procedures such as acid washing to decrease the ash content, or chemical oxidation to increase its O-containing functional groups as indicated by a low O/C molecular ratio, or producing whet straw biochar with different pyrolysis characteristics to retain high concentrations of surface functional groups.

# REFERENCES


Agilent Technologies. (2015). Agilent 8800 ICP-QQQ application handbook. 2nd edition. Retrieved October 2016 from https://www.agilent.com/cs/library/brochures/5991-2802EN_electronic.pdf

Agrafionti, E., Kalderis, D., & Diamadopoulos, E. (2014). Ca and Fe modi fi ed biochars as adsorbents of arsenic and chromium in aqueous solutions, *146*, 444–450. https://doi.org/10.1016/j.jenvman.2014.07.029

Agrafioti, E., Kalderis, D., & Diamadopoulos, E. (2014). Arsenic and chromium removal from water using biochars derived from rice husk, organic solid wastes and sewage sludge. *Journal of Environmental Management*, *133*(January), 309–314. https://doi.org/10.1016/j.jenvman.2013.12.007

Agricultural Statistics. (2011). Analytical Paper Canadian Agriculture at a Glance Corn : Canada's third most valuable crop, (96).

Ahmad, M., Lee, S. S., Dou, X., Mohan, D., Sung, J. K., Yang, J. E., & Ok, Y. S. (2012). Effects of pyrolysis temperature on soybean stover- and peanut shell-derived biochar properties and TCE adsorption in water. *Bioresource Technology*, *118*, 536–544. https://doi.org/10.1016/j.biortech.2012.05.042

Ahmad, M., Rajapaksha, A. U., Lim, J. E., Zhang, M., Bolan, N., Mohan, D., … Ok, Y. S. (2014). Biochar as a sorbent for contaminant management in soil and water: A review. *Chemosphere*, *99*, 19–23. https://doi.org/10.1016/j.chemosphere.2013.10.071

Ahmadi, M., Kouhgardi, E., & Ramavandi, B. (2016). Physico-chemical study of dew melon peel biochar for chromium attenuation from simulated and actual wastewaters, *33*(9), 2589–2601. https://doi.org/10.1007/s11814-016-0135-1

Alexander, G., Heston, W., & Iler, R. (1954). The solubility of amorphous silica in water. *J. Phys. Chem.*, *58*(6), 453–455. https://doi.org/10.1021/j150516a002

American Public Health Association, American Water Works Association, & Water Environment Federation. (1999). Standard Methods for the Examination of Water and Wastewater. *Standard Methods*, 541.

Anderson, R. A. (1997). Chromium as an essential nutrient for humans. *Regulatory Toxicology and Pharmacology : RTP*, *26*(26), S35-41. https://doi.org/10.1006/rtph.1997.1136

Ankudinov, A., & Rehr, J. (2000). Theory of solid-state contributions to the x-ray elastic scattering amplitude. *Physical Review B*, *62*(4), 2437–2445. https://doi.org/10.1103/PhysRevB.62.2437

Arslan, G., & Pehlivan, E. (2007). Batch removal of chromium ( VI ) from aqueous solution by Turkish brown coals, *98*, 2836–2845. https://doi.org/10.1016/j.biortech.2006.09.041

Atik, C., & Ates, S. (2012). Mass Balance of Silica in Straw From the. *BioResources*, *7*(3), 3274–3282.

Beesley, L., Moreno-jiménez, E., & Gomez-Eyles, J. L. (2010). Effects of biochar and greenwaste compost amendments on mobility , bioavailability and toxicity of inorganic and organic contaminants in a multi-element polluted soil, *158*, 2282–2287. https://doi.org/10.1016/j.envpol.2010.02.003

Beesley, L., Moreno-jiménez, E., Gomez-eyles, J. L., Harris, E., Robinson, B., & Sizmur, T. (2011). A review of biochars ' potential role in the remediation , revegetation and restoration of contaminated soils. *Environmental Pollution*, *159*(12), 3269–3282. https://doi.org/10.1016/j.envpol.2011.07.023

Bian, R., Ma, B., Zhu, X., Wang, W., Li, L., Joseph, S., … Pan, G. (2016). Pyrolysis of crop

residues in a mobile bench-scale pyrolyser: Product characterization and environmental performance. *Journal of Analytical and Applied Pyrolysis*, *119*(April), 52–59. https://doi.org/10.1016/j.jaap.2016.03.018

Cabatingan, L. K., Agapay, R. C., Rakels, J. L. L., Ottens, M., & van der Wielen, L. a. M. (2001). Potential of Biosorption for the Recovery of Chromate in Industrial Wastewaters. *Industrial & Engineering Chemistry Research*, *40*(10), 2302–2309. https://doi.org/10.1021/ie0008575

Cao, Y., Yang, B., Song, Z., Wang, H., He, F., & Han, X. (2016). Wheat straw biochar amendments on the removal of polycyclic aromatic hydrocarbons (PAHs) in contaminated soil. *Ecotoxicology and Environmental Safety*, *130*, 248–255. https://doi.org/10.1016/j.ecoenv.2016.04.033

Chia, C. H., Gong, B., Joseph, S. D., Marjo, C. E., Munroe, P., & Rich, A. M. (2012). Imaging of mineral-enriched biochar by FTIR, Raman and SEM-EDX. *Vibrational Spectroscopy*, *62*, 248–257. https://doi.org/10.1016/j.vibspec.2012.06.006

Choppala, G., Bolan, N., Mallavarapu, M., & Chen, Z. (2010). Sorption and mobility of chromium species in a range of soil types. *19th World Congress of Soil Science, Soil Solutions for a Changing World*, (August), 239–242.

Choppala, G. K., Bolan, N. S., Megharaj, M., Chen, Z., & Naidu, R. (2012). The Influence of Biochar and Black Carbon on Reduction and Bioavailability of Chromate in Soils. *Journal of Environment Quality*, *41*(4), 1175. https://doi.org/10.2134/jeq2011.0145

Christensen, A. N. (1976). Hydrothermal Preparation and Magnetic Properties of Alpha-CrOOH, Beta-CrOOH and Gamma-CrOOH. *Acta Chemica Scandinavica A*. https://doi.org/10.3891/acta.chem.scand.30a-0133

Christensen, A. N., Hansen, P., & Lehmann, M. S. (1977). Isotope Effects in the Bonds of a-CrOOH and a-CrOOD. *Journal of Solid State Chemistry*, *21*(4), 325–329. https://doi.org/10.1016/0022-4596(77)90130-X

Cohen, M. D., Kargacin, B., Klein, C. B., Costa, M., Cohen, M. D., Kargacin, B., … Costa, M. (2008). Critical Reviews in Toxicology Mechanisms of Chromium Carcinogenicity and Toxicity Mechanisms of Chromium Carcinogenicity and Toxicity, *8444*(July). https://doi.org/10.3109/10408449309105012

Costa, M. (2003). Potential hazards of hexavalent chromate in our drinking water. *Toxicology and Applied Pharmacology*, *188*(1), 1–5. https://doi.org/10.1016/S0041-008X(03)00011-5

Costa, M. (2008). Toxicity and Carcinogenicity of Cr ( VI ) in Animal Models and Humans Toxicity and Carcinogenicity of Cr ( VI ) in Animal Models and Humans, *8444*(July), 430–442. https://doi.org/10.3109/10408449709078442

Currie, H. A., & Perry, C. C. (2007). Silica in plants: Biological, biochemical and chemical studies. *Annals of Botany*, *100*(7), 1383–1389. https://doi.org/10.1093/aob/mcm247

Dang, T., Mosley, L., Fitzpatrick, R., & Marschner, P. (2015). Organic Materials Differ in Ability to Remove Protons, Iron and Aluminium from Acid Sulfate Soil Drainage Water. *Water, Air, & Soil Pollution*, *226*, 1–13. https://doi.org/10.1007/s11270-015-2595-z

Das, O., Sarmah, A. K., & Bhattacharyya, D. (2015). Science of the Total Environment Structure – mechanics property relationship of waste derived biochars ☆. *Science of the Total Environment, The*, *538*, 611–620. https://doi.org/10.1016/j.scitotenv.2015.08.073

Deveci, H., & Kar, Y. (2013). Adsorption of hexavalent chromium from aqueous solutions by bio-chars obtained during biomass pyrolysis. *Journal of Industrial and Engineering Chemistry*, *19*(1), 190–196. https://doi.org/10.1016/j.jiec.2012.08.001

Dong, X., Ma, L. Q., & Li, Y. (2011). Characteristics and mechanisms of hexavalent chromium removal by biochar from sugar beet tailing. *Journal of Hazardous Materials*, *190*(1–3), 909–915. https://doi.org/10.1016/j.jhazmat.2011.04.008

Dupont, L., & Guillon, E. (2003). Removal of hexavalent chromium with a lignocellulosic substrate extracted from wheat bran. *Environmental Science and Technology*, *37*(18), 4235–4241. https://doi.org/10.1021/es0342345

Eilers, P. H. C. (2004). Parametric Time Warping. *Analytical Chemistry*, *76*(2), 404–411. https://doi.org/10.1021/ac034800e

Elovitz, M. S., & Fish, W. (1995). Redox interactions of Cr(VI) and substituted phenols: Products and mechanism. *Environmental Science and Technology*, *29*(8), 1933–1943. https://doi.org/10.1021/es00008a010

EPA. (1992). METHOD 7196A - Colormeric Method, (July), 1–6.

Fanning, P. E., & Vannice, M. A. (1993). A DRIFTS study of the formation of surface groups on carbon by oxidation. *Carbon*, *31*(5), 721–730. https://doi.org/10.1016/0008-6223(93)90009-Y

Fellet, G., Marchiol, L., Vedove, G. D., & Peressotti, A. (2011). Chemosphere Application of biochar on mine tailings : Effects and perspectives for land reclamation. *Chemosphere*, *83*(9), 1262–1267. https://doi.org/10.1016/j.chemosphere.2011.03.053

Felten, J., Hall, H., Jaumot, J., Tauler, R., de Juan, A., & Gorzsás, A. (2015). Vibrational spectroscopic image analysis of biological material using multivariate curve resolution–alternating least squares (MCR-ALS). *Nature Protocols*, *10*(2), 217–240. https://doi.org/10.1038/nprot.2015.008

Fendorf, S. E. (1995). Surface reactions of chromium in soils and waters, *67*(94), 55–71.

Fendorf, S. E., Lamble, G. M., Stapleton, M. G., Kelley, M. J., & Sparks, D. L. (1994). Mechanisms of chromium(III) sorption on silica. 1. Chromium(III) surface structure derived by extended x-ray absorption fine structure spectroscopy. *Environmental Science & Technology*, *28*(2), 284–9. https://doi.org/10.1021/es00051a015

Feng, Z. C., Mascarenhas, A. J., Choyke, W. J., & Powell, J. A. (1988). Raman scattering studies of chemical-vapor-deposited cubic SiC films of (100) Si. *Journal of Applied Physics*, *64*(6), 3176–3186. https://doi.org/10.1063/1.341533

Flogeac, K., Guillon, E., Aplincourt, M., Surface, D., & Curie, M. (2003). Speciation of chromium on a straw lignin : adsorption isotherm , EPR , and XAS studies, 714–720. https://doi.org/10.1039/b211411a

Fomina, M., & Michael, G. (2014). Biosorption : current perspectives on concept , definition and application. *Bioresource Technology*, *160*, 3–14. https://doi.org/10.1016/j.biortech.2013.12.102

Gardea-Torresdey, J. L., Tiemann, K. J., Armendariz, V., Bess-Oberto, L., Chianelli, R. R., Rios, J., … Gamez, G. (2000). Characterization of Cr ( VI ) binding and reduction to Cr ( III ) by the agricultural byproducts of Avena monida ( Oat ) biomass, *80*, 175–188.

Garg, U. K., Kaur, M. P., Garg, V. K., & Sud, D. (2007). Removal of hexavalent chromium from aqueous solution by agricultural waste biomass. *Journal of Hazardous Materials*, *140*(1–2), 60–68. https://doi.org/10.1016/j.jhazmat.2006.06.056

Gottipati, R., & Mishra, S. (2010). Process optimization of adsorption of Cr ( VI ) on activated carbons prepared from plant precursors by a two-level full factorial ... *Chemical Engineering Journal*, *160*(1), 99–107. https://doi.org/10.1016/j.cej.2010.03.015

Gould, J. P. (1982). THE KINETICS OF HEXAVALENT CHROMIUM REDUCTION BY

METALLIC IRON, *16*, 871–877.

Guo, J., & Chen, B. (2014). Insights on the molecular mechanism for the recalcitrance of biochars: interactive effects of carbon and silicon components. *Environmental Science & Technology*, *48*(16), 9103–9112. https://doi.org/10.1021/es405647e

Hawley, E. I., Deeb, R. A., Kavanaugh, M. C., & Jacobs, J. (2004). *Treatment technologies for chromium (VI)*. *Chromium (VI) …*. https://doi.org/10.1002/chin.200614270

Hayes, R. B. (1997). The carcinogenicity of metals in humans, *8*, 371–385.

Hsu, N. H., Wang, S. L., Lin, Y. C., Sheng, G. D., & Lee, J. F. (2009). Reduction of Cr(VI) by crop-residue-derived black carbon. *Environmental Science and Technology*, *43*(23), 8801–8806. https://doi.org/10.1021/es901872x

Hsu, N., Wang, S., Liao, Y., Huang, S., Tzou, Y., & Huang, Y. (2009). Removal of hexavalent chromium from acidic aqueous solutions using rice straw-derived carbon, *171*, 1066–1070. https://doi.org/10.1016/j.jhazmat.2009.06.112

Inyang, M., Gao, B., Yao, Y., Xue, Y., Zimmerman, A. R., Pullammanappallil, P., & Cao, X. (2012). Removal of heavy metals from aqueous solution by biochars derived from anaerobically digested biomass. *Bioresource Technology*, *110*, 50–56. https://doi.org/10.1016/j.biortech.2012.01.072

Inyang, M. I., Gao, B., Yao, Y., Xue, Y., Zimmerman, A., Mosa, A., … Zimmerman, A. (2016). Technology A review of biochar as a low-cost adsorbent for aqueous heavy metal removal. *Critical Reviews in Environmental Science and Technology*, *46*(4), 406–433. https://doi.org/10.1080/10643389.2015.1096880

Johansson, C. L., Paul, N. A., Nys, R. De, & Roberts, D. A. (2016). Simultaneous biosorption of selenium , arsenic and molybdenum with modi fi ed algal-based biochars. *Journal of*

*Environmental Management*, *165*, 117–123. https://doi.org/10.1016/j.jenvman.2015.09.021

Jones, S., Bardos, R. P., Kidd, P. S., Mench, M., Leij, F. De, Hutchings, T., … Menger, P. (2016). Biochar and compost amendments enhance copper immobilisation and support plant growth in contaminated soils. *Journal of Environmental Management*, *171*, 101–112. https://doi.org/10.1016/j.jenvman.2016.01.024

Keiluweit, M., Nico, P. S., Johnson, M. G., & Kleber, M. (2010). Dynamic molecular structure of plant biomass-derived black carbon (Biochar). *Environmental Science and Technology*, *44*(4), 1247–1253.

Kelly, S., Hesterberg, D., & Ravel, B. (2008). Analysis of soils and minerals using X-ray absorption spectroscopy. *Methods of Soil Analysis. Part 5: Mineralogical Methods*, (5), 387–464. https://doi.org/10.2136/sssabookser5.5.c14

Keown, D. M., Li, X., Hayashi, J. ichiro, & Li, C. Z. (2008). Evolution of biomass char structure during oxidation in O2 as revealed with FT-Raman spectroscopy. *Fuel Processing Technology*, *89*(12), 1429–1435. https://doi.org/10.1016/j.fuproc.2008.07.002

Khare, P., Dilshad, U., Rout, P. K., Yadav, V., & Jain, S. (2013). Plant refuses driven biochar: Application as metal adsorbent from acidic solutions. *Arabian Journal of Chemistry*. https://doi.org/10.1016/j.arabjc.2013.11.047

Kim, P., Johnson, A., Edmunds, C. W., Radosevich, M., Vogt, F., Rials, T. G., & Labbé, N. (2011). Surface functionality and carbon structures in lignocellulosic-derived biochars produced by fast pyrolysis. *Energy and Fuels*, *25*(10), 4693–4703. https://doi.org/10.1021/ef200915s

Kimbrough et al. (1999). A Critical Assessment of Chromium in the Environment. *Critical Reviews in Environmental Science and Technology*, *29*(1), 1–46.

https://doi.org/10.1080/10643389991259164

Kloss, S., Zehetner, F., Dellantonio, A., Hamid, R., Ottner, F., Liedtke, V., … Soja, G. (2012). Characterization of Slow Pyrolysis Biochars: Eff ects of Feedstocks and Pyrolysis Temperature on Biochar Properties. https://doi.org/10.2134/jeq2011.0070

Kotasâ, J., & Stasicka, Z. (2000). Chromium occurrence in the environment and methods of its speciation, *107*.

Lehmann, J. (2007). A handful of carbon. *Nature*, *447*(7141), 143–144. https://doi.org/10.1038/447143a

Lehmann, J., & Rondon, M. (2006). Bio-Char Soil Management on Highly, (March). https://doi.org/10.1201/9781420017113.ch36

Lehmann, J., & Steiner, C. (2003). Nutrient availability and leaching in an archaeological Anthrosol and a Ferralsol of the Central Amazon basin ..., (January). https://doi.org/10.1023/A

Li, X., Shen, Q., Zhang, D., Mei, X., Ran, W., Xu, Y., & Yu, G. (2013). Functional Groups Determine Biochar Properties (pH and EC) as Studied by Two-Dimensional 13C NMR Correlation Spectroscopy. *PLoS ONE*, *8*(6). https://doi.org/10.1371/journal.pone.0065949

Lindqvist-Reis, P., Munoz-Paez, A., Diaz-Moreno, S., Pattanaik, S., Persson, I., & Sandström, M. (1998). The Structure of the Hydrated Gallium(III), Indium(III), and Chromium(III) Ions in Aqueous Solution. A Large Angle X-ray Scattering and EXAFS Study. *Inorg Chem*, *37*(26), 6675–6683. Retrieved from http://www.ncbi.nlm.nih.gov/pubmed/11670798

Liu, N., Huo, K., McDowell, M. T., Zhao, J., & Cui, Y. (2013). Rice husks as a sustainable source of nanostructured silicon for high performance Li-ion battery anodes. *Scientific Reports*, *3*, 1–7. https://doi.org/10.1038/srep01919

May, T., W, & Wiedmeyer. (1998). *tomic pectroscopy In This Issue :* (Vol. 19).

Melo, L. C. a, Coscione, A. R., Abreu, C. a., Puga, A. P., & Camargo, O. a. (2013). Influence of pyrolysis temperature on cadmium and zinc sorption capacity of sugar cane straw-derived biochar. *BioResources*, *8*(4), 4992–5004.

Mohan, D., Rajput, S., Singh, V. K., Steele, P. H., & Pittman, C. U. (2011). Modeling and evaluation of chromium remediation from water using low cost bio-char, a green adsorbent. *Journal of Hazardous Materials*, *188*(1–3), 319–333. https://doi.org/10.1016/j.jhazmat.2011.01.127

Mohan, D., Sarswat, A., Ok, Y. S., & Pittman, C. U. (2014). Organic and inorganic contaminants removal from water with biochar, a renewable, low cost and sustainable adsorbent - A critical review. *Bioresource Technology*, *160*, 191–202. https://doi.org/10.1016/j.biortech.2014.01.120

Mohanty, P., Nanda, S., Pant, K. K., Naik, S., Kozinski, J. A., & Dalai, A. K. (2013). Evaluation of the physiochemical development of biochars obtained from pyrolysis of wheat straw , timothy grass and pinewood : Effects of heating rate. *Journal of Analytical and Applied Pyrolysis*, *104*, 485–493. https://doi.org/10.1016/j.jaap.2013.05.022

Mukherjee, A., Zimmerman, A. R., & Harris, W. (2011). Surface chemistry variations among a series of laboratory-produced biochars. *Geoderma*, *163*(3–4), 247–255. https://doi.org/10.1016/j.geoderma.2011.04.021

Mulligan, C. N., Yong, R. N., & Gibbs, B. F. (2001). Remediation technologies for metal-contaminated soils and groundwater: An evaluation. *Engineering Geology*, *60*(1–4), 193–207. https://doi.org/10.1016/S0013-7952(00)00101-0

Murphy, V., Hughes, H., & McLoughlin, P. (2008). Comparative study of chromium biosorption

by red, green and brown seaweed biomass. *Chemosphere*, *70*(6), 1128–1134. https://doi.org/10.1016/j.chemosphere.2007.08.015

Murphy, V., Tofail, S. A. M., Hughes, H., & McLoughlin, P. (2009). A novel study of hexavalent chromium detoxification by selected seaweed species using SEM-EDX and XPS analysis. *Chemical Engineering Journal*, *148*(2–3), 425–433. https://doi.org/10.1016/j.cej.2008.09.029

Nagamori, M., Malinsky, I., & Claveau, A. (1986). Thermodynamics of the Si-C-O system for the production of silicon carbide and metallic silicon. *Metallurgical Transactions B*, *17*(3), 503–514. https://doi.org/10.1007/BF02670216

Naik, S., Goud, V. V., Rout, P. K., Jacobson, K., & Dalai, A. K. (2010). Characterization of Canadian biomass for alternative renewable biofuel. *Renewable Energy*, *35*(8), 1624–1631. https://doi.org/10.1016/j.renene.2009.08.033

Nanda, S., Mohanty, P., Pant, K. K., Naik, S., Kozinski, J. A., & Dalai, A. K. (2013). Characterization of North American Lignocellulosic Biomass and Biochars in Terms of their Candidacy for Alternate Renewable Fuels. *Bioenergy Research*, *6*(2), 663–677. https://doi.org/10.1007/s12155-012-9281-4

Nguyen, T. A. H., Ngo, H. H., Guo, W. S., Zhang, J., Liang, S., Yue, Q. Y., … Nguyen, T. V. (2013). Applicability of agricultural waste and by-products for adsorptive removal of heavy metals from wastewater, *148*, 574–585. https://doi.org/10.1016/j.biortech.2013.08.124

O'Toole, a, de Zarruk, K. K., Steffens, M., & Rasse, D. P. (2013). Characterization, Stability, and Plant Effects of Kiln-Produced Wheat Straw Biochar. *Journal of Environmental Quality*, *42*(2), 429–436. https://doi.org/Doi 10.2134/Jeq2012.0163

Ohta, A., Kagi, H., Tsuno, H., Nomura, M., & Okai, T. (2012). Speciation study of Cr(VI/III)

reacting with humic substances and determination of local structure of Cr binding humic substances using XAFS spectroscopy. *Geochemical Journal*, *46*(5), 409–420. https://doi.org/10.2343/geochemj.2.0222

Owlad, M., & Aroua, M. K. (2009). Removal of Hexavalent Chromium-Contaminated Water and Wastewater : A Review, 59–77. https://doi.org/10.1007/s11270-008-9893-7

Palmer, C. D., & Wittbrodt, P. R. (1991). Processes Affecting the Remediation of Chromium-Contaminated Sites. *Environmental Health Perspectives*, *92*(6), 25–40.

Park, D., Lim, S.-R., Yun, Y.-S., & Park, J. M. (2008). Development of a New Cr ( VI ) - biosorbent from Agricultural Biowaste, (January). https://doi.org/10.1016/j.biortech.2008.04.042

Park, D., Yun, Y. S., Ahn, C. K., & Park, J. M. (2007). Reduction of Hexavalent chromium with the brown seaweed Ecklonia biomass. *Environmental Science and Technology*, *38*(18), 4860–4864. https://doi.org/10.1021/es035329+

Park, D., Yun, Y. S., & Park, J. M. (2005). Use of dead fungal biomass for the detoxification of hexavalent chromium: Screening and kinetics. *Process Biochemistry*, *40*(7), 2559–2565. https://doi.org/10.1016/j.procbio.2004.12.002

Park, D., Yun, Y. S., & Park, J. M. (2006). Mechanisms of the removal of hexavalent chromium by biomaterials or biomaterial-based activated carbons. *Journal of Hazardous Materials*, *137*(2), 1254–1257. https://doi.org/10.1016/j.jhazmat.2006.04.007

Park, D., Yun, Y. S., & Park, J. M. (2008). XAS and XPS studies on chromium-binding groups of biomaterial during Cr(VI) biosorption. *Journal of Colloid and Interface Science*, *317*(1), 54–61. https://doi.org/10.1016/j.jcis.2007.09.049

Park, J. H., Choppala, G. K., Bolan, N. S., Chung, J. W., & Chuasavathi, T. (2011). Biochar

reduces the bioavailability and phytotoxicity of heavy metals. *Plant and Soil*, *348*(1–2), 439–451. https://doi.org/10.1007/s11104-011-0948-y

Parkhurst, B. D. L., & Appelo, C. a J. (1999). User's Guide To PHREEQC (version 2) — a Computer Program for Speciation, and Inverse Geochemical Calculations. *Exchange Organizational Behavior Teaching Journal*, *D*(Version 2), 326. https://doi.org/Rep. 99-4259

Parsons, J. G., Hejazi, M., Tiemann, K. J., Henning, J., & Gardea-Torresdey, J. L. (2002). An XAS study of the binding of copper(II), zinc(II), chromium(III) and chromium(VI) to hops biomass. *Microchemical Journal*, *71*(2–3), 211–219. https://doi.org/10.1016/S0026-265X(02)00013-9

Perova, T. S., Wasyluk, J., Kukushkin, S. A., Osipov, A. V., Feoktistov, N. A., & Grudinkin, S. A. (2010). Micro-raman mapping of 3C-SiC thin films grown by solid-gas phase epitaxy on Si (111). *Nanoscale Research Letters*, *5*(9), 1507–1511. https://doi.org/10.1007/s11671-010-9670-6

Pollard S., Fowler G., Sollars C., P. R. (1992). Low cost adsorbents for waste and wastewater treatment: a review. *Sci. Total Environ.*, *116*, 31–52.

Rai, D., Eary L.E., & Zachara, J. . (1989). E n v i r o n m e n t a l chemistry of chromium, *86*, 15–23.

Rao, L., Zhang, Z., Friese, J. I., Ritherdon, B., Clark, S. B., Hess, N. J., & Rai, D. (2002). Oligomerization of chromium(iii) and its impact on the oxidation of chromium(iii) by hydrogen peroxide in alkaline solutions. *Journal of the Chemical Society, Dalton Transactions*, (2), 267. https://doi.org/10.1039/b104154c

Raveendran, K., & Ganesh, A. (1998). Adsorption characteristics and pore-development of

biomass-pyrolysis char. *Fuel*, *77*(7), 769–781. https://doi.org/10.1016/S0016-2361(97)00246-9

Ravel, B., & Newville, M. (2005). ATHENA, ARTEMIS, HEPHAESTUS: Data analysis for X-ray absorption spectroscopy using IFEFFIT. *Journal of Synchrotron Radiation*, *12*(4), 537–541. https://doi.org/10.1107/S0909049505012719

Ressler, T. (1998). WinXAS: a Program for X-ray Absorption Spectroscopy Data Analysis under MS-Windows. *Journal of Synchrotron Radiation*, *5*(2), 118–122. https://doi.org/10.1107/S0909049597019298

Rihs, S., Gaillard, C., Reich, T., & Kohler, S. J. (2014). Uranyl sorption onto birnessite: A surface complexation modeling and EXAFS study. *Chemical Geology*, *373*, 59–70. https://doi.org/10.1016/j.chemgeo.2014.02.025

Rinklebe, J., Shaheen, S. M., & Frohne, T. (2016). Chemosphere Amendment of biochar reduces the release of toxic elements under dynamic redox conditions in a contaminated floodplain soil. *Chemosphere*, *142*, 41–47. https://doi.org/10.1016/j.chemosphere.2015.03.067

Roberts, K. G., Gloy, B. A., Joseph, S., Scott, N. R., & Lehmann, J. (2009). Life Cycle Assessment of Biochar Systems: Estimating the Energetic, Economic, and Climate Change Potential, 827–833. https://doi.org/10.1021/es902266r

Roussel, H., Briois, V., Elkaim, E., Roy, A. de, Besse, J.-P., & Jolivet, J.-P. (2001). Study of the formation pof the layered double hydroxide Hydroxide [Zn - Cr - Cl], *II*(12), 329–337.

Saha, B., & Orvig, C. (2010). Biosorbents for hexavalent chromium elimination from industrial and municipal effluents. *Coordination Chemistry Reviews*, *254*(23–24), 2959–2972. https://doi.org/10.1016/j.ccr.2010.06.005

Samrat Alam, M., Cossio, M., Robinson, L., Wang, X., Kenney, J. P. L., Konhauser, K. O., …

Alessi, D. S. (2016). Removal of organic acids from water using biochar and petroleum coke. *Environmental Technology & Innovation*, *6*(6), 141–151. https://doi.org/10.1016/j.eti.2016.08.005

Santos, A., Yustos, P., Quintanilla, A., Rodríguez, S., & García-Ochoa, F. (2002). Route of the catalytic oxidation of phenol in aqueous phase. *Applied Catalysis B: Environmental*, *39*(2), 97–113. https://doi.org/10.1016/S0926-3373(02)00087-5

Savitzky, A., & Golay, M. J. E. (1964). Smoothing and Differentiation of Data, *36*(8), 1627–1639.

Sharma, D. C., & Forster, C. E. (1994). A Preliminary Examination Into the Adsorption of Hexavalent Chromium using Low-Cost Adsorbents. *Bioresource Technology*, *47*, 257–264. https://doi.org/10.1016/0960-8524(94)90189-9

Shen, Y. S., Wang, S. L., Huang, S. T., Tzou, Y. M., & Huang, J. H. (2010). Biosorption of Cr(VI) by coconut coir: Spectroscopic investigation on the reaction mechanism of Cr(VI) with lignocellulosic material. *Journal of Hazardous Materials*, *179*(1–3), 160–165. https://doi.org/10.1016/j.jhazmat.2010.02.073

Shen, Y. S., Wang, S. L., Tzou, Y. M., Yan, Y. Y., & Kuan, W. H. (2012). Removal of hexavalent Cr by coconut coir and derived chars - The effect of surface functionality. *Bioresource Technology*, *104*, 165–172. https://doi.org/10.1016/j.biortech.2011.10.096

Singh, B., Singh, B. P., & Cowie, A. L. (2010). Characterisation and evaluation of biochars for their application as a soil amendment. *Australian Journal of Soil Research*, *48*(6–7), 516–525. https://doi.org/10.1071/SR10058

Song, Z., Wang, H., Strong, P. J., & Shan, S. (2014). Increase of available soil silicon by Si-rich manure for sustainable rice production. *Agronomy for Sustainable Development*, *34*(4),

813–819. https://doi.org/10.1007/s13593-013-0202-5

Spokas, K. a. (2010). Review of the stability of biochar in soils: predictability of O:C molar ratios. *Carbon Management*, *1*(2), 289–303. https://doi.org/10.4155/cmt.10.32

Tang, J., Zhu, W., Kookana, R., & Katayama, A. (2013). Characterization of biochar and its application in remediation of contaminated soil. *Journal of Bioscience and Bioengineering*, *116*(6), 653–659.

Titiladunayo, I. F., McDonald, A. G., & Fapetu, O. P. (2012). Effect of Temperature on Biochar Product Yield from Selected Lignocellulosic Biomass in a Pyrolysis Process, 311–318. https://doi.org/10.1007/s12649-012-9118-6

Tytłak, A., Oleszczuk, P., & Dobrowolski, R. (2015). Sorption and desorption of Cr(VI) ions from water by biochars in different environmental conditions. *Environmental Science and Pollution Research*, *22*(8), 5985–5994. https://doi.org/10.1007/s11356-014-3752-4

Uchimiya, M., Chang, S., & Klasson, K. T. (2011). Screening biochars for heavy metal retention in soil: Role of oxygen functional groups. *Journal of Hazardous Materials*, *190*(1–3), 432–441. https://doi.org/10.1016/j.jhazmat.2011.03.063

Uchimiya, M., Wartelle, L. H., Klasson, K. T., Fortier, C. A., & Lima, I. M. (2011). Influence of Pyrolysis Temperature on Biochar Property and Function as a Heavy Metal Sorbent in Soil, 2501–2510.

Verheijen, F., Jeffery, S., Bastos, a C., Van Der Velde, M., & Diafas, I. (2010). *Biochar Application to Soils*. *Environment* (Vol. 8). https://doi.org/10.2788/472

von Gunten, K., Alam, M. S., Hubmann, M., Ok, Y. S., Konhauser, K. O., & Alessi, D. S. (2017). Modified sequential extraction for biochar and petroleum coke: Metal release potential and its environmental implications. *Bioresource Technology*, *236*, 106–110.

https://doi.org/10.1016/j.biortech.2017.03.162

Wang, S. L., & Lee, J. F. (2011). Reaction mechanism of hexavalent chromium with cellulose. *Chemical Engineering Journal*, *174*(1), 289–295. https://doi.org/10.1016/j.cej.2011.09.031

Wang, T., Camps-Arbestain, M., & Hedley, M. (2013). Predicting C aromaticity of biochars based on their elemental composition. *Organic Geochemistry*, *62*, 1–6. https://doi.org/10.1016/j.orggeochem.2013.06.012

Wang, X. S., Chen, L. F., Li, F. Y., Chen, K. L., Wan, W. Y., & Tang, Y. J. (2010). Removal of Cr (VI) with wheat-residue derived black carbon: Reaction mechanism and adsorption performance. *Journal of Hazardous Materials*, *175*(1–3), 816–822. https://doi.org/10.1016/j.jhazmat.2009.10.082

Wu, Y., Zhang, S., Guo, X., & Huang, H. (2008). Adsorption of chromium(III) on lignin. *Bioresource Technology*, *99*(16), 7709–7715. https://doi.org/10.1016/j.biortech.2008.01.069

Xiao, X., & Chen, B. (2017). A Direct Observation of the Fine Aromatic Clusters and Molecular Structures of Biochars. *Environmental Science and Technology*, *51*(10), 5473–5482. https://doi.org/10.1021/acs.est.6b06300

Xiao, X., Chen, B., & Zhu, L. (2014). Transformation, morphology, and dissolution of silicon and carbon in rice straw-derived biochars under different pyrolytic temperatures. *Environmental Science and Technology*, *48*(6), 3411–3419. https://doi.org/10.1021/es405676h

Xiao, X., Chen, Z., & Chen, B. (2016). H/C atomic ratio as a smart linkage between pyrolytic temperatures, aromatic clusters and sorption properties of biochars derived from diverse precursory materials. *Scientific Reports*, *6*(October 2015), 22644. https://doi.org/10.1038/srep22644

Yang, H. (2007). Characteristics of hemicellulose , cellulose and lignin pyrolysis, *86*, 1781–1788. https://doi.org/10.1016/j.fuel.2006.12.013

Yuan, X., Huang, H., Zeng, G., Li, H., Wang, J., & Zhou, C. (2011). Bioresource Technology Total concentrations and chemical speciation of heavy metals in liquefaction residues of sewage sludge. *Bioresource Technology*, *102*(5), 4104–4110. https://doi.org/10.1016/j.biortech.2010.12.055

Zhang, H., Tang, Y., Cai, D., Liu, X., Wang, X., Huang, Q., & Yu, Z. (2010). Hexavalent chromium removal from aqueous solution by algal bloom residue derived activated carbon: Equilibrium and kinetic studies. *Journal of Hazardous Materials*, *181*(1–3), 801–808. https://doi.org/10.1016/j.jhazmat.2010.05.084

Zhang, M., & Ok, Y. S. (2014). Biochar soil amendment for sustainable agriculture with carbon and contaminant sequestration. *Carbon Management*, *5*(3), 255–257. https://doi.org/10.1080/17583004.2014.973684

Zhao, L., Cao, X., Mašek, O., & Zimmerman, A. (2013). Heterogeneity of biochar properties as a function of feedstock sources and production temperatures. *Journal of Hazardous Materials*, *256–257*, 1–9. https://doi.org/10.1016/j.jhazmat.2013.04.015

Zhuang, L. W., Zhang, W. H., Lu, H. L., Yang, Y. X., & Qiu, R. L. (2011). Removal of heavy metal ions from aqueous solution by sludge derived- biochar pyrolyzed under different heating conditions, 857–864.